

**DIRECT NUMERICAL SIMULATION OF PARTICLE-LADEN  
TURBULENCE IN A STRAIGHT SQUARE DUCT**

A Thesis

by

GAURAV SHARMA

Submitted to the Office of Graduate Studies of  
Texas A&M University  
in partial fulfillment of the requirements for the degree of  
MASTER OF SCIENCE

May 2004

Major Subject: Mechanical Engineering

**DIRECT NUMERICAL SIMULATION OF PARTICLE-LADEN  
TURBULENCE IN A STRAIGHT SQUARE DUCT**

A Thesis

by

GAURAV SHARMA

Submitted to Texas A&M University  
in partial fulfillment of the requirements  
for the degree of

MASTER OF SCIENCE

Approved as to style and content by:

---

Denis J. Phares  
(Chair of Committee)

---

Ali Beskok  
(Member)

---

Othon K. Rediniotis  
(Member)

---

Dennis O'Neal  
(Head of Department)

May 2004

Major Subject: Mechanical Engineering

## ABSTRACT

Direct Numerical Simulation of Particle-Laden Turbulence  
in a Straight Square Duct. (May 2004)

Gaurav Sharma, B. Tech., Regional Engineering College Hamirpur, India

Chair of Advisory Committee: Dr. Denis J. Phares

Particle-laden turbulent flow through a straight square duct at  $Re_\tau = 300$  is studied using direct numerical simulation (DNS) and Lagrangian particle tracking. A parallelized 3-D particle tracking direct numerical simulation code has been developed to perform the large-scale turbulent particle transport computations reported in this thesis. The DNS code is validated after demonstrating good agreement with the published DNS results for the same flow and Reynolds number. Lagrangian particle transport computations are carried out using a large ensemble of passive tracers and finite-inertia particles and the assumption of one-way fluid-particle coupling. Using four different types of initial particle distributions, Lagrangian particle dispersion, concentration and deposition are studied in the turbulent straight square duct. Particles are released in a uniform distribution on a cross-sectional plane at the duct inlet, released as particle pairs in the core region of the duct, distributed randomly in the domain or distributed uniformly in planes at certain heights above the walls. One- and two-particle dispersion statistics are computed and discussed for the low Reynolds number inhomogeneous turbulence present in a straight square duct. New detailed statistics on particle number concentration and deposition are also obtained and discussed.

## **DEDICATION**

I dedicate this thesis to the loving memory of my late grandmother, Smt. Nandi Devi.

I also dedicate this thesis to my mother, Bimla Sharma.

## ACKNOWLEDGEMENTS

I am grateful to my advisor, Dr. Denis Phares, for his encouragement and support for this research. I thank Dr. Phares for his supervision of my research and for his valuable comments. I also thank him for his efforts in financially supporting me for a part of my study at Texas A&M. Dr. Phares has been understanding and has beared with me in my pursuit of obtaining these computationally expensive results. Dr. Phares gave me the freedom to work on a research topic that was of most interest to me. I am grateful to him for trusting in my capabilities for this research endeavor. I feel fortunate that I choose him as my academic advisor at Texas A&M and I have greatly enjoyed working with him.

I gratefully acknowledge the generous use of computational resources at the Texas A&M Supercomputing Facility. I also acknowledge technical support related help from Spiros Vellas and other members of staff at the Texas A&M Supercomputing Facility. I am grateful to NAG Inc. for allowing me to modify and parallelize a function in the source code of the NAG Fortran numerical library. Most of the computations reported in this thesis were performed on K2 (SGI Origin 3800) and Agave (IBM p690) parallel supercomputers at the Texas A&M Supercomputing Facility. A small part of the computations reported in this thesis was performed on the National Science Foundation Terascale Computing System (HP-Compaq Alphaserver) at the Pittsburgh Supercomputing Center using NSF-NPACI grant no. CTS030005P. Partial financial support from the Comprehensive Test Ban Treaty Organization (CTBTO), through the Lovelace Respiratory Research Institute, under contract no. JK020160 is gratefully acknowledged.

I am grateful to Dr. M. D. Deshpande for providing me the 3-D cavity flow code. Some sections of that code were rewritten, modified or used directly while developing a new larger code for the present study. For a one-year period following my undergraduate studies, I had greatly enjoyed working as a graduate trainee under the supervision of Dr. Deshpande at the Computational and Theoretical Fluid Dynamics (CTFD) Division of

National Aerospace Laboratories (N.A.L.), Bangalore. I am grateful to Dr. Deshpande and to Dr. P. N. Shankar for that opportunity. I especially thank Dr. Deshpande for stimulating my interest in direct numerical simulations.

I thank Dr. Ali Beskok and Dr. Othon Rediniotis for serving on my committee. I also thank them for their comments.

I would like to take this opportunity to thank my parents for their love and understanding. I also thank them for their effort in financially supporting me partially for a semester after I transferred from the University of Houston to Texas A&M in fall'01. I wholeheartedly thank my mother, Bimla Sharma, for her love and sacrifices.

I had a memorable time with my friends in the department and our lab: Praveen Ramaprabhu, Satyanarayan Seshadri, Vasanth Muralidharan and Stan Glagolenko.

## TABLE OF CONTENTS

	Page
ABSTRACT .....	iii
DEDICATION .....	iv
ACKNOWLEDGEMENTS .....	v
TABLE OF CONTENTS .....	vii
LIST OF FIGURES .....	viii
LIST OF TABLES .....	xii
1. INTRODUCTION .....	1
2. NUMERICAL PROCEDURE .....	5
2.1 Eulerian equations of motion .....	5
2.2 Spatial and temporal discretization .....	7
2.3 Lagrangian equations of motion .....	12
2.4 Tricubic interpolation on 3-D staggered grid .....	15
2.5 Particle tracking code parallelization .....	20
3. TURBULENT FLOW SIMULATION .....	25
3.1 Flow parameters and turbulence simulation .....	25
3.2 Flow verification .....	31
4. LAGRANGIAN PARTICLE TRANSPORT .....	37
4.1 Dispersed particles visualization .....	37
4.2 One- and two-particle Lagrangian dispersion .....	44
4.2.1 Case I simulations .....	45
4.2.2 Case II simulations .....	49
4.3 Particle concentration and deposition statistics .....	58
4.3.1 Case III simulations .....	58
4.3.2 Case IV simulations .....	62
4.3.3 Deposition rate .....	70
5. CONCLUSIONS .....	76
REFERENCES .....	78
VITA .....	83

## LIST OF FIGURES

FIGURE	Page
2.1 Flow geometry and coordinate system for a straight square duct.....	5
2.2 Schematic of a particle moving through the 3-D staggered grid. Shown also are the eight neighboring grid points (at cell faces) used for interpolating fluid velocity at its location.....	16
2.3 The values assumed by three linear parameters at the eight grid points in tricubic interpolation.....	17
2.4 Sparse structure of the constant coefficient matrix, WT3D.....	18
2.5 Parallel performance of the particle tracking code on SGI Origin 3800 and IBM p690 parallel supercomputers.....	23
3.1 Contours of streamwise velocity in the initial (unidirectional) laminar flow.....	26
3.2 Contours of instantaneous turbulent (a) streamwise velocity and (b) secondary flow in a cross-sectional plane at $x/h = 2\pi$ .....	26
3.3 Contours of streamwise velocity at (a) $y/h = 0.5$ in the laminar flow initial condition. Contours of instantaneous turbulent streamwise velocity at (b) $y^+ = 4$ (c) $y^+ = 15$ (d) $y^+ = 150$ , and secondary flow at (e) $y^+ = 4$ (f) $y^+ = 15$ (g) $y^+ = 150$ .....	27
3.4 Instantaneous turbulent velocity time trace at three cross-stream locations.....	29
3.5 Coefficients of one-point velocity correlation at three cross-stream locations.....	30
3.6 Coefficients of two-point velocity correlation at four cross-stream locations.....	31
3.7 Quadrant-averaged profiles of the mean streamwise velocity at five spanwise locations. ( ___ ) Present DNS, ( ○ ) Gavrilakis (1992).....	32
3.8 Quadrant-averaged profiles of the rms fluctuations in streamwise velocity at five spanwise locations. ( ___ ) Present DNS, ( ○ ) Gavrilakis (1992).....	32
3.9 Quadrant-averaged profiles of the mean spanwise velocity at five spanwise locations. ( ___ ) Present DNS, ( ○ ) Gavrilakis (1992).....	33
3.10 Quadrant-averaged profiles of the rms fluctuations in spanwise velocity at five spanwise locations. ( ___ ) Present DNS, ( ○ ) Gavrilakis (1992).....	33



FIGURE	Page
3.11 (a) Quadrant-averaged profile of the primary Reynolds stress component, $\langle -u'v' \rangle$ , normalized by the local wall-friction velocity at mid-wall location. (b) Profile of wall shear stress as a function of distance along the wall and normalized by the average shear stress over the wetted area of duct. (c) Profile of mean streamwise velocity component at duct centerline on a log-linear scale and normalized by the mean friction velocity. Shown also is the corresponding profile from Gavrilakis (1992) DNS and profiles of the law of the wall and the log-law. In figures (a-c) above: ( — ) Present DNS, ( ○ ) Gavrilakis (1992).....	34
4.1 Effect of inertia on Lagrangian dispersion of particles released from the same point.....	37
4.2 Particle velocity time trace for particles released from the same point at duct centerline.....	39
4.3 Coefficients of Lagrangian velocity auto-correlation from a typical trajectory.....	40
4.4 Initial distribution of particles in the domain for (a) Case I, (b) Case II ( $r_0^+ = 24.0$ shown), (c) Case III and (d) Case IV ( $y_0^+ = 30$ shown).....	41
4.5 Instantaneous particle positions for $\tau_p^+ = 15$ particles at $t^+ =$ (a) 0, (b) 135, (c) 265 and (d) 675 for an initial release height of $y_0^+ = 3$ (Case IV simulation). Particles are visualized in the $x$ - $z$ plane and a $y$ bin of width 30 wall units from the bottom wall.....	42
4.6 Instantaneous particle positions for passive tracer particles at $t^+ =$ (a) 0, (b) 135, (c) 265 and (d) 675 for an initial release height of $y_0^+ = 3$ (Case IV simulation). Particles are visualized in the $y$ - $z$ plane and a $x$ bin that is 150 wall units wide ( $h/4$ wide on either side of $x = L_x/2$ ).....	43
4.7 Particle penetration measured in streamwise bins of length $h$ through the square duct.....	47
4.8 Growth of (a) RMS displacement and (b) mean square displacement (MSD). Particle response times are $\tau_p^+ = (0, 3, 5, 10, 15, 20, 30$ and $50)$ for curves (a – h).....	47
4.9 Time variation of the turbulent particle diffusivity. Particle response times are $\tau_p^+ = (0, 3, 5, 10, 15, 20, 30$ and $50)$ for curves (a – h).....	49
4.10 Time variation of the square of inter-particle separation for $r_0^+ = 0.5$ .....	52
4.11 Time variation of the square of inter-particle separation for $r_0^+ = 24.0$ .....	52

FIGURE	Page
4.12 Time variation of the square of inter-particle separation for (a) $r_0^+ = 2.0$ , (b) $r_0^+ = 8.0$ , (c) $r_0^+ = 12.0$ and (d) $r_0^+ = 16.0$ .....	53
4.13 Time variation of the RMS inter-particle velocity difference for (a) $r_0^+ = 2.0$ and (b) $r_0^+ = 24.0$ .....	53
4.14 pdfs of the $x$ -direction standardized inter-particle separations at a late time of the simulation ( $t^+ = 1800$ ) for $\tau_p^+ = 15$ and (a) $r_0^+ = 2.0$ and (b) $r_0^+ = 24.0$ . The dotted line represents the standard Gaussian.....	54
4.15 pdfs of the $x$ -direction standardized inter-particle separations at five different times of the simulation for passive tracer particles and four different initial inter-particle separations. The dotted line represents the standard Gaussian.....	54
4.16 pdfs of the $x$ -direction standardized inter-particle separations at five different times of the simulation for $\tau_p^+ = 30$ particles and four different initial inter-particle separations. The dotted line represents the standard Gaussian.....	55
4.17 pdfs of the $x$ -direction standardized inter-particle separations at the end of Case II simulation ( $t^+ = 1800$ ) for four different particle response times and for (a) $r_0^+ = 0.5$ and (b) $r_0^+ = 24.0$ . The dotted line represents the standard Gaussian.....	55
4.18 Skewness and flatness factors in the $x$ -direction inter-particle separations at two different times of the simulation. The dashed line represents a Gaussian distribution .....	57
4.19 Normalized instantaneous particle number concentration near the wall for initially random distribution of particles (Case III simulation).....	59
4.20 Normalized time-averaged particle number concentration near the wall for different inertia values in Case III simulation.....	60
4.21 Particle deposition rate normalized by the number of particles at time $t^+ = 0$ .....	60
4.22 Particle deposition rate normalized by time-local number of particles in time bins.....	61
4.23 For particles released at different heights above the wall, time variation of (a) mean distance from the wall, (b) variance in the distribution, (c) maximum distance, and (d) minimum distance from the wall.....	63

FIGURE	Page
4.24 Normalized instantaneous particle number concentration for $\tau_p^+ = 0$ (figures on the left) and $\tau_p^+ = 15$ (figures on the right), for three different initial release heights.....	65
4.25 Normalized instantaneous particle number concentration for the passive tracer particles at an early time after their release from eleven different initial release heights above the duct walls.....	66
4.26 Normalized instantaneous particle number concentration for four different particle response times and one initial release height.....	66
4.27 Normalized time-averaged particle number concentration near the wall in Case IV simulation.....	67
4.28 Normalized time-averaged particle number concentration along the streamwise direction for different inertia values in (a) Case III and (b) Case IV.....	67
4.29 Deposition rate from four different initial release heights in Case IV. Deposition rate is normalized by the number of particles in the domain at $t^+ = 0$ .....	68
4.30 (a) Fraction of particles deposited in Case III and Case IV as a function of particle response time. (b) Wall-impact velocities from Case III and Case IV simulations as a function of particle response time.....	68
4.31 Number of particles deposited between the total time of simulation, $0 \leq t_t^+ \leq 675$ and time of statistics, $75 < t_s^+ \leq 675$ , as a function of the initial release height.....	69
4.32 Averaged deposition rate from eleven different initial release heights, when normalized by the number of particles at $t^+ = 0$ .....	69
4.33 Averaged deposition rate from eleven different initial release heights, when normalized by the time varying number of particles in individual time bins.....	70
4.34 Time variation of the deposition constants computed in time bins in Case III.....	73
4.35 Time variation of the deposition constants computed in time bins in Case IV.....	73
4.36 Ensemble-averaged deposition constants from Case III and Case IV, as a function of particle response time.....	74

## LIST OF TABLES

TABLE	Page
3.1 Flow simulation parameters in the present DNS.....	25
3.2 Comparison of flow quantities computed in present DNS and their corresponding values computed by Gavrilakis (1992) and Vazquez & Metais (2002).....	34
4.1 Particle transport simulation parameters for Case I. $a_p^+$ refers to the dimensionless particle radius.....	46
4.2 Particle transport simulation parameters for Case II.....	50
4.3 Particle transport simulation parameters for Case III.....	59
4.4 Particle transport simulation parameters for Case IV.....	62
4.5 Computed deposition constants from present DNS Case III and Case IV.....	72

## 1. INTRODUCTION

Particle-laden turbulent flows are ubiquitous in nature and technology, but remain poorly understood. With a limited number of exceptions, most of the flows occurring in the natural world around us are turbulent. Most of the environmental and geophysical flows are also particle-laden, multiphase or granular. Examples include air pollution, cloud formation, snowfall, sediment transport in rivers, and phytoplankton rich oceans. Particle-laden flows also occur in wide ranging industrial applications. Examples include solid propellant combustion, fluidized bed combustion, drug delivery, powder manufacturing, transport of multiphase fluids through pipes and ducts, and wind tunnels. Due to renewed threats from bio-terrorism, there is an even greater need to enhance our current level of understanding of complex processes of particle mixing, dispersion, concentration and deposition. A better understanding of these fundamental processes can lead to new technologies and devices to counter more effectively the threats from bio-terrorism. Particle-laden turbulent flow through ducts of square or rectangular cross-section occurs in wide ranging industrial applications. It represents a particularly interesting case of turbulent particle transport due to the inhomogeneous near-wall turbulence and its effect on transport of the dispersed phase. Such flows are found in building ductwork, playing a central role in the transport of harmful air pollutants, dust, and biological aerosols from outdoor air to the indoor environment. In addition to the useful practical applications, turbulent flow through a duct of square or rectangular cross-section is a good choice for studying basic processes of particle mixing, accumulation and deposition in the presence of inhomogeneous wall-bounded turbulence.

The dynamics of a particle suspended in a turbulent flow is best studied in the Lagrangian frame of reference. Due to the practical difficulties in tracking a large number of particle trajectories over a sufficient period of time, only a few detailed experimental measurements have been performed (e.g. Virant & Dracos 1997; Jullien, Paret &

---

This thesis follows the style and format of *Journal of Fluid Mechanics*.

Tabeling 1999; Ott & Mann 2000; La Porta *et al.* 2001). By contrast, time-resolved numerical simulations of Lagrangian particle motion offer fewer practical difficulties, while providing significantly larger data sets. Accurate description of the Lagrangian particle motion requires accurate and detailed information about the instantaneous flow structure, which can only be obtained numerically when the exact Navier-Stokes equations are solved without any turbulence model.

Direct numerical simulation (DNS) is a time-accurate numerical simulation of the Navier-Stokes equations (unlike numerical solution of the time-averaged RANS equations), subject to prescribed initial and boundary conditions. Its strength lies in the fact that it attempts to resolve all the dynamically significant scales of fluid motion without any turbulence modeling. DNS, coupled with Lagrangian particle tracking, is a time-accurate simulation technique where trajectories of suspended particles can be integrated over prolonged periods of time. However, DNS is also a computationally very expensive approach due to the very fine spatial and temporal grid resolution requirements. The range of length and time scales present in a turbulent flow increases rapidly with Reynolds number. A fine grid capable of resolving the smallest dynamically significant length and time scales of fluid motion is required in DNS, which makes it impractical at present to simulate high Reynolds number flows. As a consequence, DNS was restricted to low Reynolds numbers only for quite some time. With the improvement in supercomputing hardware and efficient (parallel) numerical algorithms, it is now possible to perform DNS for some flows even at moderately high Reynolds numbers. The very high Reynolds number flows appear beyond the reach of DNS even in the foreseeable future. Nevertheless, the detailed information about the instantaneous turbulence structure provided by DNS is immensely helpful to researchers even at low and moderate Reynolds numbers. This valuable information is needed to understand the dynamics of turbulence for developing better models to predict it and for devising efficient strategies to control or manipulate it.

The computationally expensive nature of DNS methodology has given way to a flow simulation technique, where a significant reduction in computational time is achieved at

the cost of simulation accuracy. Large eddy simulation (LES) is a numerical technique where the larger, most energetic turbulent motions are solved directly like in a DNS, but the smaller sub-grid scale motions are modeled. A loss of accuracy occurs in this approach due to the modeling of sub-grid scale motions, which are generally assumed to be isotropic. However, not requiring resolution of the smallest scales makes it possible for LES to simulate higher Reynolds numbers than those currently possible in DNS. Most importantly, LES holds immense promise for the reasonably accurate estimation of high Reynolds number flows important to industry. However, the use of sub-grid scale models based on the incorrect assumption of isotropy of sub-grid scales raises many questions about use of LES as a research tool. Despite its high computational cost, no other numerical approach can match DNS in accurately simulating turbulent flows. Quoting Moin & Mahesh (1998): “...DNS is a research tool, and not a brute-force solution to the Navier-Stokes equations for engineering problems.” Efficient numerical algorithms, massively parallel computing and innovative new hardware shall bring moderately high Reynolds number DNS within the reach of more and more researchers in the future.

Within the last two decades, numerous DNS studies have appeared in the literature that have enhanced our understanding of complex processes like particle mixing, dispersion and deposition. Most of these computational studies focus on homogeneous and isotropic turbulent flows in periodic domains (e.g. Yeung & Pope 1989; Squires & Eaton 1991; Elghobashi & Truesdell 1992; Yeung 1994; Bagchi & Balachandar 2003). Among those that focus on inhomogeneous turbulent flows, the plane channel is the most studied wall-bounded flow geometry (McLaughlin 1989; Brooke, Hanratty & McLaughlin 1994). Particle-laden turbulent flow through a straight circular pipe has also drawn some attention (Uijtewaal & Oliemans 1996). Despite the currently available DNS databases, the field is still young and more simulations are needed to conclusively elucidate all the possible mechanisms by which particles disperse and deposit in inhomogeneous turbulent flows. This dictates the need for new and more detailed Lagrangian particle transport data spanning much wider ranges of flow Reynolds numbers and particle Stokes numbers. These data would also be valuable to researchers

developing improved models of turbulent mixing and dispersion, which are of great practical importance, especially in industrial flow applications where DNS is rarely feasible. Currently available stochastic turbulent dispersion models (see discussions in MacInnes & Bracco 1992; Sawford 2001; Yeung 2002) intended for use with mean flow simulations yield quite inaccurate predictions in most inhomogeneous flows. More accurate data, such as from time-accurate simulations like DNS coupled with Lagrangian particle tracking of large ensembles of particles, are required for improved models of turbulent dispersion.

In the present square duct flow, the spanwise direction is inhomogeneous and wall-bounded, unlike the widely studied plane channel flow. The two wall-bounded directions in a square duct give rise to a net secondary flow of Prandtl's second kind, which has the potential to significantly alter the turbulent particle transport compared to a plane channel. This thesis reports new results on particle dispersion, concentration and deposition in a duct of square cross-section using DNS coupled with Lagrangian particle tracking. The thesis is organized as follows. Section 2 describes the numerical procedure for DNS and Lagrangian particle tracking. Section 3 discusses the turbulent flow simulation and presents results demonstrating agreement in computed flow statistics between the present DNS and the DNS reported by Gavrilakis (1992). Section 4 presents the discussion on the computed statistics of one- and two-particle dispersion, particle concentration, and deposition of finite-inertia particles. Finally, Section 5 presents conclusions from the present simulations.



## 2. NUMERICAL PROCEDURE

In this section, the governing equations for fluid and particle phase are described along with their spatial and temporal discretization.

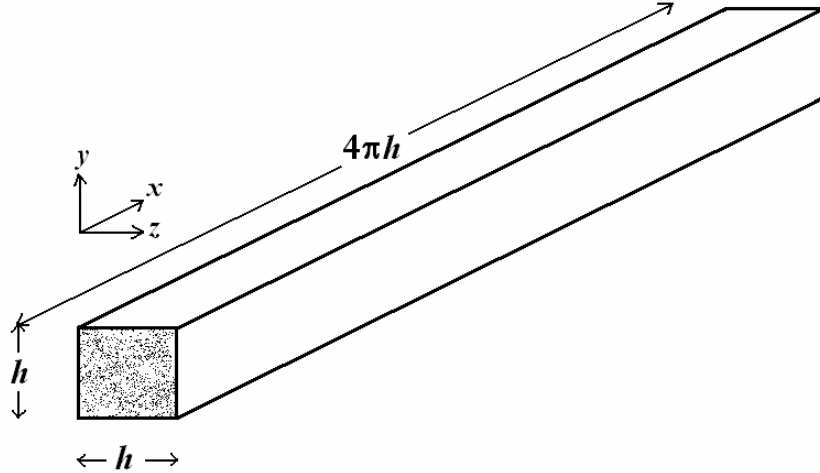


Figure 2.1. Flow geometry and coordinate system for a straight square duct.

### 2.1. Eulerian equations of motion

The flow domain of interest is a straight square duct (figure 2.1) which is bounded by no-slip walls in the cross-stream ( $y$  and  $z$ ) directions and the flow field is assumed to be instantaneously periodic in the statistically homogeneous streamwise ( $x$ ) direction. The governing equations of fluid phase are the familiar Navier-Stokes equations written in their non-dimensional form as

$$D \equiv \nabla \cdot \mathbf{U} = 0 \quad (2.1)$$

$$\frac{\partial \mathbf{U}}{\partial t} + (\mathbf{U} \cdot \nabla) \mathbf{U} = -\nabla P + \Pi \delta_{ij} + \frac{1}{Re_\tau} \nabla^2 \mathbf{U}. \quad (2.2)$$

Taking the divergence of (2.2) and using (2.1) gives the Poisson equation for pressure:

$$\nabla^2 P = -\nabla \cdot (\mathbf{U} \cdot \nabla) \mathbf{U} - \frac{\partial D}{\partial t} + \frac{1}{Re_\tau} \nabla^2 D. \quad (2.3)$$

Here  $U(\mathbf{X}, t)$  is the Eulerian velocity given by  $U(\mathbf{X}, t) = (u, v, w)$  at a fixed point in space,  $\mathbf{X} = (x, y, z)$ , and at time  $t$ . The characteristic scales of duct flow used for non-dimensionalization of these equations are the duct hydraulic diameter,  $h$ , and mean friction velocity,  $u_\tau^a$ . The mean friction velocity here is known *a priori* from the imposed static pressure gradient,  $\Pi$ , used to derive the bulk flow in the homogeneous streamwise direction:

$$\tau_w^a = (u_\tau^a)^2 = \frac{\Pi}{4h} . \quad (2.4)$$

The term  $\Pi \delta_{ij}$  represents the imposed static pressure gradient along the homogeneous streamwise direction, where  $\Pi$  has a constant value of 4.0 and  $\delta_{ij}$  is the Kronecker delta. The imposed static pressure gradient is used to calculate the mean friction velocity for non-dimensionalization, even though the actual four-wall, spatially averaged friction velocity will slightly fluctuate in time about this mean value. The friction Reynolds number is defined as  $Re_\tau = hu_\tau^a / \nu = 300$ , where  $\nu$  is the kinematic viscosity of the Newtonian fluid. The present value of  $Re_\tau = 300$  corresponds to a bulk Reynolds number,  $Re_b \sim 4410$ , and a centerline Reynolds number,  $Re_c \sim 5880$  (Gavrilakis 1992). The dimensions of the square duct are  $4\pi h \times h \times h$  (see figure 2.1). In terms of wall units, the dimensions of the duct are  $L_x^+ = 3770$  and  $L_y^+ = L_z^+ = 300$ . The present streamwise length of  $L_x^+ = 3770$  wall units is sufficiently long to accommodate the streamwise-elongated near-wall structures present in wall-bounded turbulent shear flows (see section 3.1). These near-wall structures are rarely expected to be longer than about 1000 wall units in the streamwise direction (Robinson 1991). A uniform Cartesian grid of  $327 \times 195 \times 195$  is used, totaling about 12.43 million computational grid points. The grid resolution is  $\Delta x^+ = 11.67$  wall units in the streamwise direction and  $\Delta y^+ = \Delta z^+ = 1.57$  wall units in the wall-normal directions. The first grid point away from the wall is located at  $\Delta y^+/2 = \Delta z^+/2 = 0.79$  wall units, due to a staggered grid. The Kolmogorov length scale for this flow based on volume-averaged dissipation is estimated to be little over 2 wall units (Gavrilakis 1992). The present grid is therefore capable of resolving all the dynamically

significant length scales of interest here without requiring any sub-grid scale modeling. Unlike stretched grids, the present uniform grid maintains the small  $\Delta y^+$  and  $\Delta z^+$  values in the interior of the flow domain. The small fixed time step for time integration was  $\Delta t = 1.5e-4$  or equivalently  $\Delta t^+ = 4.5e-2$  time wall units, which gave a time-mean CFL value of about 0.28 in the present flow simulation. The parameters of relevance to the present DNS are summarized in a table in section 3.1.

## 2.2. Spatial and temporal discretization

The spatial derivatives in the equations above are discretized on a uniform staggered (Harlow & Welch 1965) Cartesian mesh using finite difference discretization. The inertial and viscous terms in the momentum equations are approximated in the interior of flow domain by fourth-order accurate central differences, and all other spatial derivatives in (2.1)-(2.3) are at least second-order accurate. Near the boundaries, all derivatives are second-order accurate with the exception of inertial terms for which a third-order accurate upwind-biased formula (Kawamura, Takami & Kuwahara 1986) is used, as in Deshpande (1993). The present duct flow code was rewritten from the 3-D cavity flow code of Deshpande (1993) by modifying most of its numerical procedure. A uniform Cartesian grid and the numerical implementation of velocity and pressure boundary conditions were retained from the cavity flow code while most other numerical procedures were rewritten altogether or modified. In the section below, emphasis will be placed on describing the numerical procedure of the present particle tracking DNS code. For details on numerical procedure of the lid-driven cavity flow code, the reader is referred to Deshpande (1993).

We will now discuss the exact form of numerical approximation for spatial and temporal derivatives in the code. As in Deshpande (1993), a uniform staggered Cartesian grid was used for the finite difference spatial discretization. In the Navier-Stokes equations, the inertial terms assume greater significance as the Reynolds number increases and therefore require special attention when using finite differences. The aliasing errors can be present in the flow solution due to inadequate resolution of the

small (yet energetic) scales whose unbounded energy growth can easily destabilize the code. Second-order finite differences are believed to be more prone to the growth of these aliasing errors in turbulence simulations and one popular approach is to use some suitable upwind-biased formula. Upwind-biased formulae are compact unlike the regular upwind formulae, which require a larger stencil of grid points. Upwind-biased formulae are inherently dissipative in nature, damping out the high frequency content in the energy spectrum thereby providing good aliasing error control. Precisely which part of the energy spectrum gets damped out is difficult to predict and sometimes an undesirable damping of a certain frequency component in the spectrum results. Rai & Moin (1991) presented a fifth-order accurate upwind-biased formula that was demonstrated to provide good aliasing error control in their finite difference based turbulent flow simulations. We would like to mention here that initially the fifth-order accurate upwind-biased formula of Rai & Moin (1991) was used in the present code, but was later abandoned due to its high-order dissipation preventing the growth of small perturbations.

In the present code, we use the standard fourth-order accurate central difference formulae in the interior along with a third-order accurate upwind-biased formula and the standard second-order accurate central difference formulae near the walls. The standard fourth-order accurate central differences have high-order accuracy and generate much less aliasing errors than their second-order counterparts. The standard fourth-order accurate central difference formula for the second derivative approximation is

$$\partial^2 u_i / \partial x_i^2 = \{-u_{i+2} + 16u_{i+1} - 30u_i + 16u_{i-1} - u_{i-2}\} / 12\Delta x_i^2 + O(\Delta x_i^4). \quad (2.5)$$

The above fourth-order accurate spatial discretization is used for the diffusive terms in the interior of the flow domain. The standard second-order accurate formula is used near the boundaries for diffusive terms:

$$\partial^2 u_i / \partial x_i^2 = \{u_{i+1} - 2u_i + u_{i-1}\} / \Delta x_i^2 + O(\Delta x_i^2). \quad (2.6)$$

The convective terms are approximated in the interior of the flow domain by the standard fourth-order accurate central difference formula

$$u_i \partial u_i / \partial x_i = u_i \{u_{i-2} - 8u_{i-1} + 8u_{i+1} - u_{i+2}\} / 12\Delta x_i + O(\Delta x_i^4), \quad (2.7)$$

which is identical to the first term on the right hand side of the third-order accurate upwind-biased formula given below in (2.8). A third-order accurate upwind-biased formula (Kawamura *et al.* 1986) is used for the convective terms near the boundaries:

$$u_i \partial u_i / \partial x_i = u_i \{u_{i-2} - 8u_{i-1} + 8u_{i+1} - u_{i+2}\} / 12\Delta x_i - |u_i| \{-3u_{i-2} + 12u_{i-1} - 18u_i + 12u_{i+1} - 3u_{i+2}\} / 12\Delta x_i + O(\Delta x_i^3). \quad (2.8)$$

As in Deshpande (1993), the above expression is written for both  $u_i > 0$  and  $u_i < 0$  in order to avoid an expensive IF statement in the computer program for checking the sign of  $u_i$  every time. Due to its above form, the coefficients of  $u_{i-2}$  to  $u_{i+2}$  returned for  $u_i > 0$  case are  $\{-2, 4, -18, 20, -4\}$  while for the  $u_i < 0$  case they are  $\{4, -20, 18, -4, 2\}$ . The original lid-driven cavity flow code of Deshpande (1993) used this third-order accurate upwind-biased formula for convective terms in the entire domain and second-order accurate central differences for the diffusive terms in the entire domain. A variation of the original (viscous) cavity flow code of Deshpande (1993) is described for the case of (inviscid) Euler equations in Deshpande & Sharma (1999). Upwind or upwind-biased formulae provide stability due to high-order dissipation of any aliasing errors, but can also spoil the solution quality due to some over-dissipation. Therefore, higher-order central differences only were chosen in this code for most of the domain (i.e. away from the boundaries).

The momentum equations are integrated in time using an explicit, second-order accurate Adams-Bashforth method. The first step for the Adams-Bashforth time integration scheme is started in the code using a low-storage, third-order accurate Runge-Kutta method. The original code of Deshpande (1993) used first-order accurate Euler explicit scheme for time integration. The explicit, two-step, second-order accurate Adams-Bashforth (AB2) method is given by

$$u^{n+1} = u^n + (3/2) \Delta t f(u^n) - (1/2) \Delta t f(u^{n-1}) + O(\Delta t^2). \quad (2.9)$$

The explicit, three-stage, low-storage, third-order accurate Runge-Kutta method (lsRK3) of Williamson (1980) is given by

$$\begin{aligned} u_0 &= u^n \\ q_1 &= \Delta t f(u_0) \quad ; \quad u_1 = u_0 + (1/3) q_1 \\ q_2 &= -(5/9) q_1 + \Delta t f(u_1) \quad ; \quad u_2 = u_1 + (15/16) q_2 \end{aligned}$$

$$q_3 = - (153/128) q_2 + \Delta t f(u_2) \quad ; \quad u_3 = u_2 + (8/15) q_3$$

$$u^{n+1} = u_3 . \tag{2.10}$$

Depending on the size of time step, the time stepping errors can be made satisfactorily small in the simulation using the present AB2 method. In one set of test simulations, the laminar duct flow was computed using different grid sizes and successively smaller fixed time steps. The second-order AB2 method yielded results very close to those from the third-order lsRK3 method, with identically small time steps. The stability region of lsRK3 (and RK3) is wider than the explicit AB2 method (see discussion in Peyret 2002, pp. 130-152). Since the time step used here was well below that required by the CFL criterion or the viscous time scale, any instability due to the time step was unlikely in the present simulation. Since it was decided to keep the time step small in the simulation, the cost of time marching would be large from a multi-stage method like the low-storage Runge-Kutta method of (2.10). The lsRK3 would be three times more expensive than AB2 due to the repeated computation of function values. For this reason, it was not incorporated for the main part of time integration in the final version of the code even though it was used in an earlier version. The third-order accurate lsRK3 does not require any significant additional storage other than that already available in the code for a second-order accurate AB2 time integration. The explicit, second-order accurate Adams-Bashforth method with a fixed small time step is the standard method of time integration of the momentum equations in this study. Since the AB2 method is not self-starting, the lsRK3 will be used to generate the flow field corresponding to the first time step of a simulation.

The pressure Poisson equation is solved using a fast Poisson solver algorithm (an optimized and parallelized version of the NAG numerical library function D03FAF). The NAG routine D03FAF is based on the fast Poisson solver algorithm of Swarztrauber & Sweet (1979) that uses fast sine transforms in the  $x$  and  $y$  directions and solves tri-diagonal matrices in the  $z$ -direction (see also Swarztrauber 1984). Note that the routine generates the finite difference equations for Poisson equation using second-order accurate discretization formulae. The resulting linear system of equations is then solved efficiently

using the fast sine transforms and the tri-diagonal matrix algorithm (TDMA). Most of the computational time in solving the Poisson equation by the fast Poisson solver algorithm is devoted to the computation of multiple one-dimensional sine transforms and the tri-diagonal matrix inversion. Despite this efficient algorithm compared to other iterative techniques like conjugate gradients, it is desirable to further reduce the computational time. The two computationally intensive operations (sine FFTs and TDMA) in the algorithm were parallelized using shared memory (OpenMP) parallelization. The fast solution of the pressure Poisson equation in serial and parallel versions of the code allowed a fine uniform mesh and a small time step in the present simulation.

The numerical implementation of boundary conditions for velocity and pressure are identical to that in Deshpande (1993). Second-order accurate polynomial curve fitting is used to numerically simulate the velocity values for points lying outside the domain but needed by finite difference formulae in the interior. Pressure boundary conditions are derived using a no-slip condition in the continuity and momentum equations. The use of a staggered grid necessitates some kind of interpolation in the evaluation of two staggered velocity components while computing the non-linear terms along any direction. As in Deshpande (1993), the present flow code uses bilinear interpolation using four neighboring grid points to obtain the two staggered velocity components at the location of the third velocity component. A bicubic interpolation scheme was tested for this code earlier but was later abandoned for the bilinear scheme due to the high computational cost of the former. The accuracy of this interpolation is crucial in keeping the velocity dilatation magnitudes small. It is planned to incorporate a more efficient form (involving sparse matrix multiplication) of bicubic interpolation scheme in future versions of the code. The present code however uses bilinear interpolation only. The cost of computation for bilinear interpolation is very small and this simplest form of interpolation is a tradeoff between acceptable accuracy and speed of computation. All computations reported in this thesis are performed in double-precision arithmetic with O2 level of optimization in FORTRAN 90 compilers. The O2 level of optimization does not alter the semantics of computation in either serial or parallel (double-precision) computations.

### 2.3. Lagrangian equations of motion

We now turn to the numerical issues in Lagrangian particle tracking. We consider particles with inertia and passive tracers, point-like (imaginary) particles with vanishing inertia with respect to the advecting fluid. A passive tracer has a very simple equation describing its motion compared to that for a high inertia particle e.g. an aerosol. Even though, the equation is simple, the Lagrangian particle motion is not unless the flow is no more than steady two-dimensional (see the review article by Ottino 1990). The particle equations of motion given here are also non-dimensionalized by the duct hydraulic diameter ( $h$ ) and mean friction velocity ( $u_\tau^a$ ). The Lagrangian and Eulerian fluid velocities are related for a passive tracer particle by

$$\frac{d\mathbf{X}_p}{dt} = \mathbf{U}_p(t) = \mathbf{U}(\mathbf{X}, t), \quad (2.11)$$

where  $\mathbf{X}_p(t)$  is the particle position at time  $t$ ,  $\mathbf{U}_p(t)$  is the Lagrangian velocity of a particle at time  $t$ . The instantaneous location of a particle at time  $t$  is given by  $\mathbf{X}_p(t)$  and the instantaneous particle velocity at this moving point is  $\mathbf{U}_p(t)$ .

The Lagrangian motion of a rigid, spherical particle suspended in a flow is governed by a force balance equation that is described in detail by Maxey (1987). Even though a number of possible forces (including Stokes drag, lift, gravity, virtual mass, Basset history, etc.) can act on a finite-inertia particle, many of these may be neglected without any appreciable loss of accuracy, depending on the particle inertia. The most important force acting on the finite-inertia particle is the Stokes drag force. Gravity may be another important force to include depending on the geometrical orientation of the flow of interest. We neglect the shear-induced Saffman lift force (Saffman 1965) here because it only assumes non-trivial magnitudes in the viscous sublayer. Even in the viscous sublayer, it has been found to be an order of magnitude smaller than the normal component of the Stokes drag force (McLaughlin 1989). Particle deposition data obtained by DNS computations of McLaughlin (1989) and others have revealed that, depending on the particle inertia, there is only small difference in the statistical results from simulations



performed with and without consideration of the lift force. Furthermore, the Saffman lift force becomes less important for particles with large particle-fluid density ratios or large response times (defined below). As a consequence, the Saffman lift force may be neglected without any appreciable loss of accuracy in the statistical results. In the present computations we consider the linear Stokes drag as the only significant force acting on a finite-inertia particle. As a further simplification we have assumed one-way fluid-particle coupling so that the particles are affected by the fluid motion but not vice-versa. This assumption is reasonable if the suspended particles are small in size compared to the Kolmogorov length scale ( $\eta$ ) of flow and for the case of low-mass loading.

The finite-inertia particles considered here are assumed to be rigid, spherical and assumed to have a density much higher than that of the fluid (i.e.  $\rho_p/\rho_f \gg 1$ ), in order for the assumption of point forces to be valid. With all of the above assumptions, the non-dimensional force balance equation takes the form

$$\frac{d\mathbf{U}_p}{dt} = \frac{\mathbf{U} - \mathbf{U}_p}{\tau_p}. \quad (2.12)$$

The term on the right hand side represents the effect of the linear Stokes drag force. The dimensionless particle response time,  $\tau_p$  (or  $\tau_p^+$  in wall units), is a measure of the relative importance of particle inertia and fluid acceleration and is defined here as

$$\tau_p = \frac{\rho d_p^2 Re_\tau}{18}, \quad (2.13)$$

where  $\rho$  is the particle-fluid density ratio ( $\rho = \rho_p/\rho_f$ ) and  $d_p$  is the dimensionless particle diameter. In the present non-dimensionalization, the dimensionless particle relaxation time is equal to the commonly used Stokes number. The particle relaxation time alone appears as a parameter in the particle equations of motion, implicitly containing information about particle size and particle-fluid density ratio (hereafter referred to as the density ratio). Therefore the choice of this parameter is crucial as it largely determines the particle dynamics in a specified flow field. In the present study, we use a range of  $\tau_p^+$  values between 0 and 300. Here,  $\tau_p^+ = 0$  refers to the passive tracer

particle for which only the 3-dimensional dynamical system formed by (2.11) needs to be integrated. For a finite-inertia particle, the 3-D form of (2.12) is integrated first, followed by (2.11), thus forming a six-dimensional dynamical system. The density ratio for the finite-inertia particles is chosen to be  $\rho = 763$ , which corresponds to olive oil droplets in air at 25°C,  $\rho = 2083$  (glass microspheres), or  $\rho = 7333$  (copper microspheres). Having chosen the value of  $\tau_p^+$ , the density ratio determines the particle diameter, which is important for deposition. In the present simulations, the selected density ratios yield particle diameters that are smaller than the estimated Kolmogorov length scale for this flow.

The governing equations of particle motion are integrated using the standard fourth-order accurate Runge-Kutta (RK4) method. A small fixed time step equal in size to the Eulerian flow advancement time step is used to advance the particle trajectories as well. To perform this numerical integration, the Eulerian velocities of fluid motion are required at intermediate points in the computational domain where they are not defined as a part of the numerical solution. These velocities are calculated using an interpolation scheme using fluid velocities at neighboring grid points. The accuracy and speed of this interpolation scheme is important. Rovelstad, Handler & Bernard (1994) have tested the performance of three different interpolation schemes (trilinear, bicubic splines and tricubic interpolation) for particle tracking in DNS of a plane channel flow and analyzed their relative accuracy in predicting particle motion in a wall-bounded turbulent flow. Rovelstad *et al.* (1994) found tricubic interpolation particularly attractive since it provided high accuracy, fast computation and continuous first-order derivatives of interpolated velocities. In the present study, we employ a tricubic interpolation scheme using eight neighboring grid points surrounding the point of interest on the original 3-D staggered grid arrangement. The tricubic interpolator developed here requires the values of fluid velocity, its three first derivatives and four cross-derivatives at all the eight neighboring points located at the vertices of the nearest parallelepiped containing the point of interest. The function values are available directly from DNS while its derivatives and cross-derivatives are calculated using standard second-order accurate

central differences. The tricubic interpolation scheme ensures continuity and differentiability of the interpolated fluid velocities.

The initial particle velocity of any simulation was set equal to the undisturbed Eulerian fluid velocity at that point. This initial particle velocity was also calculated using the tricubic interpolation scheme. We use periodicity in the streamwise direction for particles as well, allowing particle tracking over larger displacements in the  $x$ -direction. A particle is considered deposited after it reaches a distance from the wall that is equal to or less than its radius (as determined by 2.13). The particle tracking DNS code was also parallelized using shared memory (OpenMP) parallelization and some of the computations reported in this thesis were performed using up to 4 processors. The parallelization of the particle tracking code and its parallel performance will be discussed later in section 2.5.

#### **2.4. Tricubic interpolation on 3-D staggered grid**

The numerical integration of the particle equations of motion requires a numerical estimate of flow velocity,  $\mathbf{U}$ , at arbitrary locations occupied by particles in the computational domain. As part of the flow solution, the flow velocity ( $\mathbf{U}$ ) is readily available at the computational grid points only. It must be obtained at the arbitrary points corresponding to particle locations using some suitable interpolation scheme. This interpolation scheme must be attractive in terms of its accuracy, speed of computation and continuity of derivatives of the interpolated functions. A spectral interpolation scheme using e.g. Fourier series or Chebyshev polynomials would undoubtedly be the most accurate but impractical at the same time due to its high computational cost when tracking a large number of particles and/or a long time integration. A suitable alternative is thus desired which is sufficiently accurate for the present purpose and fast enough at the same time. Rovelstad *et al.* (1994) have tested the accuracy and speed of computation for trilinear, bicubic splines and tricubic interpolation schemes in DNS of a particle-laden turbulent channel flow. Their tests concluded the superior accuracy of tricubic interpolation when compared to the other two. Apart from being least accurate, trilinear

interpolation does not provide continuous first-order derivatives of the interpolated velocities, which is highly undesirable for the present purpose. In the tests performed by Rovelstad *et al.* (1994), interpolation using bicubic splines was found to cause relatively larger errors in computed particle trajectories in the wall-bounded flow (a plane channel) studied by them. In light of this, we have chosen tricubic interpolation scheme for the present study.

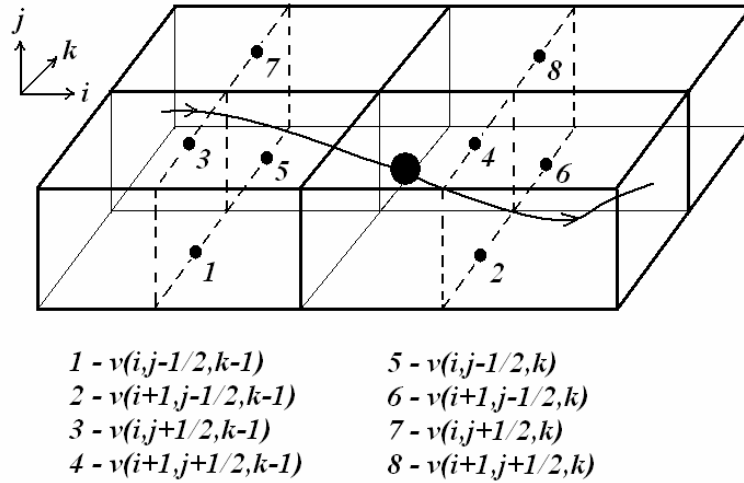


Figure 2.2. Schematic of a particle moving through the 3-D staggered grid. Shown also are the eight neighboring grid points (at cell faces) used for interpolating fluid velocity at its location.

In a tricubic interpolation scheme, if the point of interest is located at  $(x, y, z)$  location, the three linear parameters are constructed on the 3-D grid (containing the eight neighboring grid points, as shown in figure 2.2) as

$$l_1 = \frac{(x - x_l)}{(x_u - x_l)} \quad , \quad l_2 = \frac{(y - y_l)}{(y_u - y_l)} \quad , \quad l_3 = \frac{(z - z_l)}{(z_u - z_l)} \quad (2.14)$$

where the lower and upper bounds in the  $x$ -direction are denoted by  $x_l$  and  $x_u$  respectively, and similarly for  $y$  and  $z$  directions. These three linear parameters ( $l_1, l_2, l_3$ ) vary between 0 and 1 depending on the value of  $x, y$  or  $z$  at the point of interest (figure 2.3). Tricubic interpolation involves constructing a third-order polynomial using these three linear parameters. A constant coefficient matrix (WT3D) was derived by generating the 64 simultaneous equations at the eight neighboring grid points and then solving the resulting

64 x 64 linear system of equations using direct matrix inversion in MATLAB. Once this constant coefficient matrix WT3D is derived outside the main program, it is called and used in the same form every time for use on any grid size (or code) as long as there are eight neighboring (Cartesian grid) points involved in the interpolation.

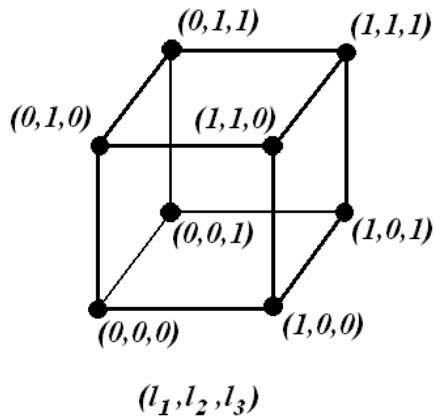


Figure 2.3. The values assumed by three linear parameters at the eight grid points in tricubic interpolation.

Interestingly, the constant coefficient matrix WT3D is found to be sparse with only 1000 elements out of the total 4096 being non-zero. The degree of sparsity is high, as about 75% of the elements are zero. However, the sparse matrix is not in one of the standard forms (see figure 2.4 below) thus posing difficulty in any effort towards its further simplification to allow efficient computation and storage. It was found that there were only ten different non-zero elements,  $\{1, 2, 3, 4, 6, 8, 9, 12, 18 \text{ and } 27\}$ , appearing in the rows and columns of this sparse matrix, along with some repetition in order. It was therefore decided to explicitly code them into a subroutine, thus allowing the multiplication with non-zero elements only of the matrix instead of the whole 64 x 64 matrix using e.g. FORTRAN 90 intrinsic function MATMUL. This made the computation faster as well as improved the speed-up in shared-memory parallelization.

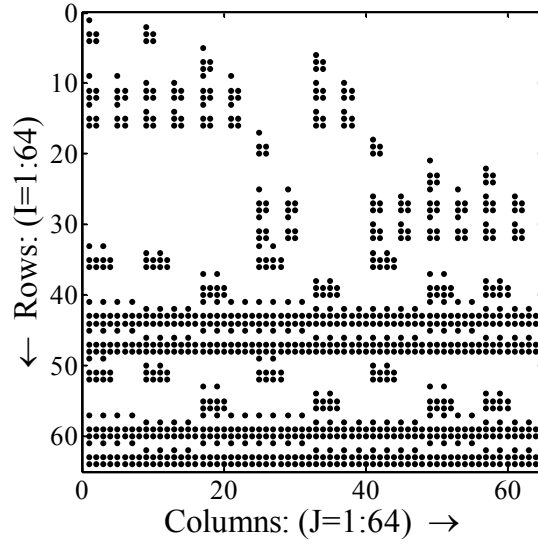


Figure 2.4. Sparse structure of the constant coefficient matrix, WT3D.

Note that the three first-order derivatives, three second-order cross-derivatives and one third-order cross-derivative of fluid velocities will be needed at each of the eight neighboring grid points by the tricubic interpolation scheme. The function values (i.e. velocities) at the eight neighboring grid points are available from the numerical solution of Navier-Stokes equations at those grid points. The derivative values were evaluated here using standard second-order accurate central differences. These function and derivative values along with the constant coefficient matrix WT3D were used for evaluation of the variable coefficients  $c_{ijk}$  at every individual particle location. Once the coefficient matrix  $c_{ijk}$  has been computed using the constant coefficient matrix WT3D and the user supplied values of the velocities and their derivatives etc. at the eight neighboring grid points, the evaluation of the interpolated velocity and its derivatives is straightforward.

The tricubic interpolation is carried out using the formula

$$f(x, y, z) = \sum_{i=0}^3 \sum_{j=0}^3 \sum_{k=0}^3 c_{ijk} l_1^i l_2^j l_3^k . \quad (2.15)$$

Moreover, its three derivatives and four cross-derivatives can be obtained easily and efficiently once the interpolation operator has been computed above, e.g.

$$f_x(x, y, z) = \sum_{i=0}^3 \sum_{j=0}^3 \sum_{k=0}^3 ic_{ijk} l_1^{i-1} l_2^j l_3^k \quad (2.16)$$

$$f_{yz}(x, y, z) = \sum_{i=0}^3 \sum_{j=0}^3 \sum_{k=0}^3 jkc_{ijk} l_1^i l_2^{j-1} l_3^{k-1} \quad (2.17)$$

$$f_{xyz}(x, y, z) = \sum_{i=0}^3 \sum_{j=0}^3 \sum_{k=0}^3 ijkc_{ijk} l_1^{i-1} l_2^{j-1} l_3^{k-1} \quad , \quad (2.18)$$

and similarly for other derivatives and cross-derivatives. The derivative values of interpolated velocities were not needed in the present particle tracking and therefore were not computed. However, as can be seen above, these are computationally very efficient to evaluate after the coefficient matrix  $c_{ijk}$  has been evaluated once, unlike in case of interpolation using bicubic splines.

In order to locate the position of a particle, a search must be performed to find the index of its position in the computational grid in each of the three directions separately. In its simplest form of implementation, it can be a highly wasteful and computationally expensive operation if every time a search is started (using the expensive IF statements) from the left end of the table of values (i.e. grid points). One of the more general-purpose yet quite efficient method of search is the bisection method (see figure on page 112 in Press *et al.* 1992), which converges to the right index in the table in about  $\log_2 N$  tries. A careful look at the present problem suggests that a particle's point location coordinates at time  $t^{n+1}$ , owing to a small time step, will not change appreciably from those at  $t^n$ . This implies that the point location coordinates will be strongly correlated with themselves in time. An index correlated search algorithm is given in Press *et al.* (1992), which uses the searched value from the previous search to quickly locate the new index value in the present search. At best, this index search algorithm can be a factor of  $\log_2 N$  faster than the bisection method. The present code incorporates the method of index-correlated

search since it is the best choice for the present problem. However, it requires the (integer) storage of indices from the last search for all the points, which can be quite large depending on the number of particles being tracked. However, the memory requirement for integers is small and in any case the reduction in computational time derived from this very fast search completely outweighs any such (small) limitations.

## 2.5. Particle tracking code parallelization

To obtain meaningful statistical results, the particle trajectories have to be integrated for a sufficiently long time. Depending on the number of particles being tracked, this can be an enormously expensive computational task. In some cases, the computational cost of tracking an ensemble of suspended particles over one time step may far exceed that of the corresponding flow DNS time step. This renders the direct simulation of particle-laden flows a prohibitively expensive computational task. Thus parallelization becomes necessary in these cases.

The shared memory parallelization was implemented in the FORTRAN 90/77 code using OpenMP compiler directives. For testing the parallel code performance, an instantaneously frozen turbulent flow field was used. The trajectories of a total of 160000 particles were advanced at each time step. Parallelization of the code is implemented in a way that the total number of particles to be tracked,  $N$ , can be divided among processors at each time step. Note that  $N = \text{NPT} * \text{NTT}$  where  $\text{NTT} =$  number of different particle response times and  $\text{NPT} =$  number of particles for each particle response time. The chunk of job on each processor or thread was thus  $N/\text{NTH}$  or  $(\text{NPT} * \text{NTT})/\text{NTH}$ , where  $\text{NTH}$  is the number of processors or threads. For a total number of  $N = 160000$  particles, there were  $\text{NPT} = 40000$  particles for each of the  $\text{NTT} = 4$   $\tau_p^+$  values. The job was divided such that at each time step, each thread tracks the  $\text{NPT}/\text{NTH}$  particles of particle response time, say  $\tau_p^+ = 1$ , followed by  $\tau_p^+ = 5$ , 10 and finally the passive tracer  $\tau_p^+ = 0$ . Separate subroutines are written for tracking the finite-inertia particles and passive tracers while both these subroutines use the same interpolation scheme. There is a choice of two interpolation schemes in the code: tricubic interpolation and trilinear interpolation. Only



tricubic interpolation was used in the present study. It was found best to divide the job among processors for a large number of particles, instead of the three individual directions of a particle trajectory. Further, dividing the job among the (equal-sized) ensembles of particles to be tracked leaves the problem open to possible scalability so that more than three processors can be assigned to carry out the job in parallel. How efficient the job is completed compared to the serial job is where implementation of parallelization comes into the picture.

The OpenMP compilers allow distributed-shared memory (DSM) parallelization on DSM machines like SGI Origins and IBM p690. The array initialization using a *first-touch policy* was performed outside the time integration loop in the main program. The outer loop running for NPT particles was parallelized while the inner loop for particle type (i.e.  $\tau_p^+$  value) was left serial. Running index as  $IPT = 1, NPT$  in the outer loop ensures a better cache utilization of the array data in addition to providing any desired chunk size to suit the varying number of processors available for parallelization. Having initialized the array data on individual threads, it was possible to get good access by local processors for all the data that they need to write to. However, there are large-sized arrays from flow field, like the 3-D velocity arrays, which are not written to during the particle tracking time step and are read only by the interpolation subroutine. These were made `THREADPRIVATE` and copied onto each thread's local memory using `COPYIN` compiler directives. This data distribution was required to be performed at each time step as the velocity arrays from the Eulerian flow simulation did not warrant any permanent data distribution in the flow part of the code. The above data distribution using `COPYIN` along with the first touch policy based data initialization proved efficient for the parallelization of the present code. This was demonstrated through very good speedup and efficiency (discussed below) of the particle tracking code.

The results of code performance are presented below for computation performed on the SGI Origin 3800 (K2) and IBM p690 (Agave) parallel computers at the Texas A&M Supercomputing Facility. In the parallel code performance results to be described below, a total of  $N = 160000$  particles were tracked in an instantaneously frozen turbulent flow

field obtained using a direct numerical simulation on a  $259 \times 165 \times 165$  grid and a duct of size  $[L_x, L_y, L_z] = [4\pi, 1, 1]$ . The Reynolds number based on duct hydraulic diameter and mean friction velocity was  $Re_\tau = 300$ . At Texas A&M Supercomputing Facility, a larger number of threads could be requested easily in the interactive mode than in a batch-processing mode, partly because of the long queues for batch processing on both these machines. The performance on a larger number of CPUs could be tested on these machines in the interactive mode only. In order to reduce the memory requirements of the code so that it could be run in the interactive mode, the  $259 \times 165 \times 165$  grid generated flow field was transferred to a coarser grid of size  $131 \times 99 \times 99$  using tricubic interpolation. In the case of an instantaneously frozen turbulent flow field, a longer time integration could be performed using a somewhat larger time step of  $\Delta t = 5.0e-03$ . The results shown below represent the second best performance recorded from among a set of 10 repeated identical runs in the interactive mode. The fluctuations in the parallel performance in these 10 repeated identical runs were small.

Figure 2.5(a) shows parallel code speedup on 12 threads of the 64-processor SGI Origin 3800 (K2). The maximum number of threads available on this machine was limited to 12 in the interactive mode, which was more than twice of that available in the batch mode for a single user. The speedup is indeed very good up to 12 threads tested here and the parallel performance can be seen to scale very well on this machine. The typical CPU time spent in parallel regions was  $t = 713.97$  sec. with  $N_{TH} = 1$  (speedup,  $S_{N_{TH}} = 1.00$ ) and  $t = 65.00$  sec. with  $N_{TH} = 12$  ( $S_{N_{TH}} = 10.98$ ). On the 32-processor IBM p690 (Agave), the speedup is very good up to 32 threads tested here (figure 2.5b). A large number of threads could be tested easily on this machine in the interactive mode only. The parallel performance can be seen to scale very well on this machine also. The typical CPU time spent in parallel regions was  $t = 330.01$  sec. at  $N_{TH} = 1$  ( $S_{N_{TH}} = 1.00$ ) and  $t = 10.39$  sec. at  $N_{TH} = 32$  ( $S_{N_{TH}} = 31.76$ ). Computations on Agave gave an additional speedup of about 2.16 for this code even in the serial mode. Note that this additional speedup is not added to the speedup shown in figure 2.5(b) below.

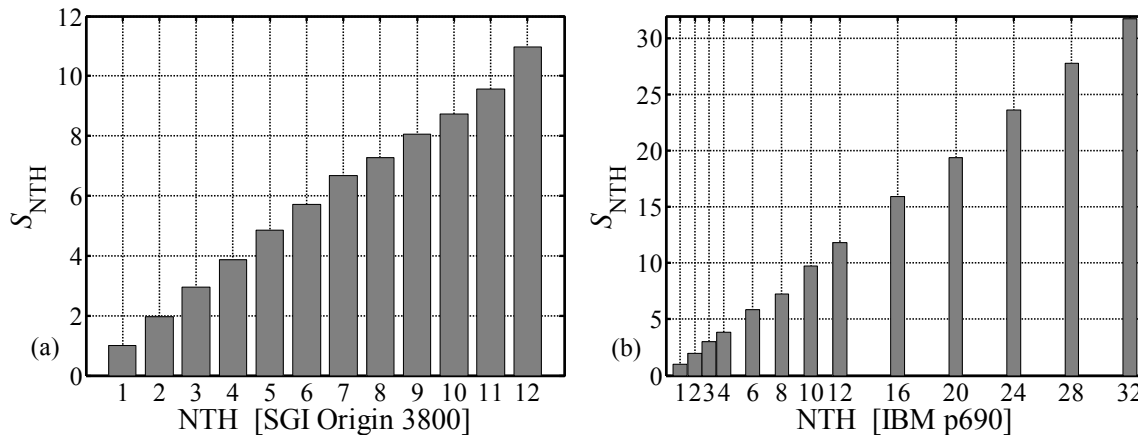


Figure 2.5. Parallel performance of the particle tracking code on SGI Origin 3800 and IBM p690 parallel supercomputers.

The efficiency of parallelization,  $\eta_{NTH}$ , is defined in terms of the CPU time (unlike wall-clock time in  $S_{NTH}$  shown above) used in serial and parallel modes of computation. It was found that every worker thread in the team uses nearly the same amount of CPU time as the master thread in the parallel region (implying low overhead cost). The efficiency did not drop appreciably even when NTH was increased on both these machines. On K2, typical values of efficiency were  $\eta_{NTH} = 94.96\%$  at  $NTH = 6$  and  $\eta_{NTH} = 90.75\%$  at  $NTH = 12$ . On Agave, typical values of efficiency were  $\eta_{NTH} = 98.51\%$  at  $NTH = 12$  and  $\eta_{NTH} = 99.25\%$  at  $NTH = 32$ . The lowest value observed in these tests on Agave was  $\eta_{NTH} = 89.39\%$  at  $NTH = 8$ , which is also quite high. These parallel performance results indicate that the particle tracking code parallelization is highly efficient.

Another set of tests was done later with a dynamically evolving DNS flow field on K2 using 4 processors requested in the batch mode. No notable differences in particle tracking parallel code performance were found in the parallel performance between an instantaneously frozen flow field and a dynamically evolving flow field or between an interactive mode and a batch mode. The particle tracking code performance is not affected either by the choice of flow type or whether the flow is steady or unsteady/turbulent. The choice of a static (i.e. instantaneously frozen) flow field in the parallel performance tests shown above was motivated by the need for a longer time integration (along with a larger time step) and to run the code in an interactive mode.

With this we conclude our discussion of the numerical procedure for DNS and Lagrangian particle tracking. The turbulent flow simulation and Lagrangian particle tracking in the instantaneously evolving DNS flow field will be discussed below in Sections 3 and 4, respectively.

### 3. TURBULENT FLOW SIMULATION

This section describes the turbulent flow simulation and the comparison of computed flow statistics with the published DNS results of Gavrilakis (1992). The statistically stationary turbulent flow field generated here will be used as the flow initial condition for all Lagrangian particle transport computations described later in Section 4.

#### 3.1. Flow parameters and turbulence simulation

The present low Reynolds number turbulent flow was simulated using the numerical procedure of sections 2.1-2.2 and perturbed laminar flow initial conditions. The series solution form of laminar duct flow was taken from Pozrikidis (2001). The perturbed laminar flow initial condition in the streamwise direction is shown in figure 3.1. The choice of initial laminar flow state and perturbations determine the time a perturbed basic state will take to become fully turbulent. In a direct numerical simulation, this initial time is also important since each time step of simulation is computationally very expensive.

---

Reynolds number,  $Re_\tau = 300$

Domain size,  $L_x = 4\pi$  and  $L_y = L_z = 1.0$  or  $L_x^+ = 3770$  and  $L_y^+ = L_z^+ = 300$

Grid size,  $N_x \times N_y \times N_z = 327 \times 195 \times 195$  (~12.43 million grid points)

Grid resolution,  $\Delta x^+ = 11.67$  and  $\Delta y^+ = \Delta z^+ = 1.57$ . First grid point at  $y^+ = z^+ = 0.78$ .

Time step,  $\Delta t = 1.5e-04$  or  $\Delta t^+ = 4.5e-02$

---

Table 3.1. Flow simulation parameters in the present DNS.

---

Table 3.1 above lists the flow simulation parameters used in this study. In the present simulation, the laminar flow was perturbed using Gaussian random numbers in  $[-1, 1]$  with small initial perturbation amplitudes of  $1.0e-6$ . The perturbed flow field was allowed to evolve in time until a fully developed and statistically stationary turbulent flow state was reached. The initial grid size was  $259 \times 165 \times 165$  and the initial streamwise length

was  $3\pi$ . After the turbulent flow became fully developed, the flow field was transferred from the  $259 \times 165 \times 165$  grid to the  $327 \times 195 \times 195$  grid using the tricubic interpolation scheme. This transferred flow field was allowed to relax on the new grid for a few large eddy turnover times. It was then transferred from the  $3\pi$  duct length to a  $4\pi$  duct length using tricubic interpolation and periodicity. The flow field of the entire  $3\pi$  duct length was transferred to the first  $3\pi$  of the  $4\pi$  duct length, and the first  $\pi$  to the last  $\pi$  duct length on the new longer duct. This flow field was again allowed to relax for a few large eddy turnover times until the turbulent flow statistics became statistically stationary again.

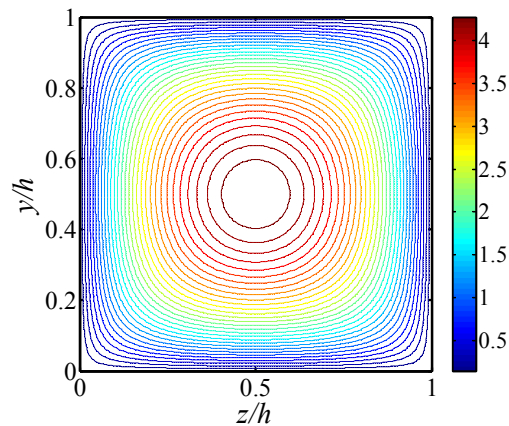


Figure 3.1. Contours of streamwise velocity in the initial (unidirectional) laminar flow.

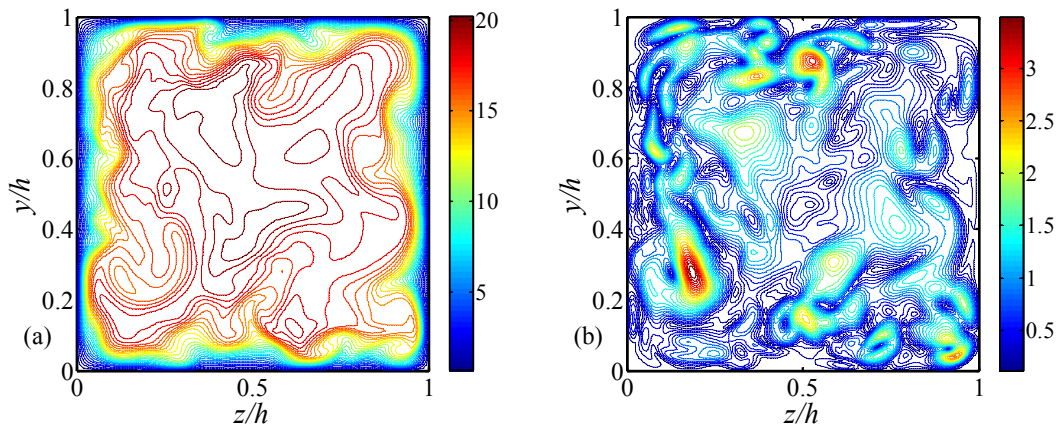


Figure 3.2. Contours of instantaneous turbulent (a) streamwise velocity and (b) secondary flow in a cross-sectional plane at  $x/h = 2\pi$ .

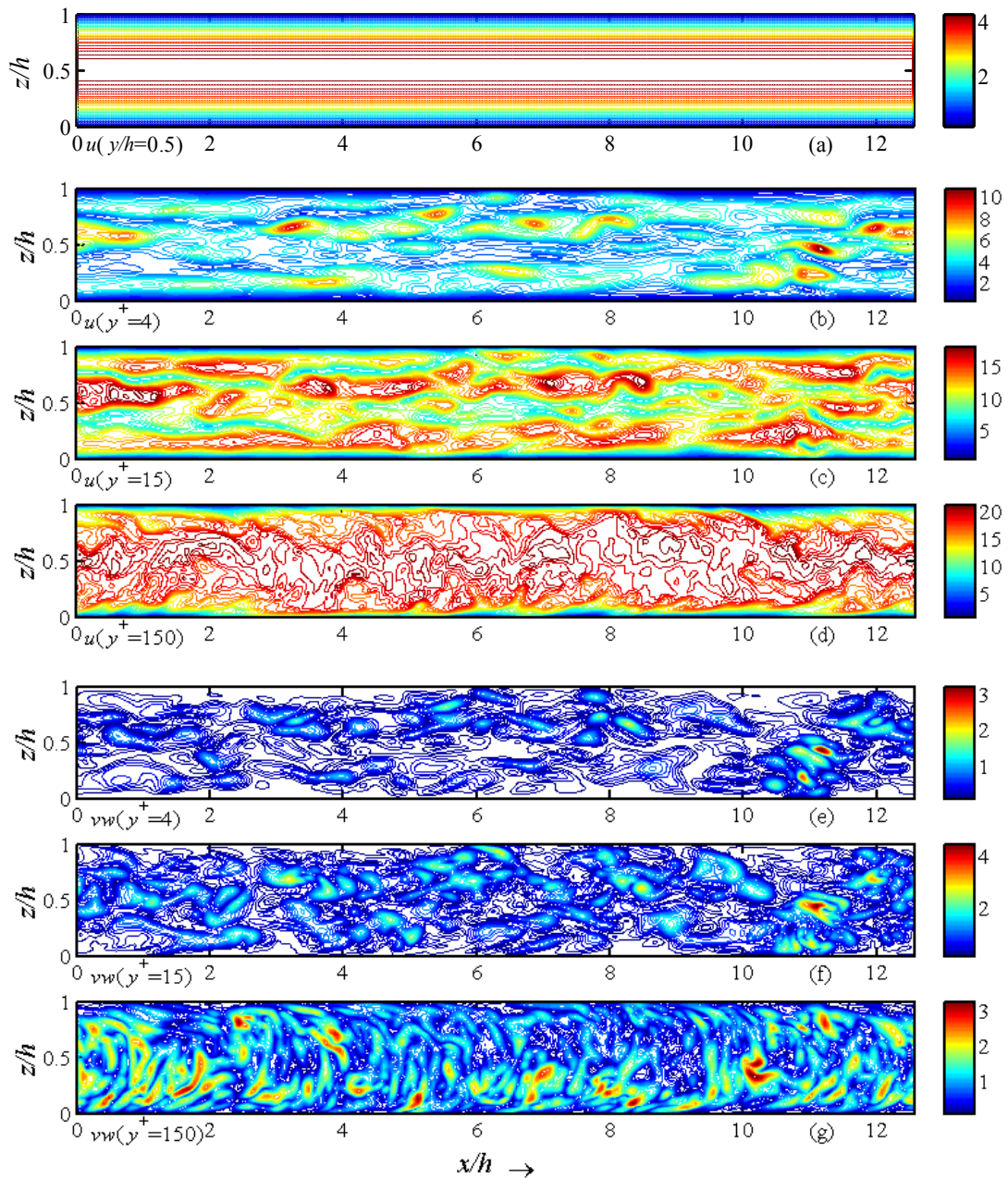


Figure 3.3. Contours of streamwise velocity at (a)  $y/h = 0.5$  in the laminar flow initial condition. Contours of instantaneous turbulent streamwise velocity at (b)  $y^+ = 4$  (c)  $y^+ = 15$  (d)  $y^+ = 150$ , and secondary flow at (e)  $y^+ = 4$  (f)  $y^+ = 15$  (g)  $y^+ = 150$ .

The final computational grid was  $327 \times 195 \times 195$  with a final duct length of  $4\pi$ . All the statistics of the Eulerian flow and Lagrangian particle transport reported in this thesis were obtained from this final configuration. Roughly 65 non-dimensional units of time

integration were required to progress from the perturbed laminar flow to the statistically stationary turbulent flow on the final grid and duct length. Once the flow had reached statistically stationary state on the final grid and duct length, the time was explicitly reset to zero again. This state was used as the fully developed turbulent flow initial condition for subsequent flow averaging and particle transport computations.

The laminar and turbulent velocity contours are shown in figures 3.1-3.3. The instantaneous turbulent velocity shown in these figures was interpolated to the planes shown using tricubic interpolation. The wall-normal distance is measured from the bottom wall for  $x$ - $z$  planes shown in figures 3.3(a-g). A time series was recorded (at every time step,  $\Delta t$ ) of the three Eulerian velocity components at three cross-stream locations for a very long duration of time (figure 3.4). Note that no interpolation was used for velocities shown in this figure and therefore the velocity components remain staggered as in the original grid arrangement. Since one-point velocity cross-correlations (involving two different components) shall not be computed here, the velocities being staggered by half grid spacing does not pose a problem. The points are in the viscous sublayer (around (8.00,0.02,0.75) or  $y^+ \sim 4$ ), buffer region (around (8.00,0.15,0.30) or  $y^+ \sim 45$ ) and outer layer (around (8.00,0.50,0.50) or  $y^+ \sim 150$ ). The turbulence intensities are higher at points around (8.00,0.15,0.30) than near the duct centerline i.e around point (8.00,0.50,0.50). Note the difference in magnitude of fluctuating wall-normal and spanwise velocity components around a point in the viscous sublayer near the wall. This point is located deep within the corner region of the square duct where a relatively small magnitude wall-normal velocity can be expected. The magnitude of spanwise velocity is larger than the wall-normal velocity at this point due to the sweeping motions of corner eddies.

Figure 3.5 shows the computed one-point auto-correlation coefficients ( $R_{uu}$ ,  $R_{vv}$  and  $R_{ww}$  at zero spatial lag values) at the locations corresponding to the velocity time traces of figure 3.4. As is expected in a fully developed turbulent flow, the velocity auto-correlations decay for large time lags. The area under the curve connecting global maximum (at zero time lag) and the first minimum in these decaying auto-correlation curves is considered adequate (Quadrio & Luchini 2003) to estimate the integral time



scale for a flow with sufficient accuracy. A conversion between space and time scales is possible using Taylor's frozen turbulence hypothesis. An estimate of the integral scales in the streamwise direction only is important here, in order to confirm that the present duct length can accommodate the longest turbulence structures. In many experiments, e.g. involving hot-wires, single-point measurements are more convenient than multi-point measurements (using e.g. an array of hot-wire probes) and integral length scales are obtained using Taylor's frozen turbulence hypothesis. On the other hand, in a DNS the two-point velocity correlations at zero time lag are more convenient. In the present DNS, we ascertain the adequacy of our duct length using two-point velocity correlations.

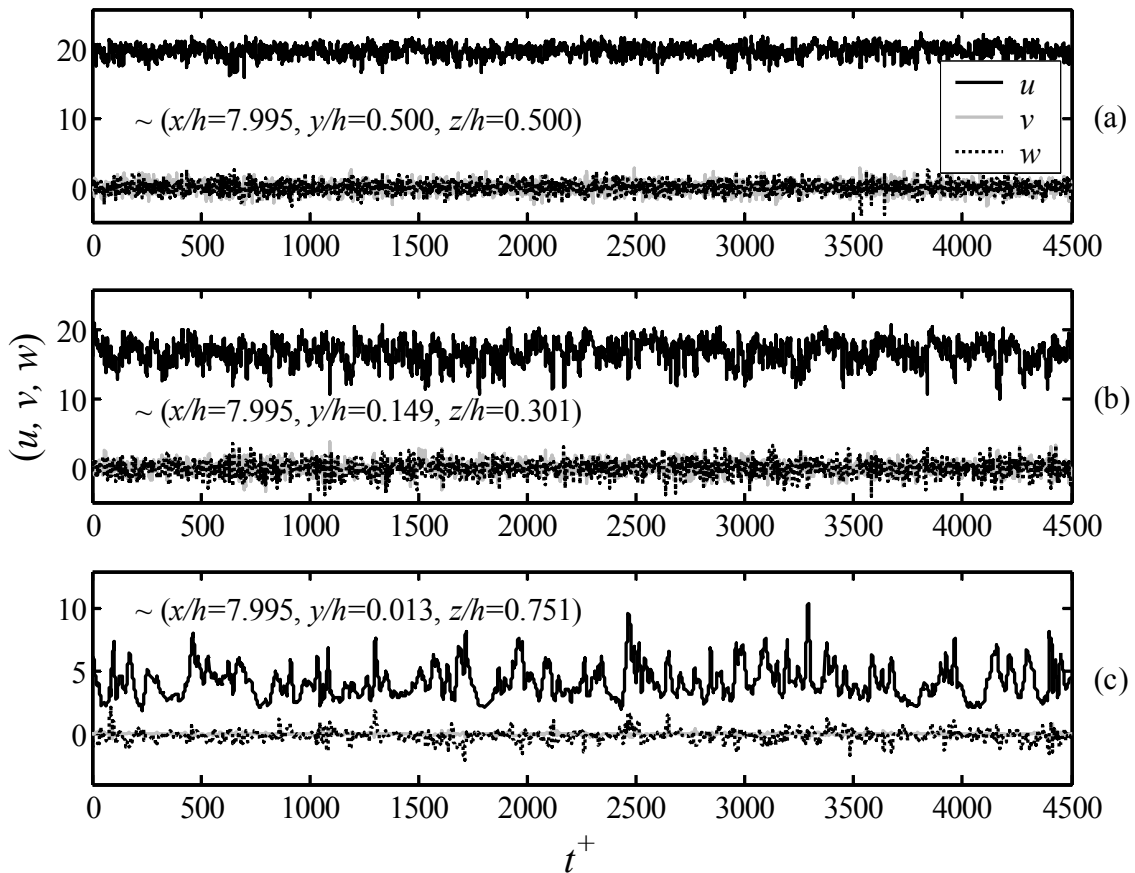


Figure 3.4. Instantaneous turbulent velocity time trace at three cross-stream locations.

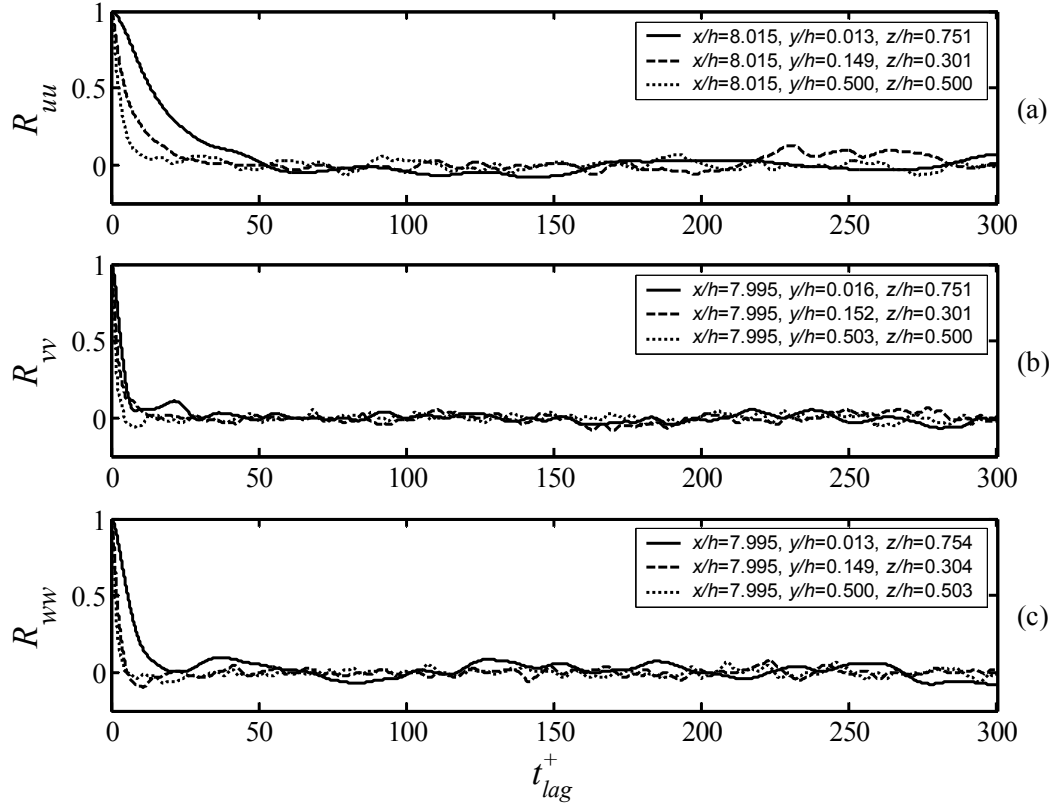


Figure 3.5. Coefficients of one-point velocity correlation at three cross-stream locations.

Figure 3.6 shows the variation of the coefficients of two-point cross-correlation ( $R_{uu}$ ,  $R_{vv}$  and  $R_{wv}$  at zero time lag) at four cross-stream locations and for all three velocity components. The two-point streamwise velocity cross-correlation coefficients (figure 3.6a) decay significantly over a streamwise length of  $L_x/2$ , thus demonstrating the adequacy of the present  $4\pi$  duct length. The small quasi-periodic fluctuation of these coefficients at large lags represents the re-introduction of turbulence structures in the computational domain due to  $x$ -direction periodicity. These secondary peaks are not a major cause of concern here due to their small magnitudes. The decay of the cross-correlation coefficients over  $2\pi$  spatial lag values suggests that the present  $4\pi$  duct length is adequate for accommodating the streamwise-elongated structures present in this turbulent flow.

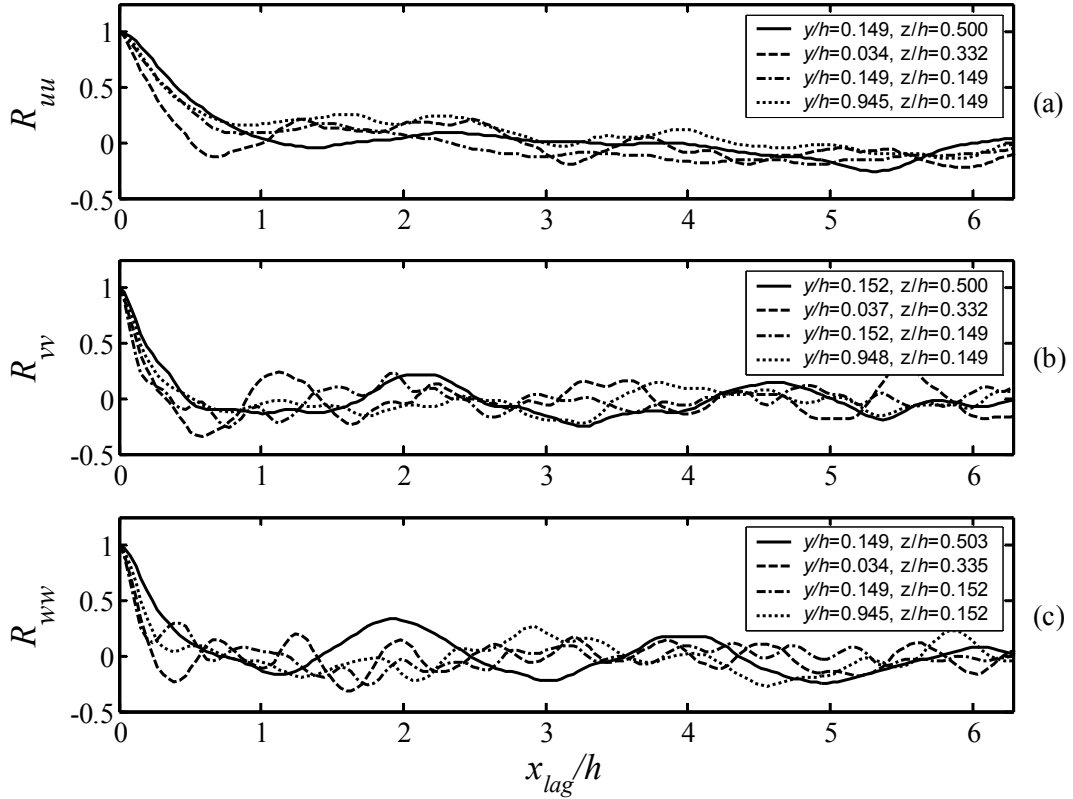


Figure 3.6. Coefficients of two-point velocity correlation at four cross-stream locations.

### 3.2. Flow verification

Before performing any Lagrangian particle tracking reported in this thesis, we have validated our numerical procedure through comparisons with the DNS results for the same flow and Reynolds number presented by Gavrilakis (1992). These comparisons are presented in figures 3.7-3.11 and table 3.2. Note that the  $y/h$  (or  $z/h$ ) label in these and other figures for any quadrant-averaged data (for both flow and particle transport results) represents the distance from the wall, irrespective of the actual  $y$  or  $z$  direction with respect to the fixed origin shown in figure 2.1. In figures 3.7-3.11, the solid lines represent the present DNS data while the circles represent data from the DNS simulation by Gavrilakis (1992). The Gavrilakis (1992) DNS data plotted here were obtained using DataTheif, a graphics reading software that requires manual selection of points on a scanned figure. The non-uniform spacing of circles representing the Gavrilakis (1992) DNS is due to this.

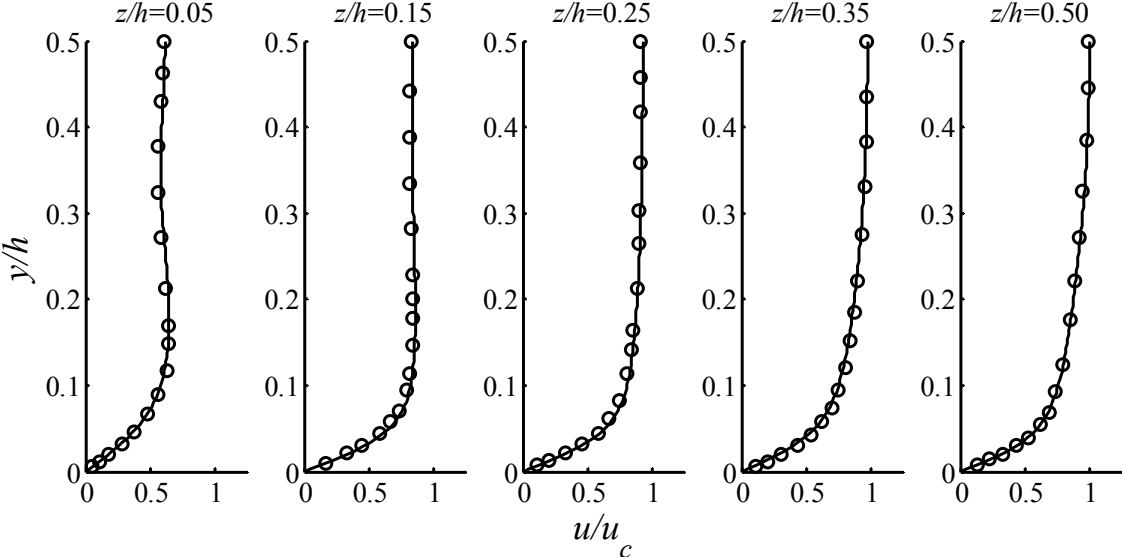


Figure 3.7. Quadrant-averaged profiles of the mean streamwise velocity at five spanwise locations. ( — ) Present DNS, ( ◯ ) Gavrilakis (1992).

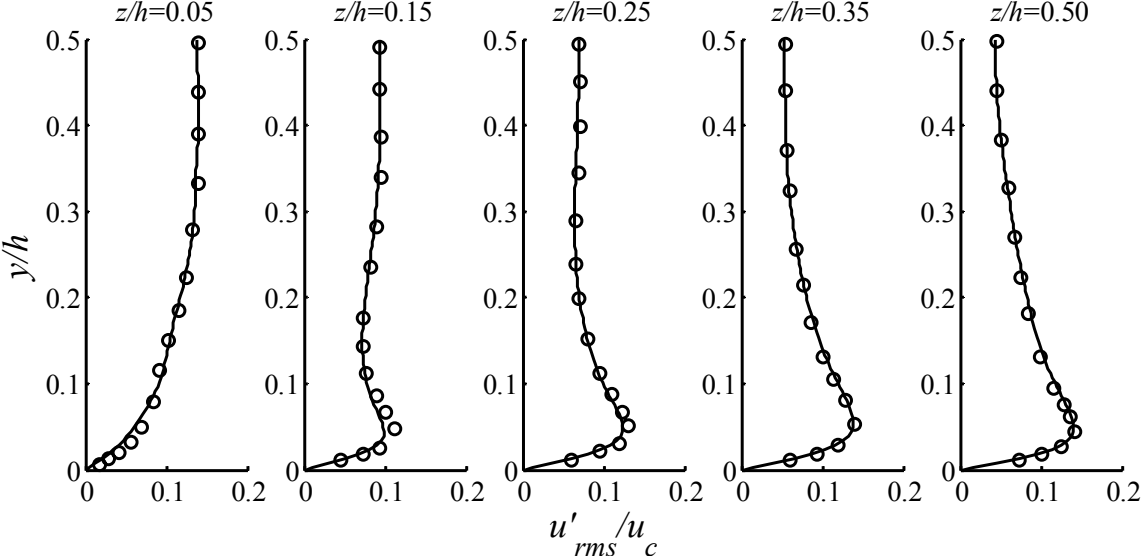


Figure 3.8. Quadrant-averaged profiles of the rms fluctuations in streamwise velocity at five spanwise locations. ( — ) Present DNS, ( ◯ ) Gavrilakis (1992).

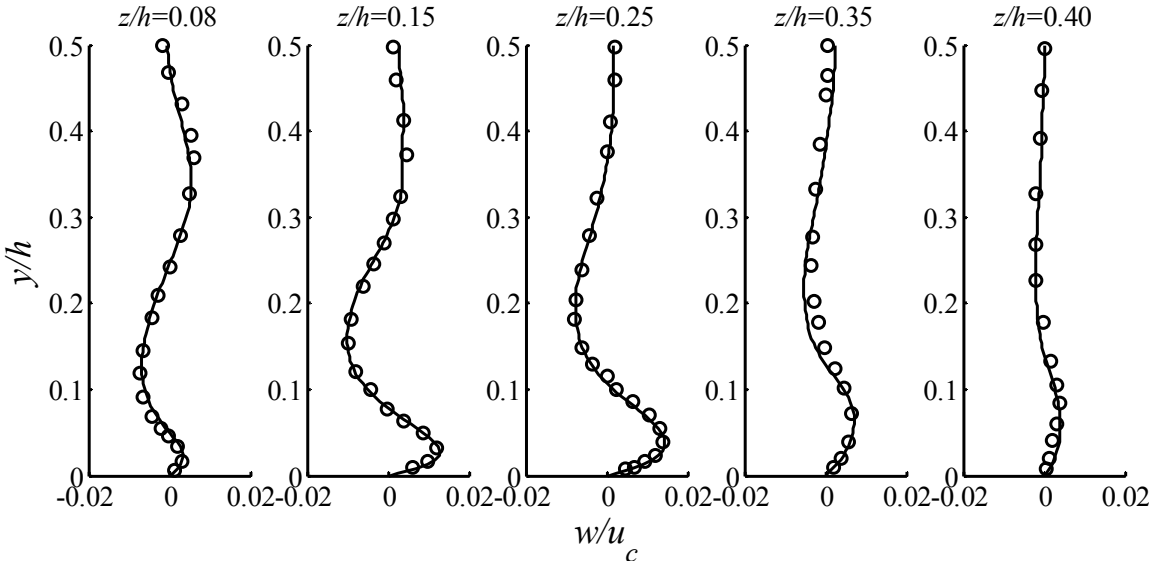


Figure 3.9. Quadrant-averaged profiles of the mean spanwise velocity at five spanwise locations. ( — ) Present DNS, ( ◯ ) Gavrilakis (1992).

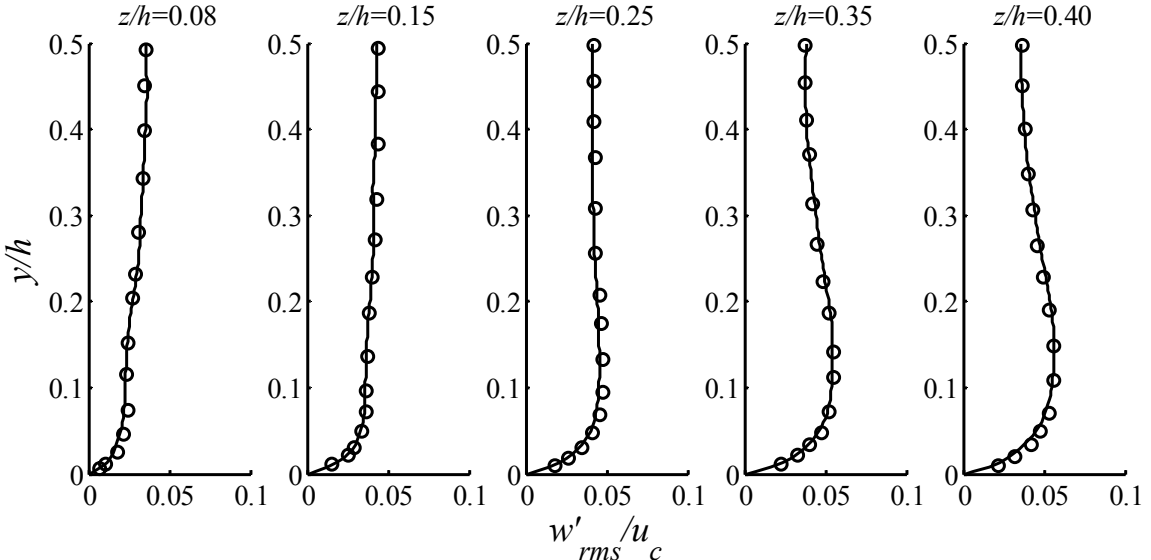


Figure 3.10. Quadrant-averaged profiles of the rms fluctuations in spanwise velocity at five spanwise locations. ( — ) Present DNS, ( ◯ ) Gavrilakis (1992).

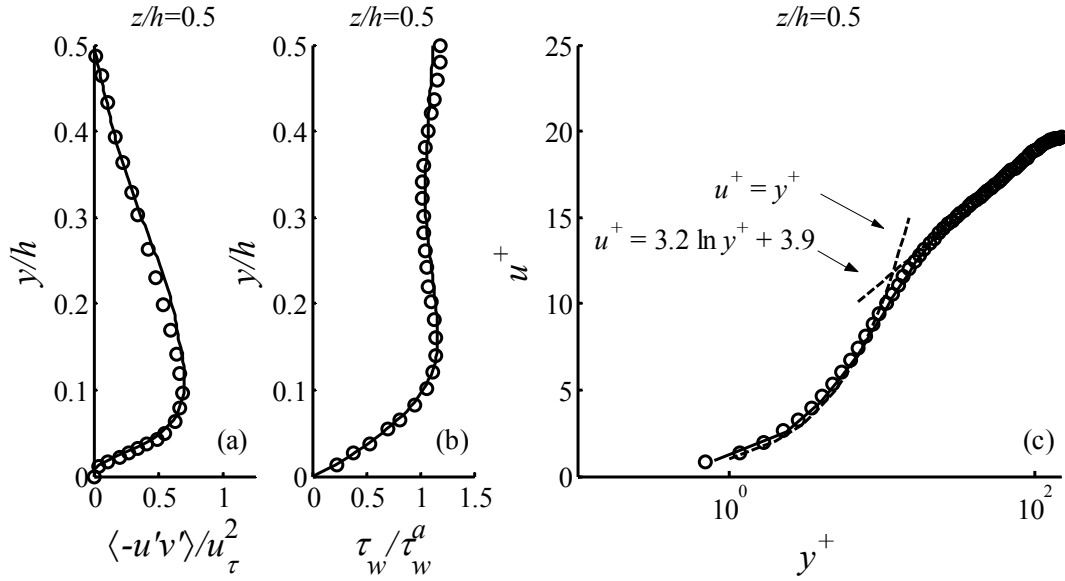


Figure 3.11. (a) Quadrant-averaged profile of the primary Reynolds stress component,  $\langle -u'v' \rangle$ , normalized by the local wall-friction velocity at mid-wall location. (b) Profile of wall shear stress as a function of distance along the wall and normalized by the average shear stress over the wetted area of duct. (c) Profile of mean streamwise velocity component at duct centerline on a log-linear scale and normalized by the mean friction velocity. Shown also is the corresponding profile from Gavrilakis (1992) DNS and profiles of the law of the wall and the log-law. In figures (a-c) above: ( — ) Present DNS, (  $\circ$  ) Gavrilakis (1992).

Computed Flow Quantity	Present DNS ( $Re_\tau=300$ )	Gavrilakis (1992) DNS ( $Re_\tau=300$ )	Vazquez & Metais (2002) LES ( $Re_\tau=393$ )
$u_c/u_b$	1.32	1.33	1.29
$\tau_w _{0.5}/\tau_w^a$	1.12	1.18	1.11
$u_{\tau 0.5}/u_\tau^a$	1.06	1.09	1.05
$F_f$	0.035	0.037	-
$u_\tau^a/u_b$	0.0663	0.0680	0.0655

Table 3.2. Comparison of flow quantities computed in present DNS and their corresponding values computed by Gavrilakis (1992) and Vazquez & Metais (2002).

Figures 3.7 and 3.8 display the quadrant-averaged profiles of the mean and fluctuating streamwise velocity components, respectively, at five spanwise locations of the square duct. Figures 3.9 and 3.10 display the mean and fluctuating spanwise velocity components at five spanwise locations. All of the velocity profiles in figures 3.7-3.10 are normalized by the mean value of the streamwise velocity at the duct centerline,  $u_c$ . Figure 3.11(a) shows the quadrant-averaged primary component of the Reynolds stress at the duct centerline. The Reynolds stress is normalized by the square of the mid-wall friction velocity computed in the simulation ( $u_{\tau|0.5}$ ). Figure 3.11(b) shows the computed wall shear stress profile as a function of distance along the wall. The wall shear stress is normalized by the average shear stress over the wetted area of the duct ( $\tau_w^a$ ). Note that the values of  $\tau_w^a$  and  $u_\tau^a$  are known from the imposed static pressure gradient and are both equal to unity in the present non-dimensionalization. Figure 3.11(c) shows the mean streamwise velocity profile on a log-linear scale along with the velocity profiles reported by Gavrilakis (1992) and the law of the wall and log-law profiles. Table 3.2 lists the numerical values of some other computed flow quantities along with their corresponding values from the Gavrilakis (1992) DNS and the isothermal LES of Vazquez & Metais (2002). The listed flow quantities are the ratio of computed mean centerline velocity to the bulk velocity ( $u_c/u_b$ ), ratios of the computed mid-wall shear stress to the four-wall averaged shear stress ( $\tau_{w|0.5}/\tau_w^a$ ) and the ratio of their corresponding friction velocities ( $u_{\tau|0.5}/u_\tau^a$ ), computed friction factor ( $F_f = 8(u_\tau^a)^2/u_b^2$ ) and the ratio of mean friction velocity to the computed bulk velocity ( $u_\tau^a/u_b$ ). It is clear from the figures 3.7-3.11 and table 3.2 that there is a generally good agreement between the present DNS and the DNS presented by Gavrilakis (1992). Other simulation data for a straight square duct are available from the LES by Madabhushi & Vanka (1991) at  $Re_\tau = 360$  and the DNS by Huser & Biringen (1993) at  $Re_\tau = 600$ . Gavrilakis (1992) data only is shown here for comparison with the present DNS due to the identical Reynolds numbers and the availability of detailed velocity profiles in that reference.

In this section we have discussed the simulation of turbulent flow in the straight square duct, starting from the perturbed laminar flow initial conditions. We have presented the turbulent flow statistics and compared them with the DNS results of Gavrilakis (1992) for the same flow and Reynolds number. Good agreement is observed for mean and fluctuating quantities as can be seen from the figures 3.7-3.11 and table 3.2. These results validate the present flow DNS code, which will now be used to generate the time evolving turbulent flow field for Lagrangian particle tracking in Section 4.



## 4. LAGRANGIAN PARTICLE TRANSPORT

We have obtained Lagrangian statistics of passive tracers and finite-inertia particles from four different problem formulations (Cases I-IV). Case I features the release of uniformly distributed particles in a plane at the duct inlet. Case II features the release of particles forming consecutive particle pairs in the core region of duct. Case III features the initially random distribution of particles in the flow domain. Case IV features the release of uniformly distributed particles in planes at different heights above the duct walls. Statistics on particle dispersion, concentration and deposition are obtained for each case.

### 4.1. Dispersed particles visualization

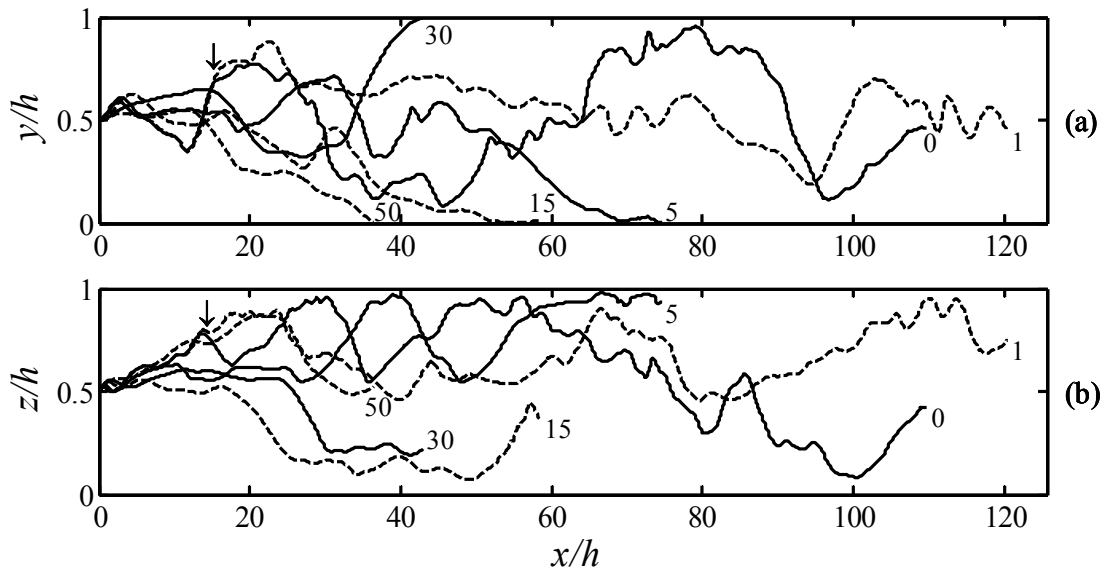


Figure 4.1. Effect of inertia on Lagrangian dispersion of particles released from the same point.

We begin our discussion of Lagrangian particle transport by considering the effect of inertia on typical trajectories of individual particles. Figure 4.1 demonstrates the effect of particle inertia on Lagrangian dispersion when particles are released from the same point

in space and time. Typical trajectories of particles with  $\tau_p^+ = 0, 1, 5, 15, 30$  and  $50$  and released at  $t^+ = 0$  on the duct centerline are shown. The trajectories deviate in time due to difference in their inertia values, despite identical conditions of fluid flow. Note that the trajectories of a passive tracer ( $\tau_p^+ = 0$ ) and a  $\tau_p^+ = 1$  particle remain initially very close and then suddenly diverge from each other (indicated with arrows in figures 4.1a-b). Similar observations are made for particles with identical inertia but with small initial inter-particle separation in space (or time). The particle pairs remain initially close for some time (which is a strong function of their initial inter-particle separation) before this inter-particle separation begins to grow quickly.

The effect of particle inertia on the Lagrangian particle motion is also evident from the time trace of particle velocities shown in figure 4.2, which displays time traces for four different inertia particles released from the same point on the duct centerline at  $t^+ = 0$ . Note that the identical inertia values in figures 4.1 and 4.2 do not correspond to the same individual particle. The velocity of a passive tracer particle is more sensitive to the turbulent fluctuations compared to the  $\tau_p^+ = 5$  particle or other higher inertia particle. There are times when the particle velocities remain significantly smaller than their time-mean values for up to a few large eddy turnover times (see the  $\tau_p^+ = 5$  velocity trace between approximately  $t^+ = 1025$  and  $t^+ = 1575$ ). Finite-inertia particles are thrown out of regions of high vorticity in the absence of a background rotation and tend to accumulate in regions of high strain rate (*preferential concentration*), such as in the interaction region of two or more adjacent vortices (see discussion in Provenzale 1999). These extended troughs in the particle velocity time trace likely represent the low velocity attained by a particle trapped in a region of high strain rate. The unpredictable nature of the velocity traces suggests that a large number of samples are needed in any average involving Lagrangian particle velocities, such as in the computation of velocity correlations.

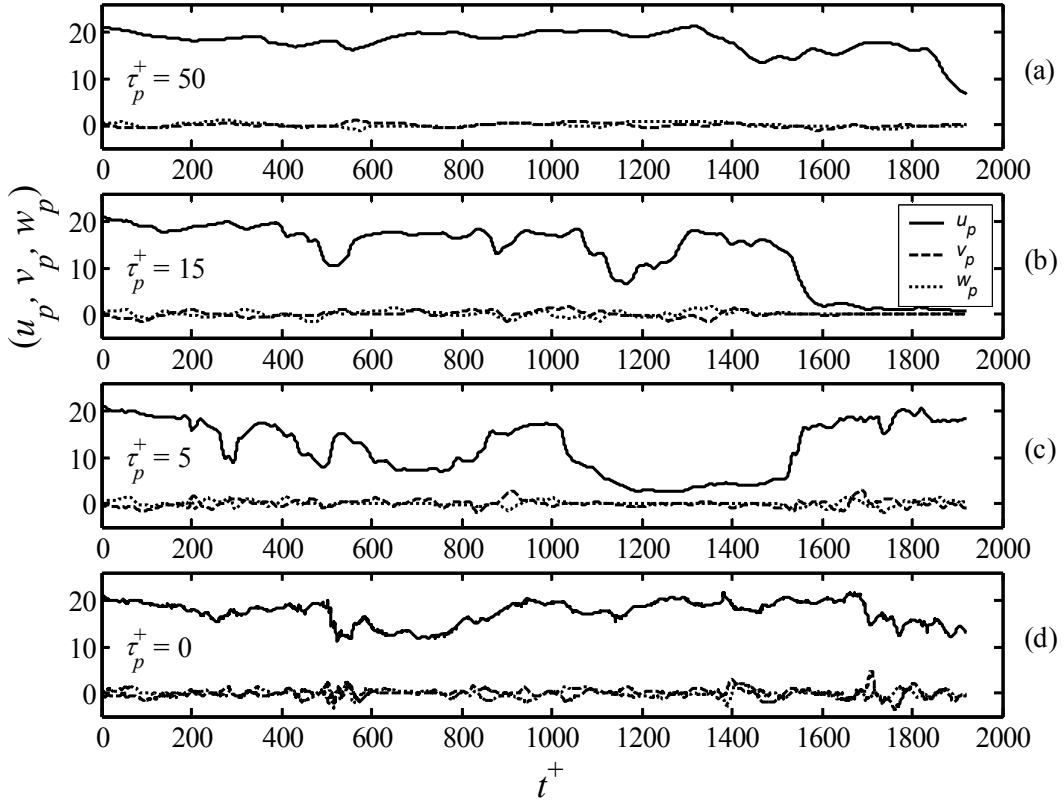


Figure 4.2. Particle velocity time trace for particles released from the same point at duct centerline.

The computation of Lagrangian velocity auto-correlations is needed for the estimation of Lagrangian integral time scales, which are important in the interpretations of similarity theory (see discussions in Sawford 2001; Yeung 2002). Due to the turbulence-induced variations in the trajectories of individual particles, averages from a large number of individual trajectories are required for auto-correlations. This is further complicated by the fact that finite-inertia particles can deposit on walls and their stagnant (zero) velocities after deposition can significantly skew the ensemble averages. Sometimes it is convenient to obtain a single long time trace of the velocity in a typical trajectory and then divide it into a number of time bins for obtaining ensembles. This is perhaps more suitable for exact flow solutions of unbounded flows, like the ABC flow studied by Wang *et al.* (1992), than for a direct numerical simulation.

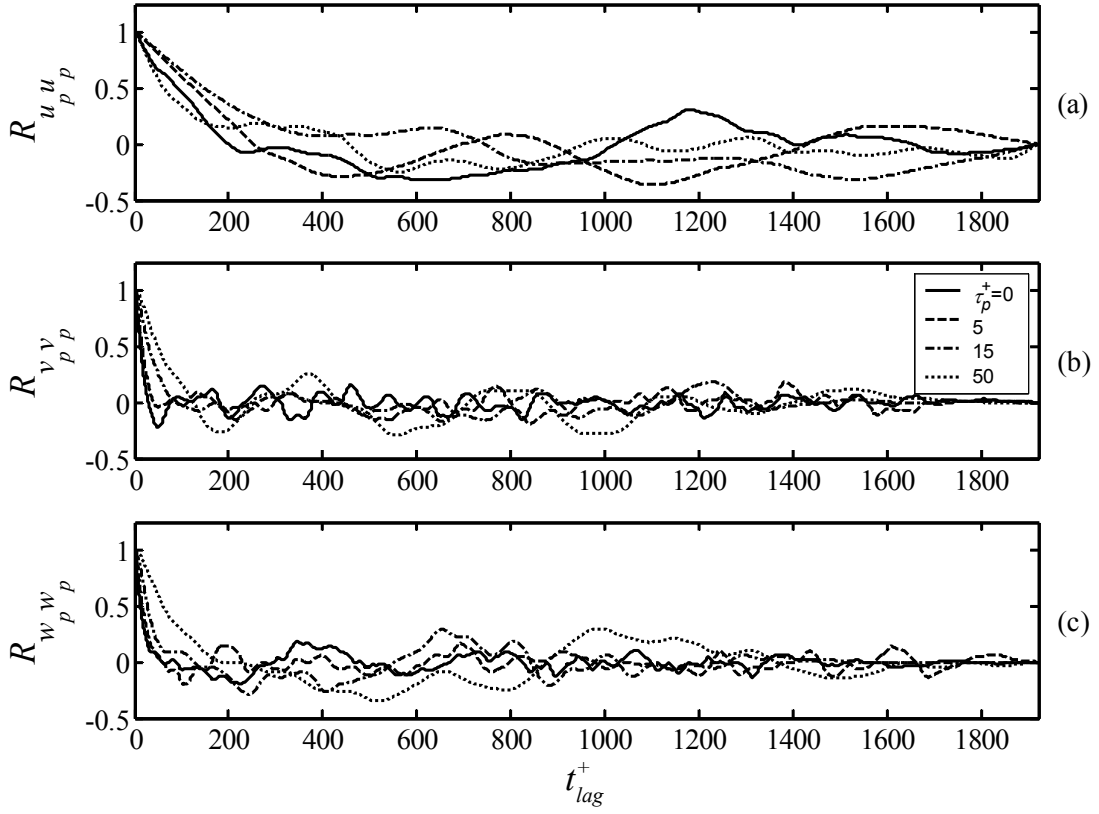


Figure 4.3. Coefficients of Lagrangian velocity auto-correlation from a typical trajectory.

Here, we have not computed the ensemble-averaged Lagrangian velocity auto-correlations needed for more accurately estimating the Lagrangian time scales, etc. For a less accurate (but expected to be quantitatively close) estimate of the effect of particle response time on Lagrangian velocity auto-correlation, we compute them from the velocity time trace of a typical single particle only. The particle velocity time trace considered for the computation of Lagrangian velocity auto-correlation coefficients,  $(R_{u_p}, R_{v_p}, R_{w_p})$  in figure 4.3 is the same as in figure 4.2. The Lagrangian auto-correlation coefficients computed here are typical of a single particle trajectory and should be viewed in that light only. However, since the particle inertia values here are not very close, a qualitative estimate of the effect of inertia on Lagrangian velocity auto-correlation is still possible from the single particle trajectory data of an un-deposited particle. The auto-correlations decay fast for low inertia values, thus corresponding to a smaller value of the

integral time scale. The location of the first minima in these auto-correlation curves is important for an adequately accurate estimation of the integral time scale. We do not discuss further the computations of any Lagrangian integral time scales for this flow since the trajectory data shown here is only for illustration of a typical single particle data set. Figures 4.4(a-d) below display the four different initial conditions for release of particles in simulations of Case I – IV. These simulations will be discussed in detail in the sections 4.2 and 4.3 below.

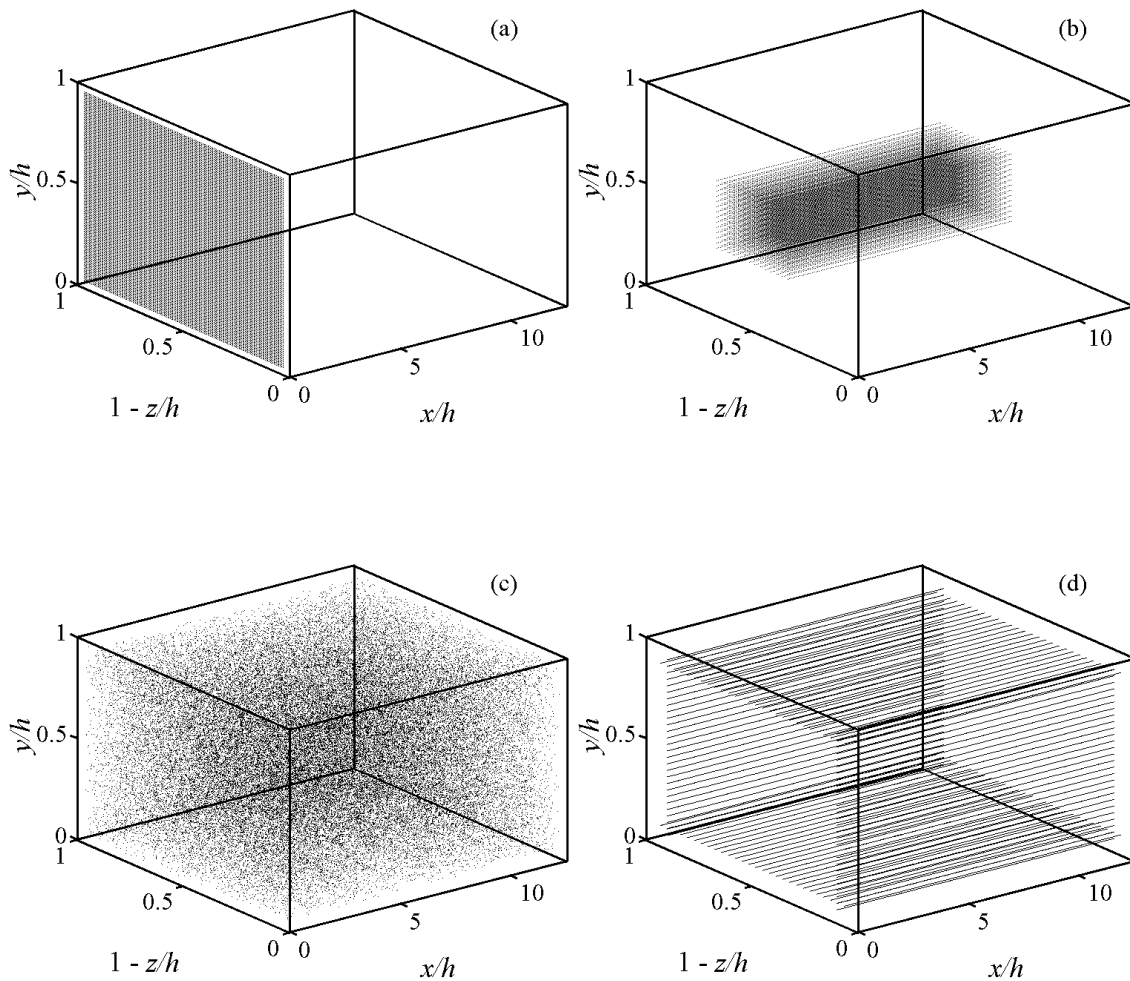


Figure 4.4. Initial distribution of particles in the domain for (a) Case I, (b) Case II ( $r_0^+ = 24.0$  shown), (c) Case III and (d) Case IV ( $y_0^+ = 30$  shown).

It is well known that an initially uniform distribution of particles becomes highly non-uniform in time in a turbulent flow. In inhomogeneous wall-bounded turbulence, preferential concentration is characterized and enhanced by the near-wall coherent motions of the turbulent boundary layer. Figures 4.5 and 4.6 show snapshots of the dispersed particles in the turbulent straight square duct for  $\tau_p^+ = 15$  (figures 4.5a-d) and  $\tau_p^+ = 0$  (figures 4.6a-d) after an initial release within the viscous sublayer ( $y_0^+ = 3$ ). Figures 4.5(a-d) below show the particle locations in an  $x$ - $z$  plane and a  $y$  bin of width 30 wall units ( $0 \leq y^+ \leq 30$ ), corresponding to a top view of the bottom wall.

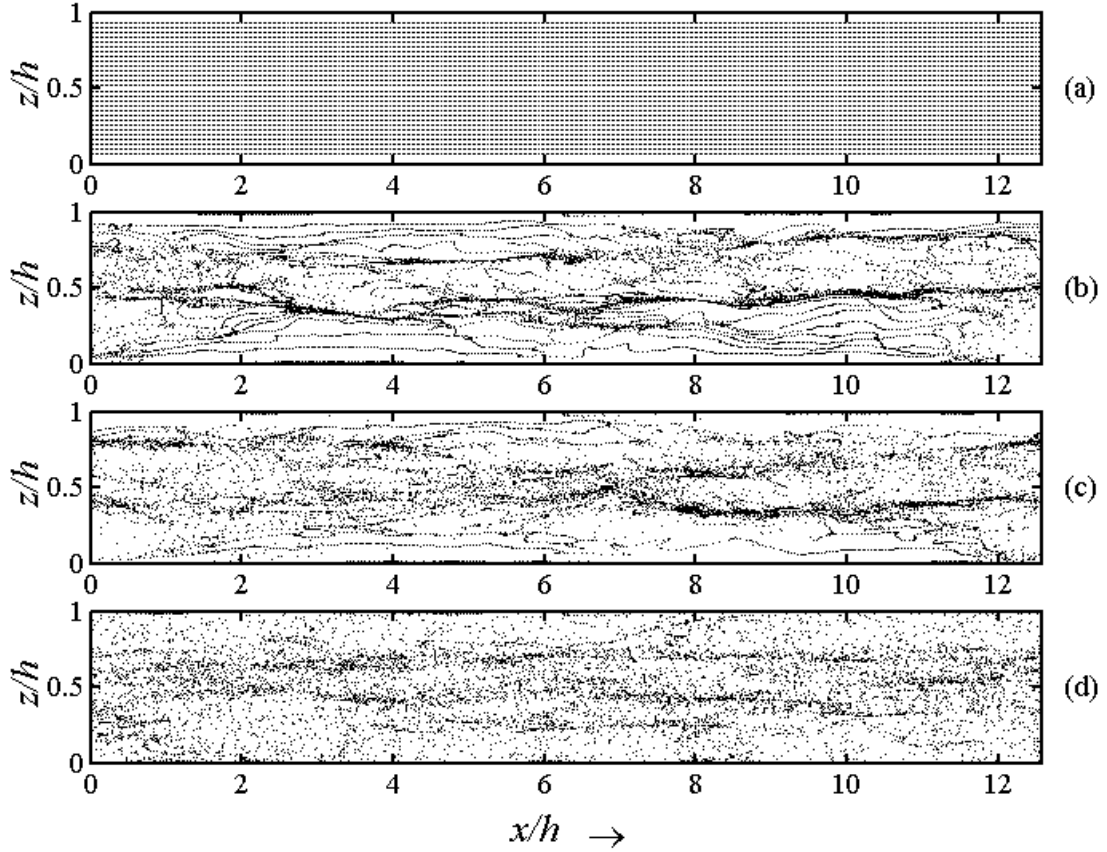


Figure 4.5. Instantaneous particle positions for  $\tau_p^+ = 15$  particles at  $t^+ =$  (a) 0, (b) 135, (c) 265 and (d) 675 for an initial release height of  $y_0^+ = 3$  (Case IV simulation). Particles are visualized in the  $x$ - $z$  plane and a  $y$  bin of width 30 wall units from the bottom wall.

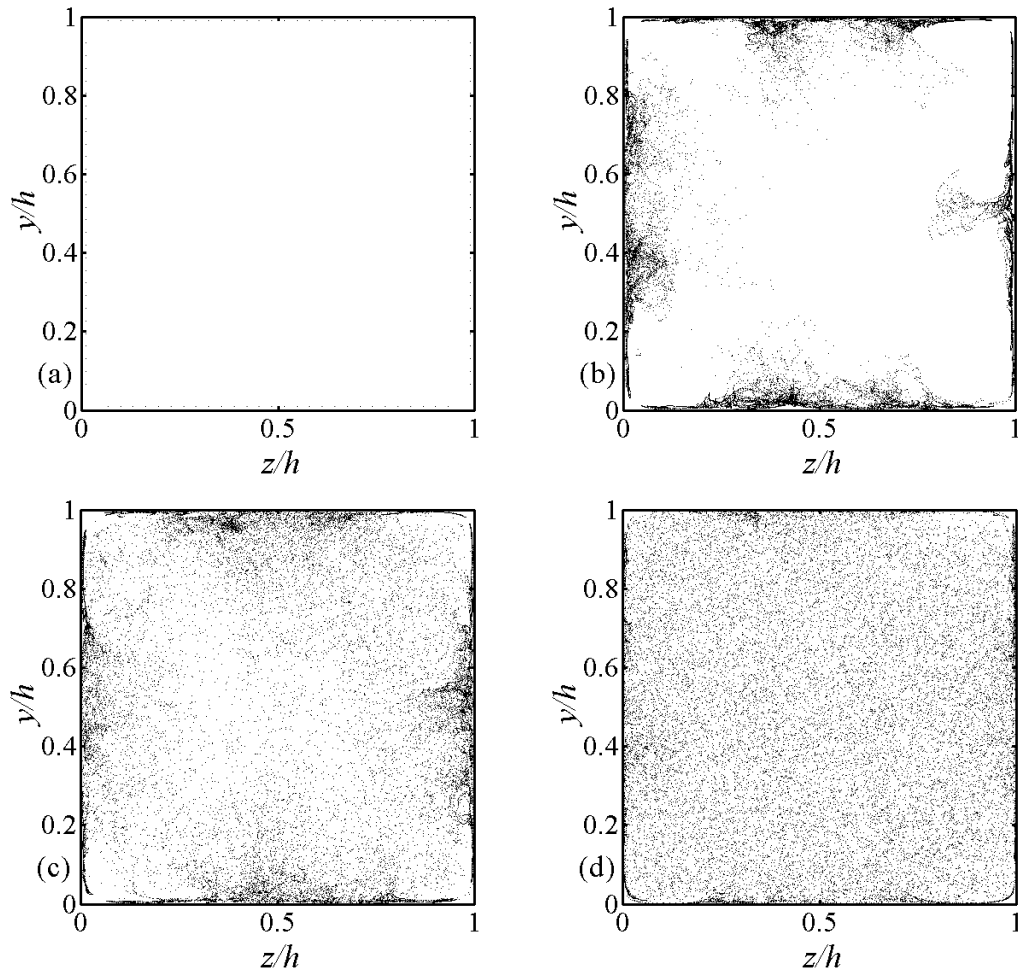


Figure 4.6. Instantaneous particle positions for passive tracer particles at  $t^+ =$  (a) 0, (b) 135, (c) 265 and (d) 675 for an initial release height of  $y_0^+ = 3$  (Case IV simulation). Particles are visualized in the  $y$ - $z$  plane and a  $x$  bin that is 150 wall units wide ( $h/4$  wide on either side of  $x = L_x/2$ ).

Starting from an initially uniform distribution (figure 4.5a), the early time particle distribution evolves showing patterns characteristic of flow structures present in a turbulent boundary layer (figures 4.5b-c). The late time particle distribution exhibits particle accumulation near the streamwise-elongated streaks (figure 4.5d). The motion of advecting streamwise vortices near the streamwise-elongated streaks is largely responsible for bringing particles closer to the low-velocity streaks. Figures 4.6(a-d) exhibit particle locations for passive tracers in a  $y$ - $z$  plane and an  $x$  bin of width 150 wall units (centered about  $x = L_x/2$ ). Particles are released in the viscous sublayer ( $y_0^+ = 3$ ) at

$t^+ = 0$ , as shown in figure 4.6(a). At early times (figures 4.6b-c), the particles released near the wall are thrown into the duct interior (lifted up away from the walls) by near-wall ejection events. At a later time ( $t^+ = 675$  in figure 4.6d), the passive tracer particles are distributed in the entire domain with some accumulation observed close to the walls.

## 4.2. One- and two-particle Lagrangian dispersion

A topic of immense practical and fundamental importance in fluid mechanics is the dispersion of particles by turbulence. Particles in turbulent flows are observed to quickly disperse from their initial location of release (Taylor 1921) and also from their original neighboring particles (Richardson 1926). Richardson (1926) proposed his empirical  $t^3$  law of Lagrangian particle pair dispersion. Later, significant theoretical contributions were made by Obukhov (1941) and Batchelor (1950 & 1952) who obtained power laws for the growth of inter-particle separation using Kolmogorov's (1941) similarity theory. The  $t^3$  law of particle pair dispersion predicts that the square of inter-particle separation will grow as  $t^3$  in the inertial sub-range. Despite its underlying assumptions about flow homogeneity and isotropy and the fact that a well-defined inertial sub-range at low and moderate Reynolds numbers is sometimes difficult to obtain, the Richardson prediction has been demonstrated in some real flows both computationally and experimentally (Babiano *et al.* 1990; Jullien *et al.* 1999). In this thesis, we present computational results related to one- and two-particle dispersion for the case of low Reynolds number turbulent flow in a straight square duct.

We shall use the notation,  $\Delta_{1-0}$ , to denote the one-particle statistics (e.g. displacement from the point of its initial release) and  $\Delta_{1-2}$  for the two-particle statistics (e.g. separation between two particles in a pair):

$$\langle \Delta_{1-0} \mathbf{X}_p(t) \rangle = \langle | \mathbf{X}_p(t)^{(1)} - \mathbf{X}_p(t=0)^{(1)} | \rangle \quad (4.1)$$

$$\langle \Delta_{1-2} \mathbf{X}_p(t) \rangle = \langle | \mathbf{X}_p(t)^{(1)} - \mathbf{X}_p(t)^{(2)} | \rangle \quad (4.2)$$

$$\langle \Delta_{1-2} \mathbf{U}_p(t) \rangle = \langle | \mathbf{U}_p(t)^{(1)} - \mathbf{U}_p(t)^{(2)} | \rangle \quad (4.3)$$



Their higher moments are denoted similarly. Angle brackets denote ensemble averages and the superscripts in brackets denote particle number (e.g. particles 1 and 2 that will form a pair). We will use  $r_0^+ \equiv \Delta_{1,2}x_p(0)$  to denote the initial inter-particle separation, which is specified only along the  $x$ -direction at the beginning of a simulation.

#### 4.2.1 Case I simulations

We have tracked a large ensemble of particles after releasing them with an initially uniform distribution on a plane at the duct inlet ( $x = 0$ ). We shall refer to the simulation corresponding to this initial condition as Case I. In this simulation, 25600 particles were released for sixteen different particle response times. The values of dimensionless particle response time, density ratio, and dimensionless particle radius for Case I are listed in table 4.1. The choice of a larger density ratio for the moderate and high inertia particles ensured that the dimensionless particle diameters were small compared to the estimated Kolmogorov length scale for this flow. All statistics were recorded at every time step ( $\Delta t$ ) for a total of 3.75 non-dimensional time units or, equivalently, 1125 time wall units. It is possible that the trajectories of particles with longer response times (e.g.  $\tau_p^+ > 100$ ) may remain somewhat influenced by the initial conditions. For the other particle response times, this time duration is expected to be sufficiently long to be free from the influence of initial conditions. Note that while table 4.1 lists all the parameters for simulation of Case I, not all will be discussed here. An interested reader may obtain the results for parameters listed in table 4.1 from the author.

We shall first examine the  $x$ -displacement of particles as a function of their inertia. As the particles move away from their initial release location at the duct inlet, some of the finite-inertia particles deposit at the duct walls, while others continue to diffuse under the influence of turbulence. Figure 4.7 displays the particle penetration, defined as the fraction of particles reaching a given distance from the initial release plane, as a function of downstream distance and particle inertia. The penetration of passive tracers (which do not deposit on the walls) remains very large ( $\geq 99\%$ ) for streamwise distances up to about 20 hydraulic diameters. It begins to drop appreciably after about 50 hydraulic diameters

due to increased near-wall accumulation that prevents the particles from reaching that distance within the simulation time. A notable feature of figure 4.7 is the transition in the shape of the curves from convex to concave for increasing particle inertia. The transition occurs somewhere between  $\tau_p^+ = 10$  (convex) and  $\tau_p^+ = 15$  (concave). This behavior is caused by the more frequent deposition of higher inertia particles, which results in an earlier drop in the penetration. We note, however, that the penetration appears to initially decrease less rapidly for the highest inertia particles (approaching  $\tau_p^+ = 300$ ). This is due to the difficulty in transporting these particles to the walls of the duct, and may be influenced by the initial conditions. As the majority approaches the duct walls, the penetration decreases sharply to zero.

---

$\tau_p^+$	$\rho$	$a^+$	$t_i^+$	$N_p$
0	-	-	1125	25600
3	763	0.1330	1125	25600
5	763	0.1717	1125	25600
8	763	0.2172	1125	25600
10	763	0.2429	1125	25600
15	763	0.2974	1125	25600
20	763	0.3434	1125	25600
25	2083	0.2324	1125	25600
30	2083	0.2546	1125	25600
40	2083	0.2940	1125	25600
50	2083	0.3287	1125	25600
75	7333	0.2145	1125	25600
100	7333	0.2477	1125	25600
150	7333	0.3034	1125	25600
300	7333	0.4291	1125	25600

---

Table 4.1. Particle transport simulation parameters for Case I.  $a_p^+$  refers to the dimensionless particle radius.

---

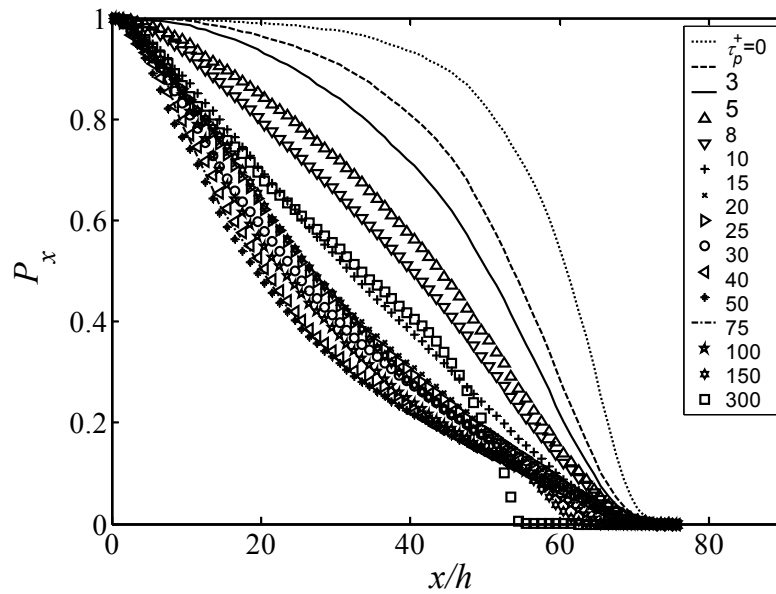


Figure 4.7. Particle penetration measured in streamwise bins of length  $h$  through the square duct.

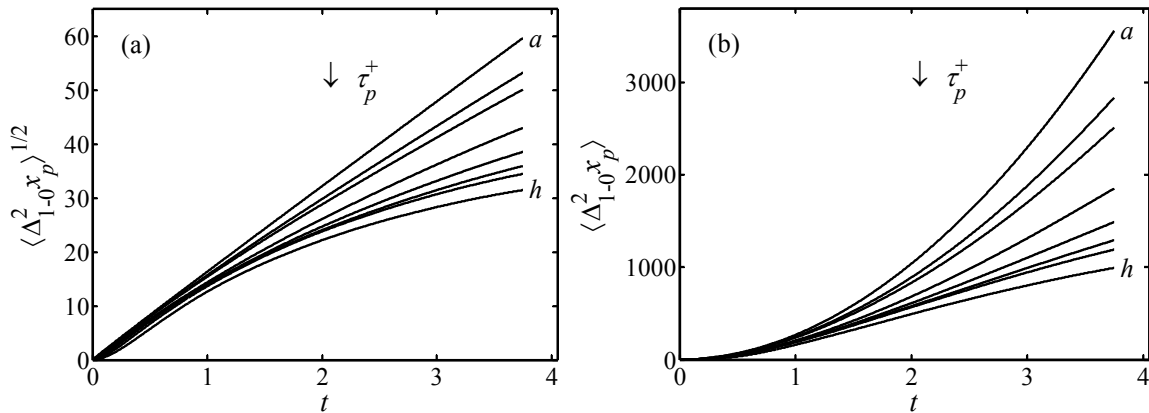


Figure 4.8. Growth of (a) RMS displacement and (b) mean square displacement (MSD). Particle response times are  $\tau_p^+ = (0, 3, 5, 10, 15, 20, 30$  and  $50)$  for curves  $(a - h)$ .

The Case I simulations were also used to compute turbulent diffusion coefficients of particles in the straight square duct flow. An estimate of the turbulent particle diffusivity is obtained using the ensemble-averaged square of displacement (or mean square displacement, MSD). The time varying turbulent diffusion coefficients for the homogeneous streamwise direction,  $\varepsilon_{xp}$ , can be estimated from the relation

$$\varepsilon_{xp} = \frac{1}{2} \frac{d\langle \Delta_{1-0}^2 x_p \rangle}{dt} \quad (4.4)$$

where the angle brackets denote an ensemble-average over 25600 particles. The diffusion coefficients were computed by approximating the time derivative in (4.4) using a standard second-order accurate central difference. We note that the present computation of the ensemble-averaged growth of particle displacement,  $\langle \Delta_{1-0} \mathbf{X}_p \rangle$ , (and its higher moments) considers the contribution from the deposited particles as well. Figure 4.8(a) shows the ensemble-averaged RMS displacement ( $\langle \Delta_{1-0}^2 x_p \rangle^{1/2}$ ) for selected particle response times from Case I. The RMS displacement drops with increasing particle inertia, while, for passive tracers it maintains a near constant slope approximately equal to the bulk fluid velocity (Monin & Yaglom 1971):

$$\langle \Delta_{1-0}^2 x_p \rangle^{1/2} \approx u_b t. \quad (4.5)$$

The small deviation from the bulk fluid velocity is due to the accumulation in the near-wall regions. Figure 4.8(b) shows the ensemble-averaged square of particle displacement ( $\langle \Delta_{1-0}^2 x_p \rangle$  or MSD) as a function of selected particle response times. Figure 4.9 shows the particle diffusion coefficients from the numerically estimated time derivative of the MSD. The particle diffusivity decreases with increasing particle response time. For passive tracers it is almost linear in time with a near constant slope. The slope is approximately constant for other particle response times as well, but over a shorter duration. A time-mean turbulent particle diffusivity in the  $x$ -direction,  $\varepsilon_{xp}^a$ , can be estimated from the ensemble-averaged, time varying turbulent particle diffusivity (shown in figure 4.9) by averaging over a fixed length of time  $t$ . The time-mean particle diffusivity averaged over the initial one non-dimensional time unit is nearly constant for all particle response times considered here. For averages over later times,  $\varepsilon_{xp}^a$  exhibits considerable variation among different particle response times, which follows from the observed saturation (even drop) in case of the longer particle response times shown in figure 4.9. The diffusivity plot exhibits a drop at later times for particles with  $\tau_p^+ > 10$ .

This is consistent with the evidence from figure 4.7 that there exists a transition beyond which particle inertia begins to dominate the transport properties, and that this transition occurs between  $\tau_p^+ = 10$  and 15. This transition closely resembles that noted by Young & Leeming (1997), who identify a *diffusion-impaction* regime between  $0.2 < \tau_p^+ < 20$  and an *inertia-moderated* regime beyond  $\tau_p^+ = 20$ .

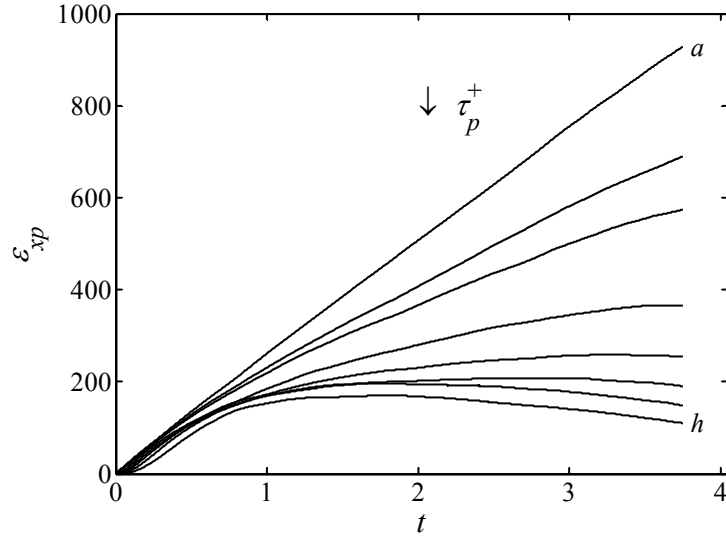


Figure 4.9. Time variation of the turbulent particle diffusivity. Particle response times are  $\tau_p^+ = (0, 3, 5, 10, 15, 20, 30 \text{ and } 50)$  for curves (a – h).

#### 4.2.2 Case II simulations

Case II refers to the numerical computation of Lagrangian particle pair dispersion, in which 24892 particle pairs ( $\tau_p^+ = 0, 5, 15$  and 30) were released in the core region ( $y^+ \geq 100$ ) of the turbulent straight square duct. Particles were arranged on a three-dimensional grid of size  $128 \times 14 \times 14$ , corresponding to 25088 particles or 24892 particle pairs (127 particle pairs per line). The  $x$ -length of this grid was different for each prescribed initial particle separation,  $r_0^+$ , since the number of particles was intended to be constant in different  $r_0^+$  simulations. The particle parameters for Case II are listed in table 4.2. Again, we note that the computations of the growth of ensemble-averaged inter-particle

separation,  $\langle \Delta_{1,2} X_p(t) \rangle$ , (and its higher moments) include the contribution from deposited particles. This contribution is very small for low inertia particles, which deposit much less frequently. Particle pairs were only released in the outer layer where turbulence is relatively homogeneous and isotropic, compared to near the walls. Nevertheless, some deviation from theoretical predictions may result from flow inhomogeneities and anisotropy, finite-inertia effects, and particle deposition. These realistic situations have been considered for the discussions presented in this thesis.

Particle pairs were tracked for a total of 6.0 non-dimensional time units or, equivalently, 1800 time wall units, and statistics were recorded at every time step. The time range in which the Richardson regime is expected is a strong function of the initial inter-particle separation (see discussion in Sawford 2001). The present time duration of 6.0 non-dimensional time units is more than adequate to allow the observation of any possible power law regime(s).

---

$\tau_p^+$	$\rho$	$a^+$	$t_i^+$	$N_{pairs}$	$N_p$
0	-	-	1800	24892	25088
5	763	0.1717	1800	24892	25088
15	763	0.2974	1800	24892	25088
30	763	0.4206	1800	24892	25088

---

$$r_0^+ = 0.5, 2.0, 8.0, 10.0, 12.0, 16.0, 20.0 \text{ and } 24.0.$$

Table 4.2. Particle transport simulation parameters for Case II.

---

Figures 4.10-4.12 show the time variation of the square of inter-particle separation for four different particle response times and six different initial inter-particle separations. The selected initial inter-particle separations of  $r_0^+ = 0.5, 2, 8, 12, 16$  and  $24$  correspond to  $r_0^+/\eta$  values of approximately  $1/4, 1, 4, 6, 8$  and  $12$ , respectively, using the Kolmogorov length scale estimated for this flow by Gavrilakis (1992). In reality, the Kolmogorov

length scale varies with spatial location. A more accurate estimate of the value of  $\eta$  would require direct computation of the dissipation functions without the assumption of isotropy (as in Deshpande & Milton 1998). Three different slope lines are shown detached in figures 4.10-4.12 to aid in the visualization of observed short-time power law behavior from the plots. We refer to these lines as the first, second or third slope lines, according to the time-order of their appearance. Power law behavior is observed over certain durations for all  $r_0^+$  values considered here. The exponent  $n$  in the observed  $t^n$  regimes is a strong function of  $r_0^+$ . The square of initial inter-particle separation is expected to grow as  $t^2$  just after the initial release of particle pairs. All of the plots exhibit an early  $t^2$  regime, as indicated by the first slope lines, with the constant relating  $\langle \Delta_{1-2}^2 x_p(t) \rangle - \Delta_{1-2}^2 x_p(0)$  to  $t^2$  approaching unity with increasing  $r_0^+/\eta$ . In addition to the early  $t^2$  regime predicted by Batchelor (1950), we also observe an intermediate-time power law regime, which is clearly different from the  $t^3$  regime (also predicted by Batchelor 1950) and is highlighted here by the second slope lines. The value of the exponent drops from about 7.0 for  $r_0^+/\eta \sim 1/4$  to about 3.9 for  $r_0^+/\eta \sim 12$ . Finally, the third slope line refers to a third distinct power law, which appears to correspond to the  $t^3$  regime, with the exception of the smallest initial separation ( $r_0^+/\eta \sim 1/4$ ), which exhibits  $t^4$  behavior. It is interesting that, even for the present inhomogeneous turbulent flow, a  $t^3$  relative dispersion can be obtained for certain values of  $r_0^+$  that are not significantly smaller than the Kolmogorov length scale. The effect of particle inertia becomes evident only after the  $t^2$  regime, as the inter-particle separation grows faster for higher inertia values.

Figures 4.13(a-b) show the time variation of the RMS streamwise velocity difference ( $\langle \Delta_{1-2}^2 u_p \rangle^{1/2}$ ) for initial inter-particle separations of  $r_0^+/\eta \sim 1$  and 12. The growth appears linear at early times (between approximately  $t = 0.25$  and  $t = 1.25$ ) and subsequently levels off to a near constant value, except for the higher inertia particles for which it begins to drop due to deposition.

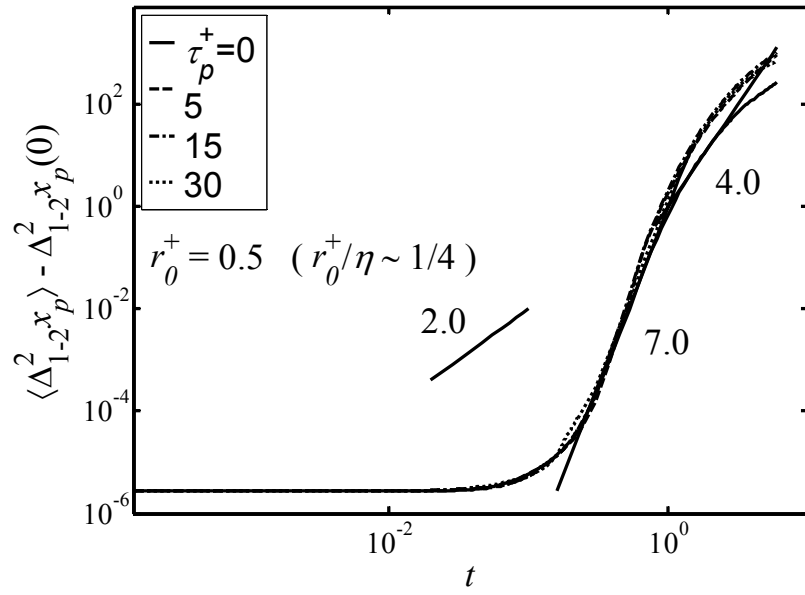


Figure 4.10. Time variation of the square of inter-particle separation for  $r_0^+ = 0.5$ .

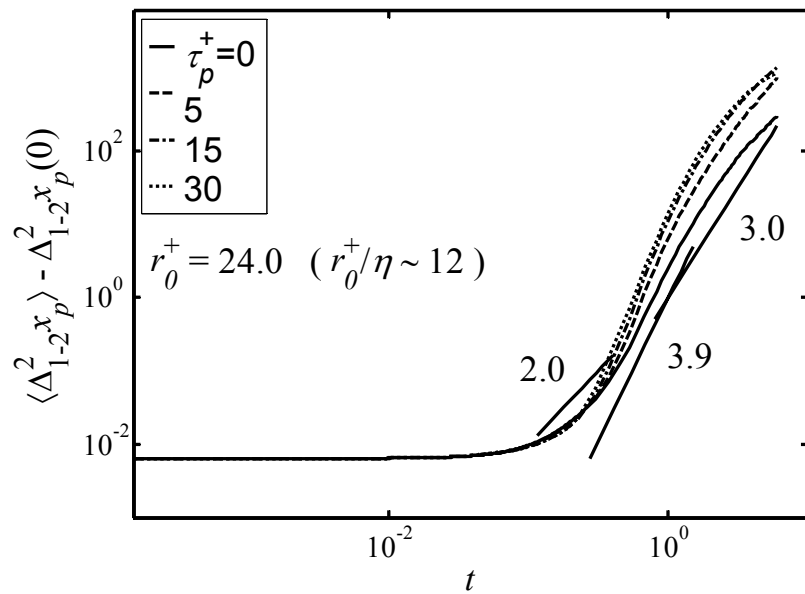


Figure 4.11. Time variation of the square of inter-particle separation for  $r_0^+ = 24.0$ .



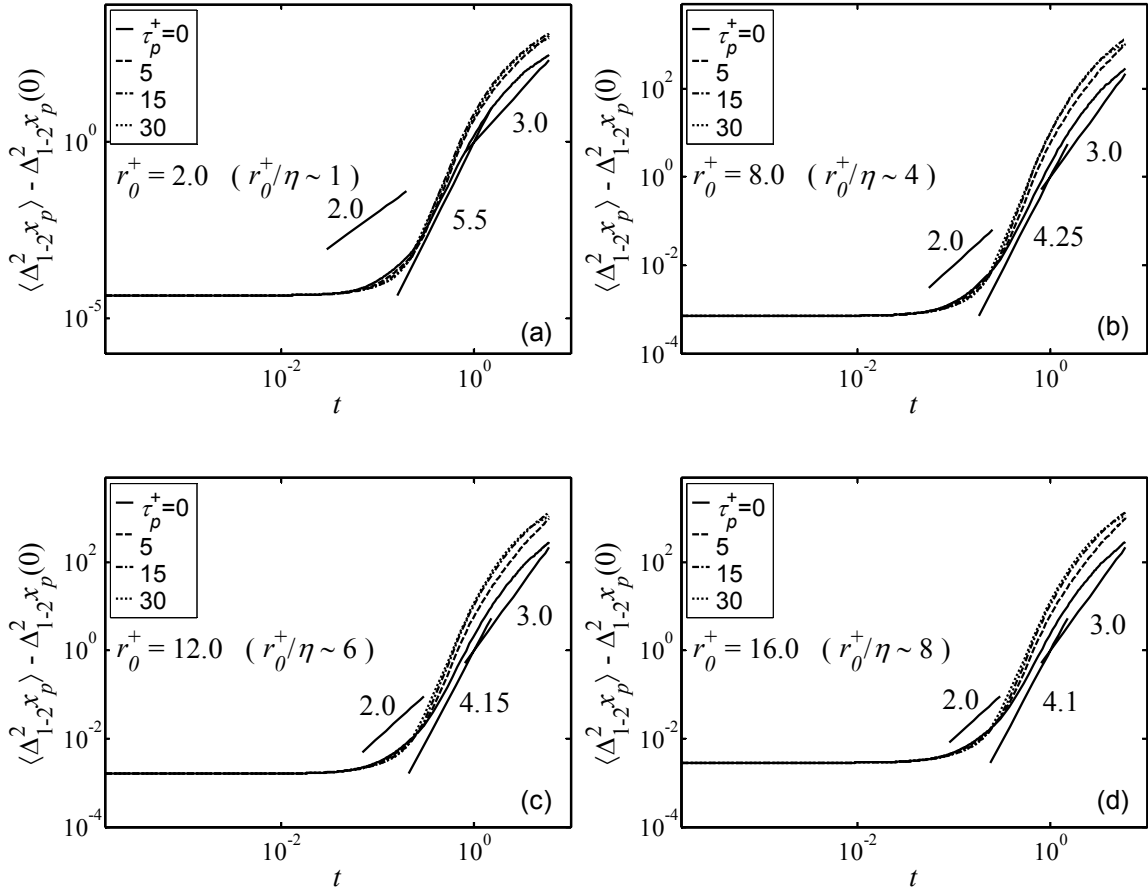


Figure 4.12. Time variation of the square of inter-particle separation for (a)  $r_0^+ = 2.0$ , (b)  $r_0^+ = 8.0$ , (c)  $r_0^+ = 12.0$  and (d)  $r_0^+ = 16.0$ .

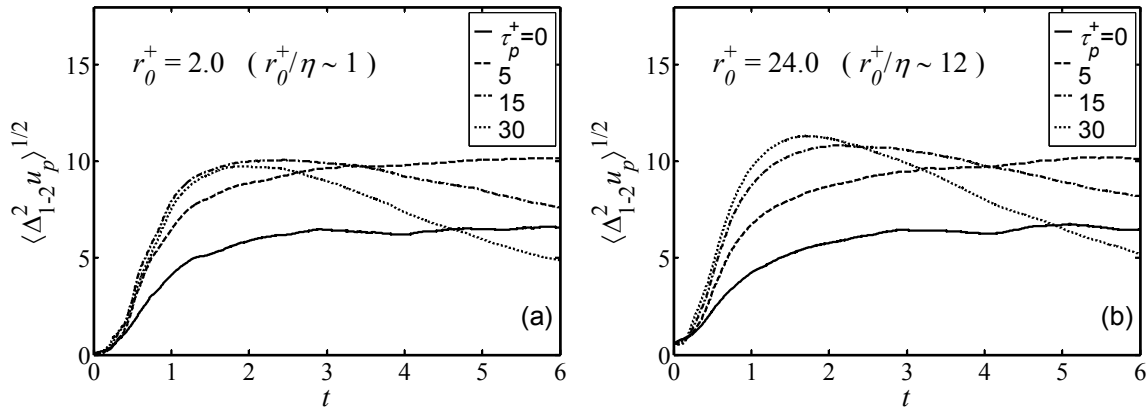


Figure 4.13. Time variation of the RMS inter-particle velocity difference for (a)  $r_0^+ = 2.0$  and (b)  $r_0^+ = 24.0$ .

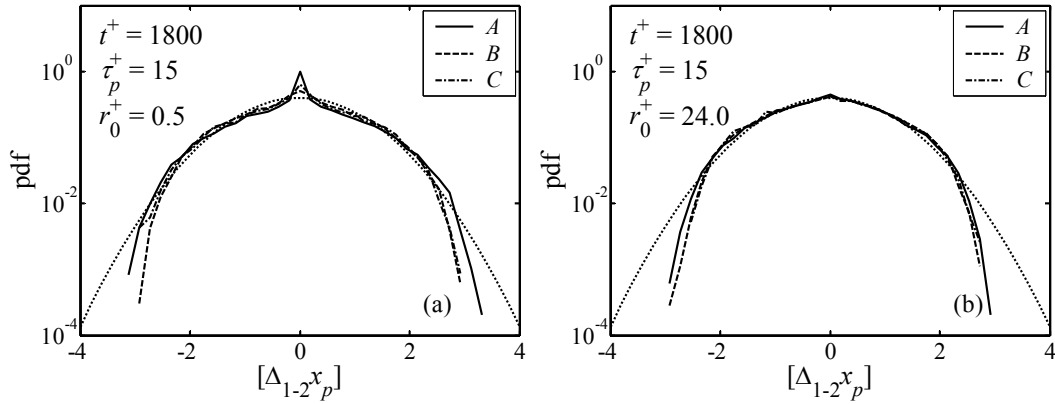


Figure 4.14. pdfs of the  $x$ -direction standardized inter-particle separations at a late time of the simulation ( $t^+ = 1800$ ) for  $\tau_p^+ = 15$  and (a)  $r_0^+ = 2.0$  and (b)  $r_0^+ = 24.0$ . The dotted line represents the standard Gaussian.

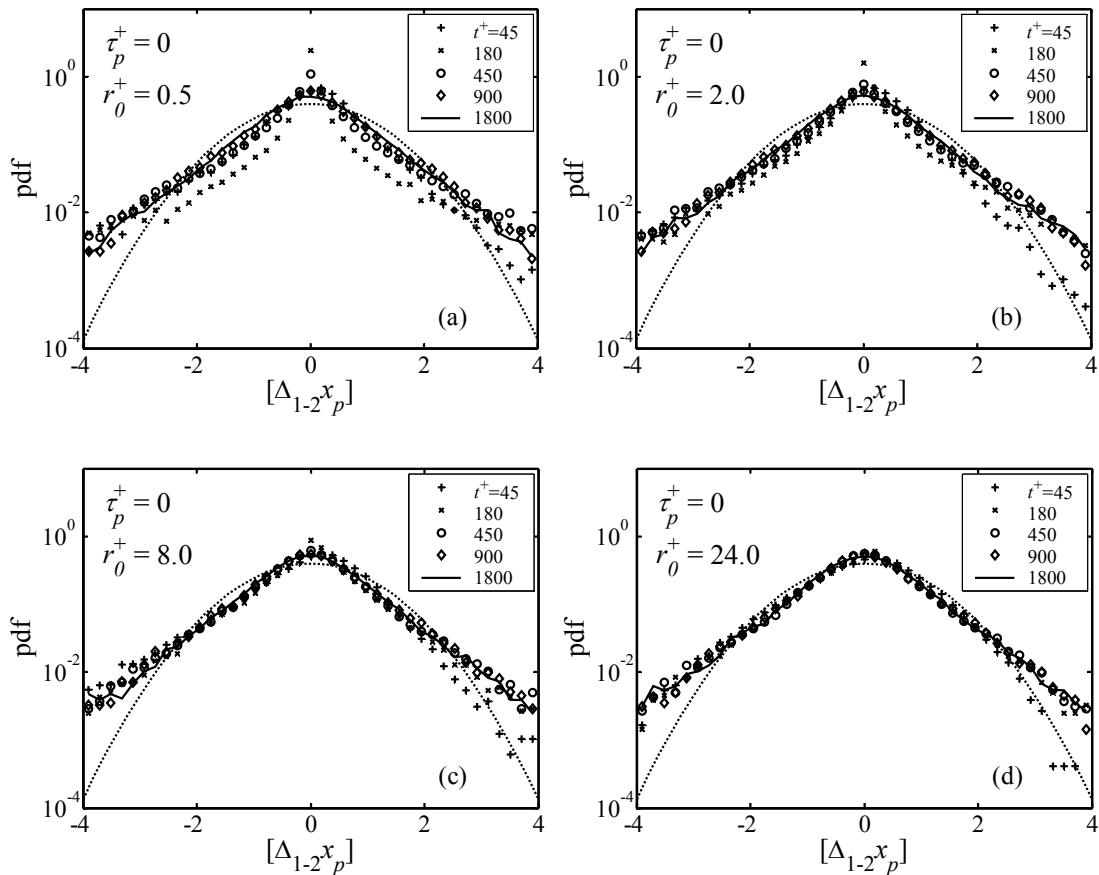


Figure 4.15. pdfs of the  $x$ -direction standardized inter-particle separations at five different times of the simulation for passive tracer particles and four different initial inter-particle separations. The dotted line represents the standard Gaussian.

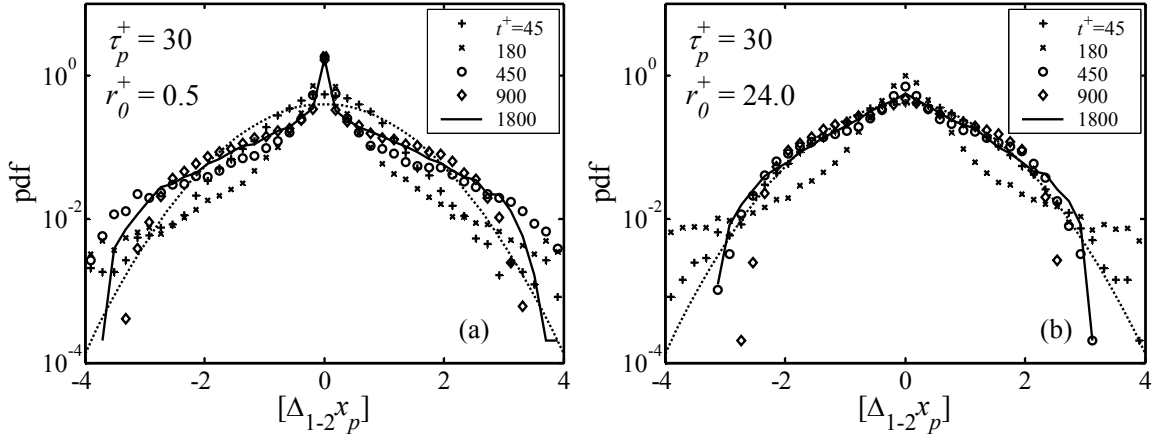


Figure 4.16. pdfs of the  $x$ -direction standardized inter-particle separations at five different times of the simulation for  $\tau_p^+ = 30$  particles and four different initial inter-particle separations. The dotted line represents the standard Gaussian.

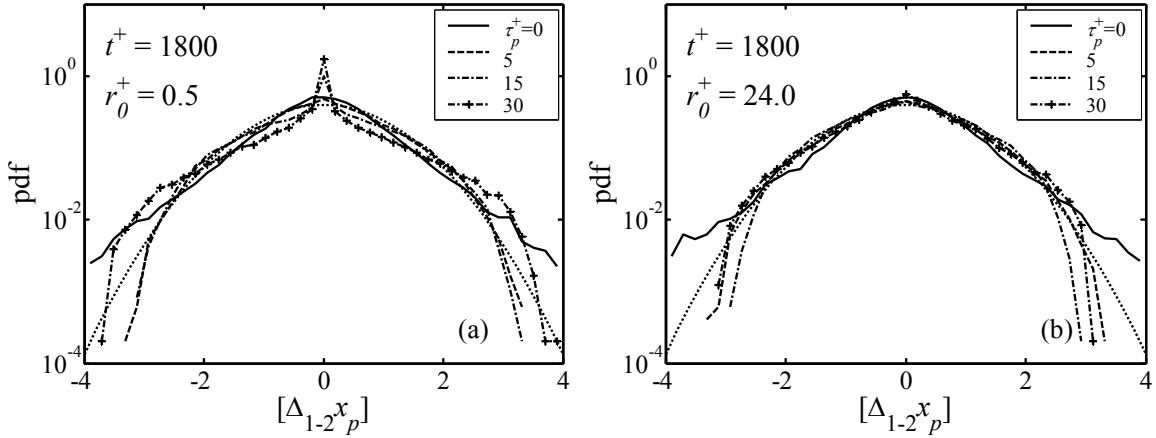


Figure 4.17. pdfs of the  $x$ -direction standardized inter-particle separations at the end of Case II simulation ( $t^+ = 1800$ ) for four different particle response times and for (a)  $r_0^+ = 0.5$  and (b)  $r_0^+ = 24.0$ . The dotted line represents the standard Gaussian.

The distribution of inter-particle separation in the ensemble was uniform at the beginning of simulation ( $t^+ = 0$ ). It is interesting to see the time variation of this initially uniform inter-particle separation. Figures 4.14-4.17 show the probability distribution function (pdf) for the standardized inter-particle separation in the ensemble. For the purpose of computing pdf's, standardization of any variable  $q$  is carried out by the transformation,  $[q] = (q - \mu_q)/\sigma_q$ , where  $\mu_q$  and  $\sigma_q$  are the mean and standard deviation

respectively, of  $q$ . Variables standardized for pdf have a zero mean and unit variance, and are denoted here with square brackets. This simple transformation is shape preserving and allows convenient comparison with the standard Gaussian, which also has a zero mean and unit variance. We view the pdfs in 41 bins in the  $[q]$  range of  $[-4, 4]$  only i.e. rare events in  $[q]$  with standard deviation more than  $\pm 4$  will not be considered here.

We intend to compute the pdf's by taking into account the deposited particles and particle pairs in the ensemble. Before doing so we would like to see the effect of deposition of a particle or a pair on the statistics of inter-particle separations. We therefore compute and plot in figure 4.14 the  $x$ -direction inter-particle separation pdfs for three different types of particle pair ensembles. In one case (type A ensemble), the separation from all the particle pairs was considered in the ensemble. In another case (type B ensemble), only the pairs having at least one un-deposited particle were considered in the ensemble. In still another case (type C ensemble), only those pairs that have both particles as un-deposited were considered. There is a clear difference in the pdfs of inter-particle separation from these cases. This difference is expected to be larger for higher inertia particles like  $\tau_p^+ = 15$  or  $30$  which deposit in large numbers. The pdfs in figure 4.14 are shown for a late time ( $t^+ = 1800$ ) since more particles would have deposited by that time and the difference in statistics of type A, B and C ensemble would be more pronounced. The type A ensemble exhibits a longer tail to the right side of the mean, while type B exhibits one towards the left. Type A has higher peak at the mean than the corresponding Gaussian or other ensemble types. For type C, the tails are shorter and the curves are flatter at the mean. The peak near the mean in the type A ensemble is smaller for  $r_0^+ = 24$  (figure 4.14a) than for  $r_0^+ = 0.5$  (figure 4.14b) i.e. the peak decreases as  $r_0^+/\eta$  increases. The main difference between type A, B and C is the length of the tails. Also with increasing initial inter-particle separations, the distributions are closer to Gaussian at late times when the deposited individual particles (type B) or pairs (type C) are not considered in the ensemble. We shall interpret the data from type A ensembles only, as it more realistically represents the events occurring in this flow.

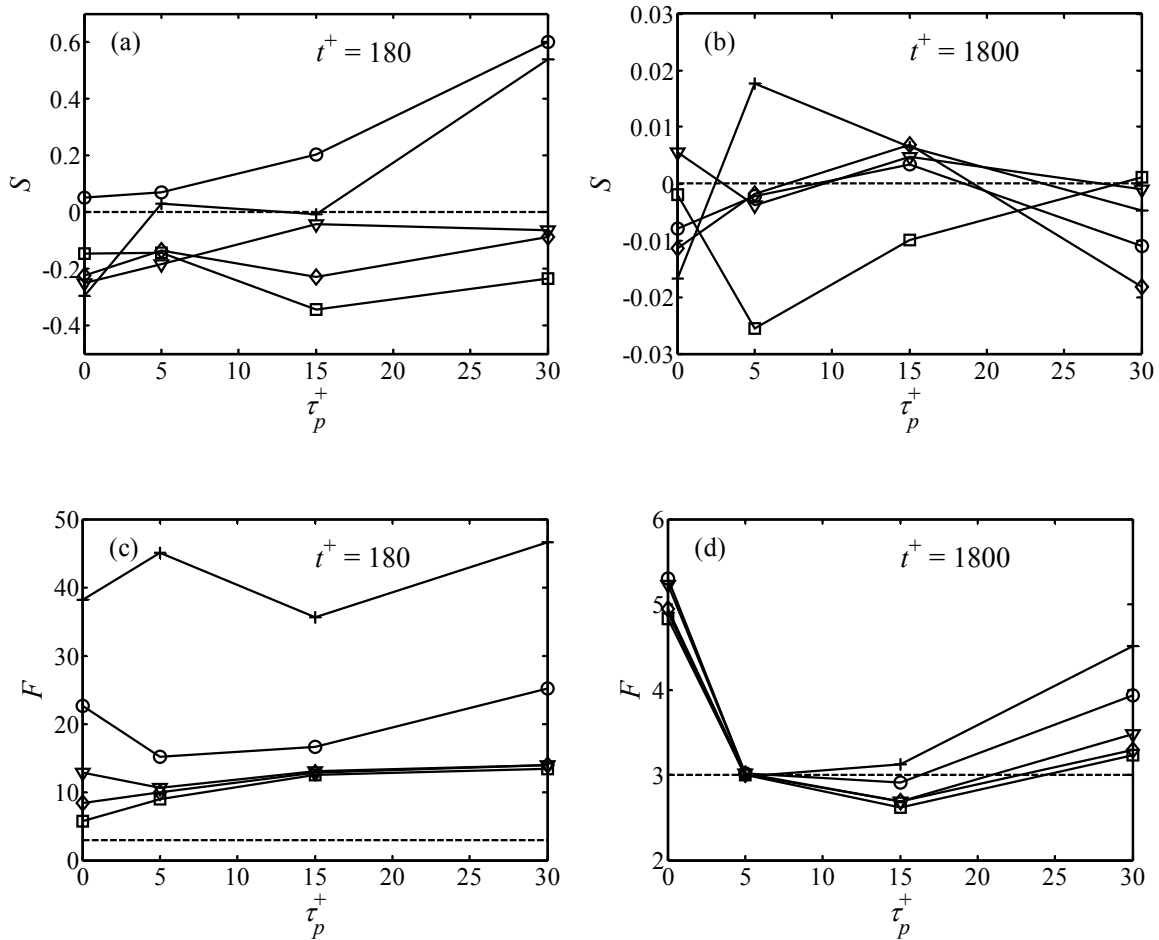


Figure 4.18. Skewness and flatness factors in the  $x$ -direction inter-particle separations at two different times of the simulation. The dashed line represents a Gaussian distribution.

The distributions are strongly non-Gaussian at  $t^+ = 180$ , as shown in figures 4.15-4.16, and subsequently approach Gaussian towards the end of the simulation ( $t^+ = 1800$ ). Higher inertia particles and larger initial inter-particle separations exhibit more Gaussian behavior. The strong non-Gaussian behavior before  $t^+ = 300$  likely represents a power law regime, when most values of inter-particle separation are similar to each other, resulting in a sharp peak in the pdf plot. At late times, when particle pair separations begin to grow in an uncorrelated fashion, the distributions become more Gaussian with longer tails for passive tracers and with some asymmetry with increasing values of  $r_0^+/\eta$  (figures 4.17a-b). To further test for the deviation from Gaussian behavior, we computed the skewness and flatness factors (figures 4.18a-d) for the inter-particle separation distributions at two

different times of the simulation. The deviation of the skewness and flatness factors from a Gaussian distribution (shown by dashed lines in figures 4.18a-d) decreases with time. We have presented here selected results on the particle pair dispersion in a stationary frame of reference. Additional results from these computations (for parameters listed in table 4.2) may be obtained from the author.

### 4.3. Particle concentration and deposition statistics

The statistics of particle concentration and deposition were obtained from the Case III and Case IV numerical simulations.

#### 4.3.1 Case III simulations

In Case III, a large ensemble of randomly distributed particles was released in the domain. The initial particle distribution was generated using Gaussian random numbers in  $[0, 1]$  with the constraint that no particle was released very close to any of the four walls ( $y_s^+ = 10$ ). As listed in table 4.3, the particle response times chosen for this simulation were  $\tau_p^+ = 0, 1, 5, 10, 15, 20, 30$  and  $50$ . For each  $\tau_p^+$  value, 64000 particles were tracked for a total 675 time wall units. To minimize the influence of initial conditions, the time-averaged statistical results were obtained during the last 600 time wall units of simulation. Therefore,  $t_t^+ = 675$  denotes total time of particle tracking while  $t_s^+ = 600$  denotes time of statistics (for concentration, deposition etc.).

The particle number concentration was measured in 150 bins in the wall-normal directions, each having a width of  $\Delta y_b^+ = \Delta z_b^+ = 1.00$  and 170 bins in the streamwise direction with a width of  $\Delta x_b^+ = 22.17$ . The wall-normal bins extended from the wall to the duct centerline, providing a total of 600 bins throughout the cross-section (150 bins away from each of four walls to duct center). The computed data in the wall-normal bins were quadrant-averaged from all four walls (4 x 150 bins). Particle number concentration in each bin has been normalized by the average concentration in one corresponding bin at  $t^+ = 0$ . Concentration data were collected every ten time steps.

$\tau_p^+$	$\rho$	$a^+$	$t_i^+$	$t_s^+$	$N_p$
0	-	-	675	600	64000
5	763	0.1717	675	600	64000
10	763	0.2429	675	600	64000
15	763	0.2974	675	600	64000
20	763	0.3434	675	600	64000
30	763	0.4206	675	600	64000
50	763	0.5430	675	600	64000

Table 4.3. Particle transport simulation parameters for Case III.

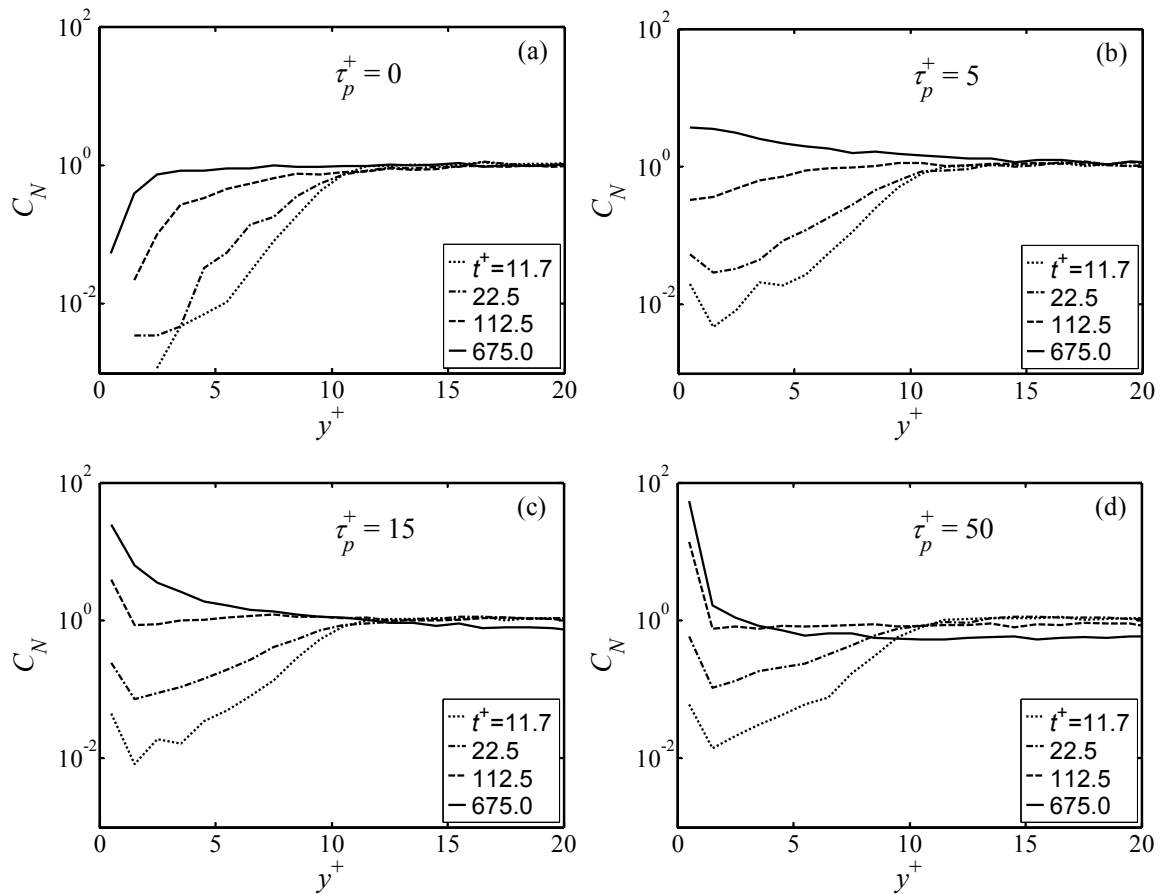


Figure 4.19. Normalized instantaneous particle number concentration near the wall for initially random distribution of particles (Case III simulation).

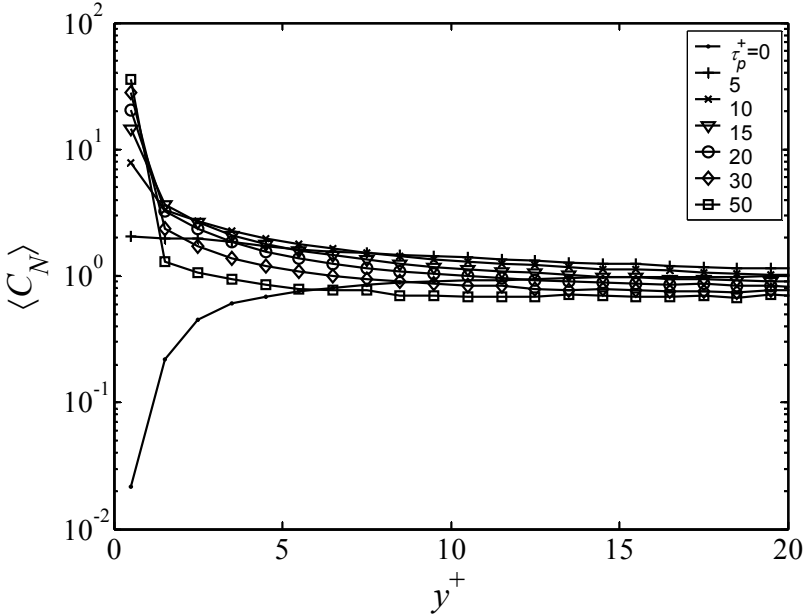


Figure 4.20. Normalized time-averaged particle number concentration near the wall for different inertia values in Case III simulation.

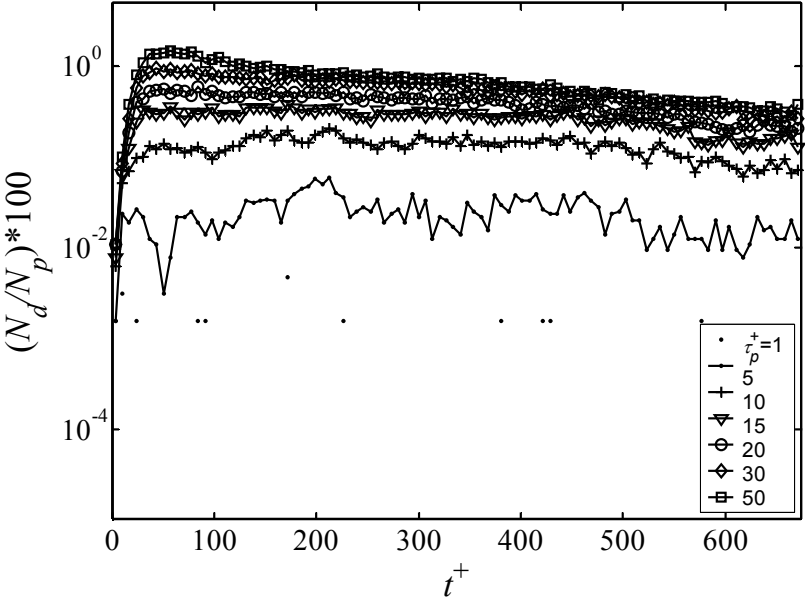


Figure 4.21. Particle deposition rate normalized by the number of particles at time  $t^+ = 0$ .



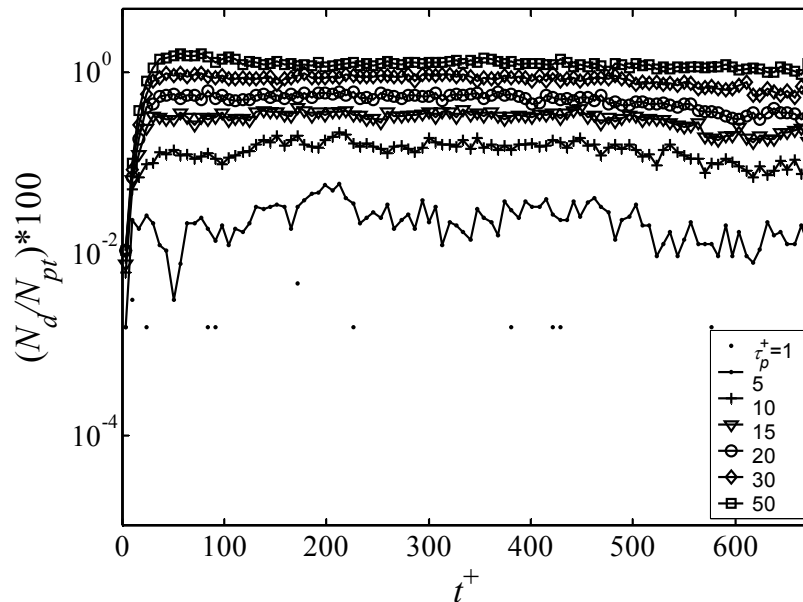


Figure 4.22. Particle deposition rate normalized by time-local number of particles in time bins.

Figures 4.19(a-d) show the instantaneous number concentration profile near the wall ( $y$  and  $z$  quadrant-averaged) at four different times during the simulation, where all concentrations were normalized with the initial number concentration. The concentration near the walls increases more rapidly for the longer particle response times, whereas particle accumulation in the viscous sublayer is lower for passive tracers. This is especially evident from figure 4.20, which displays the near-wall concentration profiles averaged over the time of statistics ( $t_s^+ = 600$ ) for all of the particle response times considered. The near-wall particle number concentration increases monotonically with particle response time, a direct result of inertia-driven deposition to the walls. The low near-wall concentration of the passive tracers is due to the fact that they do not deposit and hence are not counted in large numbers in the first bin away from the wall. The near-wall concentration of passive tracers would continue to build up further in a longer simulation.

The rate of deposition is shown in figures 4.21 and 4.22. Figure 4.21 shows the number of deposited particles per time bin normalized by the number of particles at the beginning of simulation ( $N_p$ ). Figure 4.22 plots the number of deposited particles per time bin

normalized by the number of un-deposited particles from the previous time bin ( $N_{pt}$ ). The deposition is measured in 100 time bins throughout the simulation with a time bin width of  $\Delta t_b^+ = 6.75$ . After the initial transient period caused by the effect of particle initial conditions, the deposition rate becomes nearly constant and increases with particle inertia.

#### 4.3.2 Case IV simulations

In Case IV, a large ensemble of particles distributed uniformly on planes at different heights above the walls was released at the beginning of the simulation. Eleven initial release plane heights ( $y_0^+$ ) were selected:  $y_0^+ = 3, 4, 10, 20, 30, 40, 50, 60, 75, 100$  and  $130$ . The  $y_0^+ = 3$  and  $4$  planes are located within the viscous sublayer, the  $y_0^+ = 10, 20, 30, 40$  and  $50$  planes are in the buffer region, and the  $y_0^+ = 60, 75, 100$  and  $130$  planes are in the outer region of the turbulent boundary layer. There was an additional lateral separation of  $y_s^+ = 20$  wall units between each of the four planes and the nearest sidewall. Each plane initially contained 10948 particles, thus every  $y_0^+$  plane refers to the release of 43792 particles, considering the contribution from all four walls. A total of 481712 particles were tracked for each particle response time considered. As listed in table 4.4, the particle response times chosen for Case IV were  $\tau_p^+ = 0, 5, 15$  and  $30$ . The particles were tracked for a total of 675 time wall units. The wall-normal and streamwise bins for concentration and the time bins for deposition are identical in size to those in the Case III simulation. However, for normalization we assume here a uniform concentration at  $\bar{t}^+ = 0$ .

---

$\tau_p^+$	$\rho$	$a^+$	$t_t^+$	$t_s^+$	$N_p$
0	-	-	675	600	481712
5	763	0.1717	675	600	481712
15	763	0.2974	675	600	481712
30	763	0.4206	675	600	481712

---

$y_0^+ = 3, 4, 10, 20, 30, 40, 50, 60, 75, 100$  and  $130$ .

Table 4.4. Particle transport simulation parameters for Case IV.

---

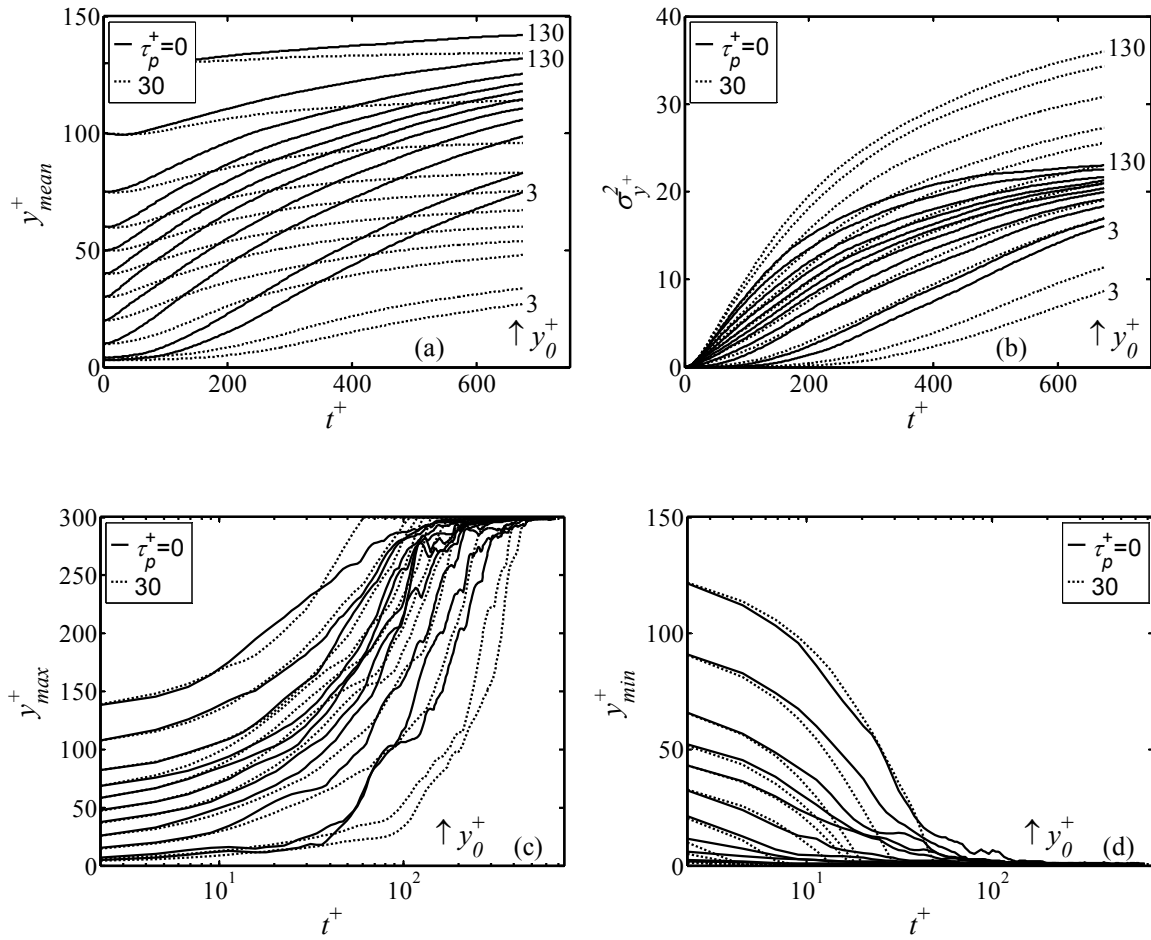


Figure 4.23. For particles released at different heights above the wall, time variation of (a) mean distance from the wall, (b) variance in the distribution, (c) maximum distance, and (d) minimum distance from the wall.

For each  $y_0^+$  plane, the growth of average, maximum and minimum distance of a particle from the wall is shown in figures 4.23(a), 4.23(c) and 4.23(d) respectively. Figure 4.23(b) shows the growth of the variance in the distribution of instantaneous particle locations for each of the  $y_0^+$  planes. Figures 4.24(a-f) display the normalized instantaneous number concentration profile at four times during the Case IV simulation, for three initial release heights, and for two different particle response times. Again, we see the higher inertia particles being driven to the wall, as indicated by the rapid rise of the concentration in bins near the wall. The near-wall concentration increases monotonically with the particle inertia values considered in this simulation. Another

notable feature of figure 4.24 is the increasingly more rapid broadening of the initially narrow profile as the initial release plane is moved further away from the wall. This is especially evident in figure 4.25, which displays a snapshot of the normalized number concentration profile for all eleven initial release heights for the case of passive tracers. Note that the concentration peaks are approximately equal for initial release heights located in the outer region of the turbulent boundary layer. The fluid in the core region of the duct disperses the particles more quickly when compared to the more quiescent regions of the turbulent boundary layer. The near-wall concentration increases monotonically with particle inertia values considered in this simulation. This can be seen clearly as a function of particle inertia at one instant of time from figure 4.26. The concentration starts to build up more quickly in bins near the wall for  $\tau_p^+ = 30$  particles than for passive tracers.

The time-averaged ( $t_s^+ = 600$ ) and normalized particle number concentration in the wall-normal ( $y$  and  $z$  averaged) direction is shown in figure 4.27 for four particle response times. As expected, the near-wall concentration is lowest for passive tracers and highest for  $\tau_p^+ = 30$  particles. Compared to the simulation of Case III, the concentration of all particle types exhibits smaller fluctuations in the interior of domain. This can be attributed in part to the significantly larger number of particles ( $N_p = 481712$ ) in the Case IV simulation when compared to the Case III simulation ( $N_p = 64000$ ). Similar to Case III, the near-wall concentration from Case IV increases monotonically with increasing inertia. Unlike Case III, however, the concentration exhibits a well-defined peak near  $y^+ = 3$  in the viscous sublayer for all particle response times. The peak becomes more of a shoulder for the  $\tau_p^+ = 15$  and 30 particles whose time-averaged concentration maximum is in the first bin away from the wall due to frequent deposition. The peak at  $y^+ = 3$  is due to particle accumulation over the duration of the simulation, whereas the peak at  $y^+ = 1$  is due to deposition.

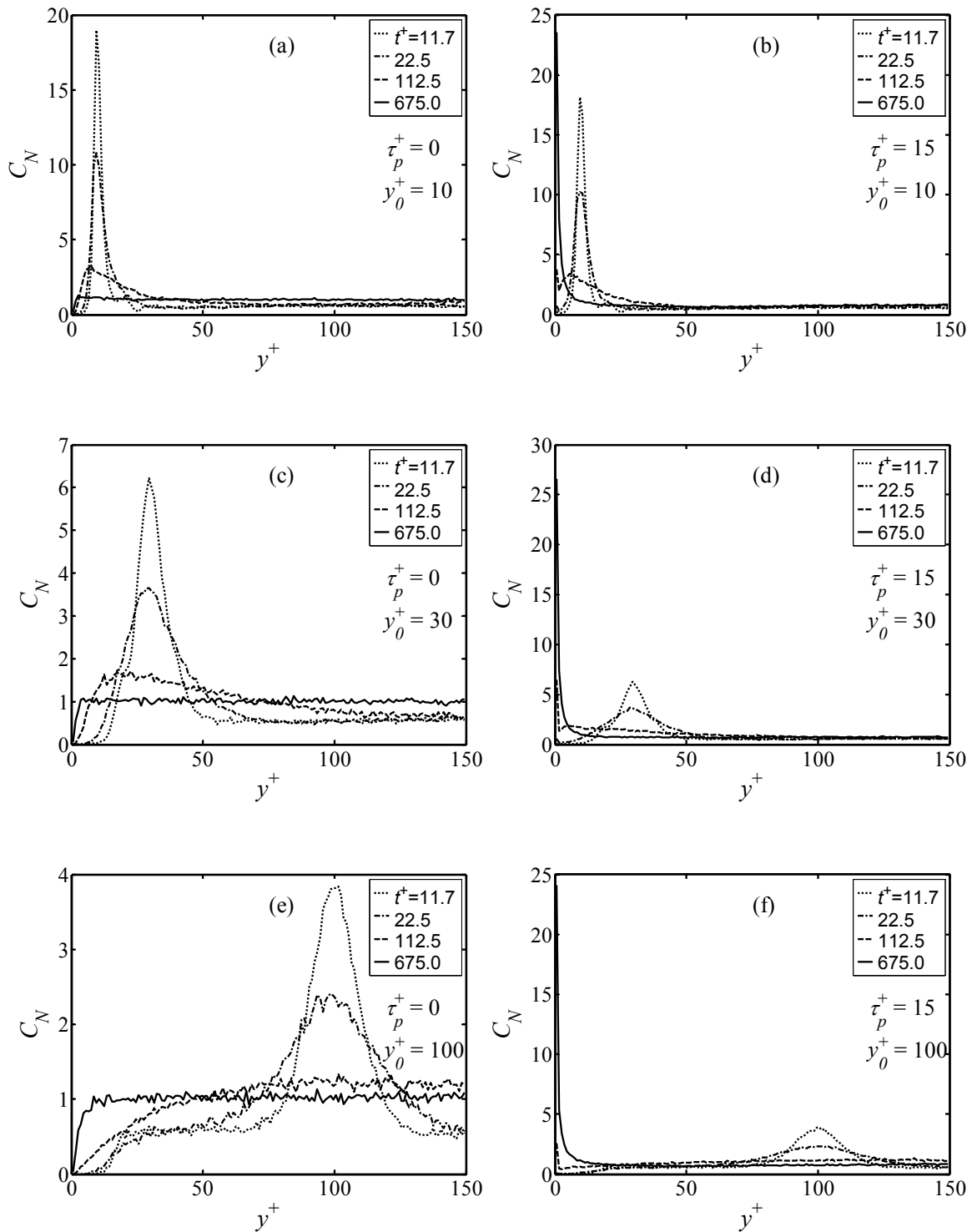


Figure 4.24. Normalized instantaneous particle number concentration for  $\tau_p^+ = 0$  (figures on the left) and  $\tau_p^+ = 15$  (figures on the right), for three different initial release heights.

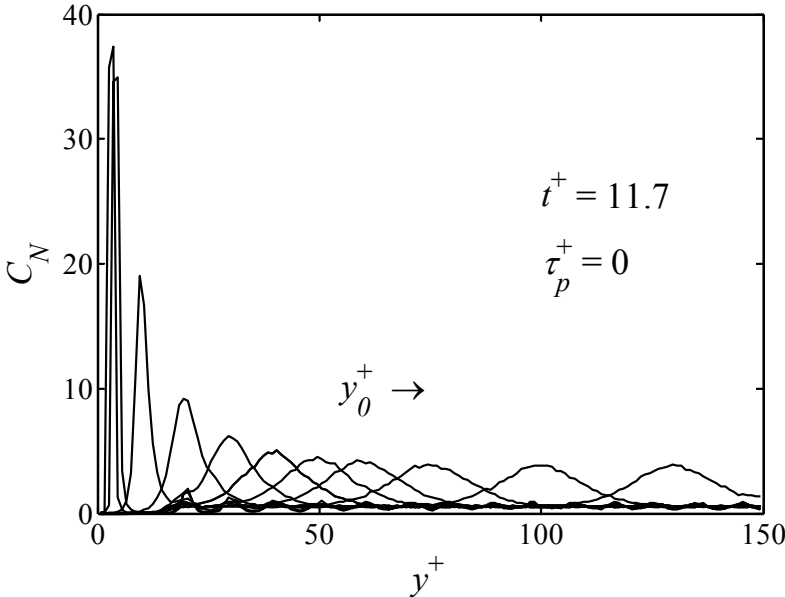


Figure 4.25. Normalized instantaneous particle number concentration for the passive tracer particles at an early time after their release from eleven different initial release heights above the duct walls.

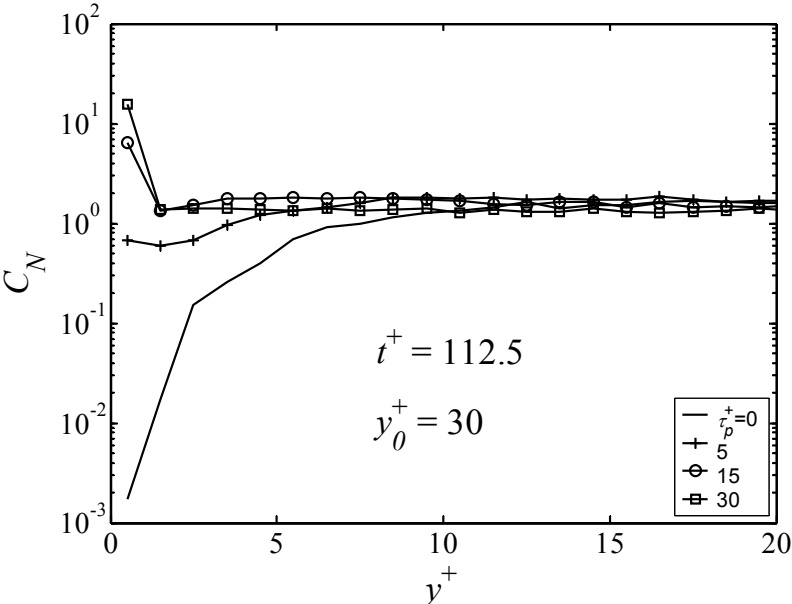


Figure 4.26. Normalized instantaneous particle number concentration for four different particle response times and one initial release height.

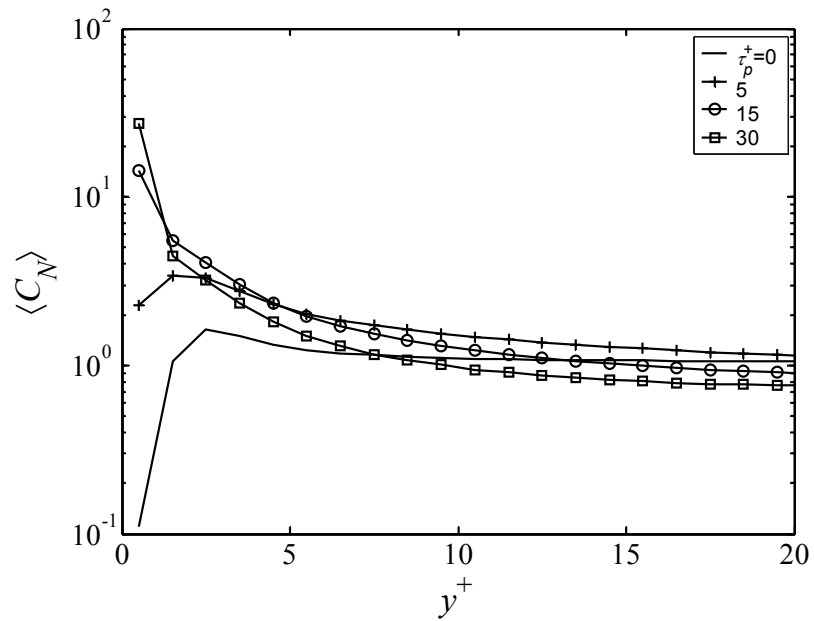


Figure 4.27. Normalized time-averaged particle number concentration near the wall in Case IV simulation.

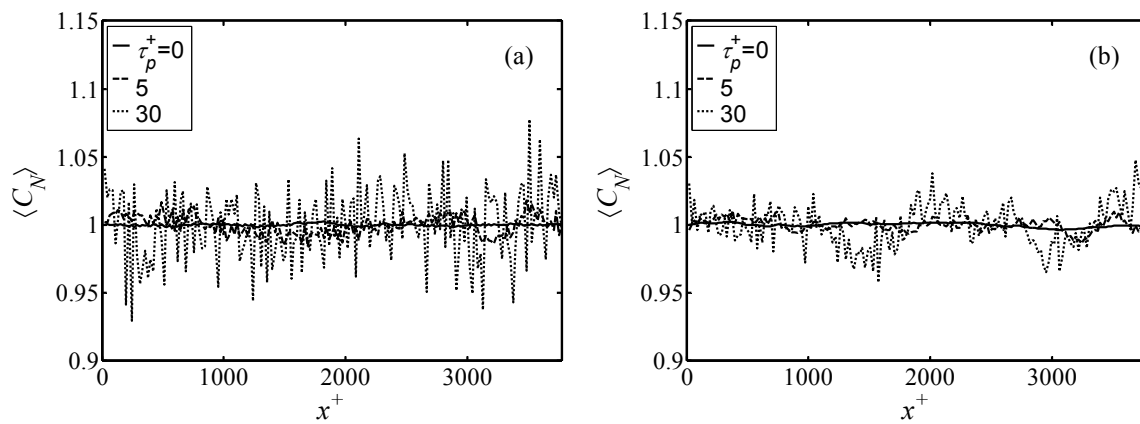


Figure 4.28. Normalized time-averaged particle number concentration along the streamwise direction for different inertia values in (a) Case III and (b) Case IV.

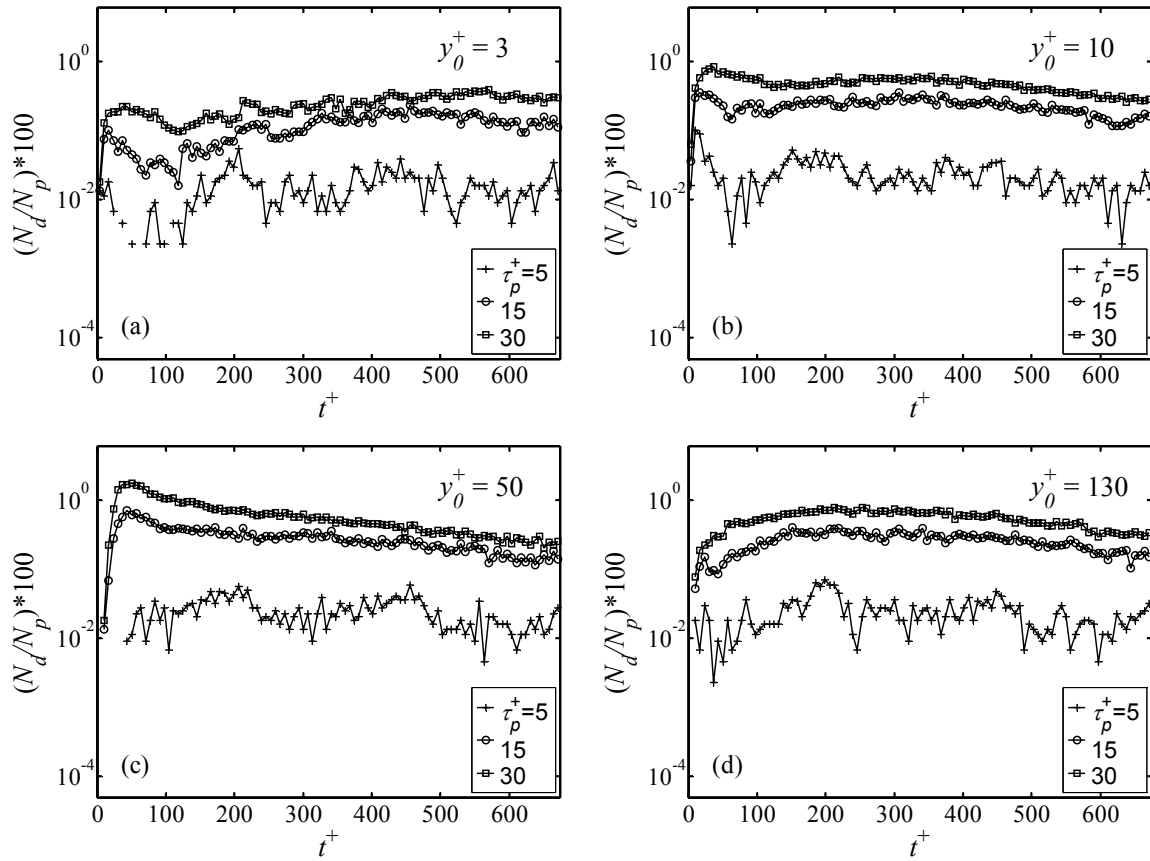


Figure 4.29. Deposition rate from four different initial release heights in Case IV. Deposition rate is normalized by the number of particles in the domain at  $t^+ = 0$ .

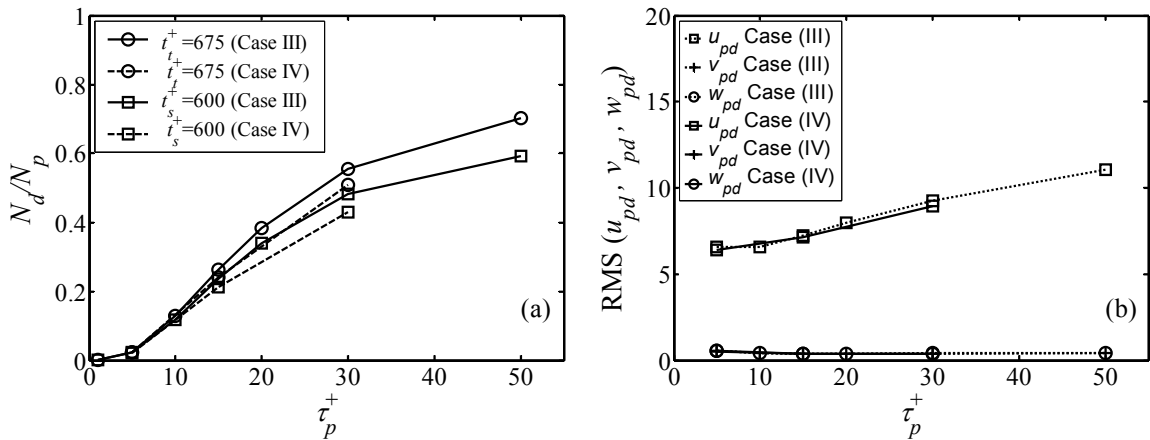


Figure 4.30. (a) Fraction of particles deposited in Case III and Case IV as a function of particle response time. (b) Wall-impact velocities from Case III and Case IV simulations as a function of particle response time.



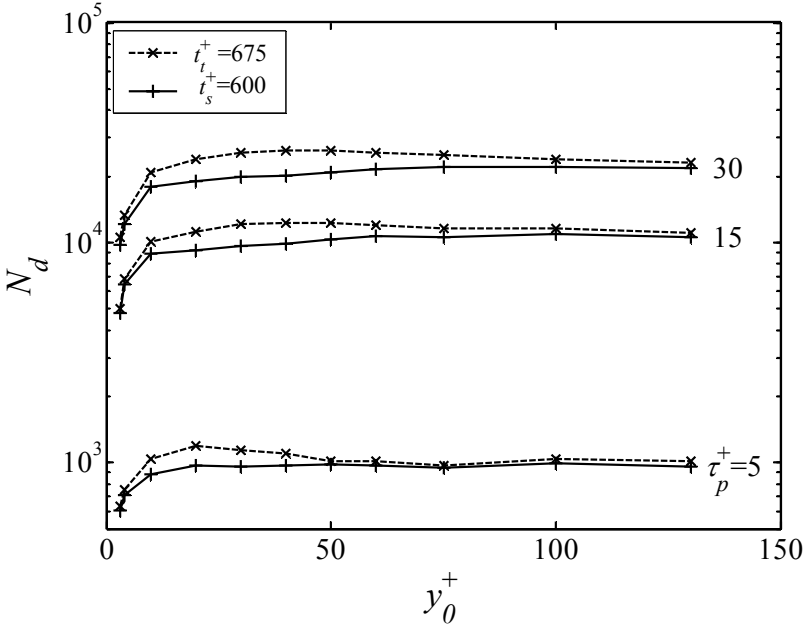


Figure 4.31 Number of particles deposited between the total time of simulation,  $0 \leq t_t^+ \leq 675$  and time of statistics,  $75 < t_s^+ \leq 675$ , as a function of the initial release height.

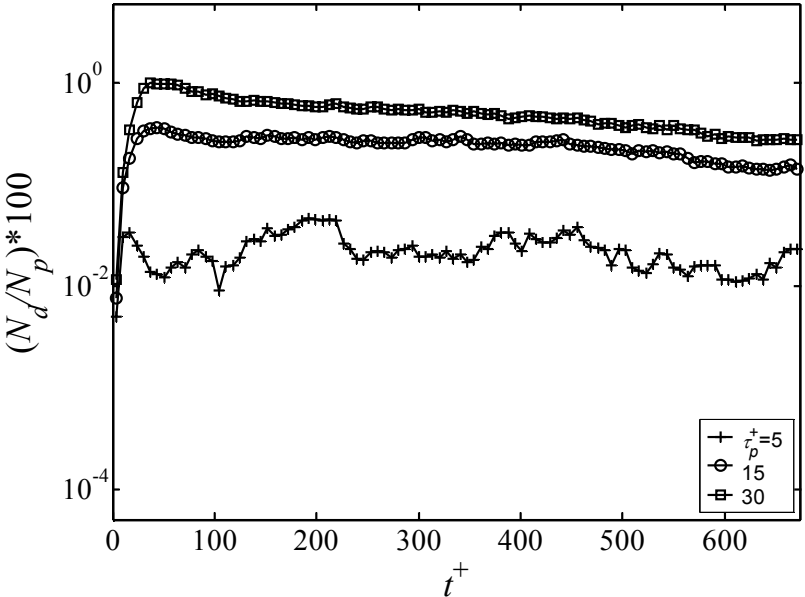


Figure 4.32. Averaged deposition rate from eleven different initial release heights, when normalized by the number of particles at  $t^+ = 0$ .

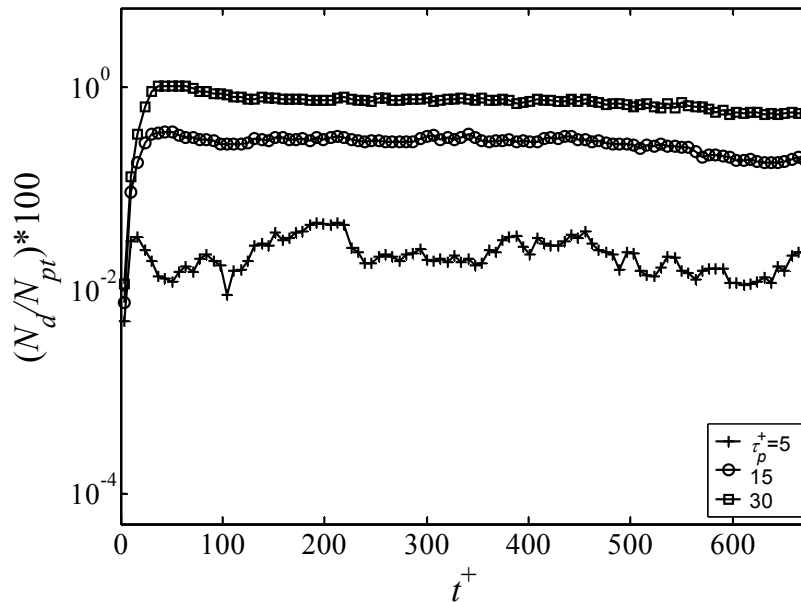


Figure 4.33. Averaged deposition rate from eleven different initial release heights, when normalized by the time varying number of particles in individual time bins.

Normalized and time-averaged concentration profiles in the homogeneous streamwise direction from Case III and Case IV are shown in figure 4.28 for three different particle response times. The fluctuations in the normalized concentration along the streamwise direction are very small. For both cases, the normalized streamwise concentration of passive tracers is observed to be much more uniform and close to unity implying good mixing of passive tracers.

### 4.3.3 Deposition rate

The deposition rate is shown in figures 4.29(a-d) for four different initial release heights. A higher deposition during the initial transient period ( $t^+ < 75$ ) occurs for initial release heights in the buffer region. The net contribution to deposition from the initial transient period can be seen clearly in figure 4.30(a), which shows the normalized net deposition over two different times of deposition for both Case III and Case IV. Figure 4.30(b) shows the RMS wall-impact velocities for the particles deposited during the last 600 time wall units of simulation in both Case III and Case IV. The wall-impact

velocities are very small and appear almost equal in wall-normal ( $y$ ) and spanwise ( $z$ ) directions. However, the streamwise component of the wall-impact velocity increases almost linearly with increasing particle response time, which demonstrates the effect of increasing particle inertia. Wall-impact velocities are important in the studies of particle-induced corrosion at the walls in particle-laden flows. Figure 4.31 shows the net deposition as a function of eleven initial release heights and for two different times of deposition. Figure 4.31 also demonstrates that the deposition during the first 75 time wall units of simulation is highest in case of initial release heights falling in the buffer region of turbulent boundary layer than those in the viscous sublayer or outer region.

The averaged deposition rate from the Case IV simulations is shown in figure 4.32 and 4.33. As in Case III (figure 4.22), after an initial transient period the particle deposition rate becomes nearly constant, when normalized with the number of particles remaining in suspension. Furthermore, this constant deposition rate is largely insensitive to the initial release height. This is not an unexpected result, since, for monodisperse particles, the rate of particle deposition ( $dN_d/dt$ ) is proportional to the particle number concentration per unit volume ( $C_v$ ) and the area of deposition ( $A_d$ ). The deposition constant,  $k_d^+$  (sometimes also called deposition velocity), is one of the most widely reported quantities in particle deposition studies. The deposition constant is calculated from the particle deposition rate and the particle concentration,

$$k_d^+ = \frac{J_w}{C_v u_\tau^a}, \quad (4.6)$$

where  $J_w$  is the particle mass flux to the wall per unit time and per unit area of deposition,  $C_v$  is the mean particle concentration per unit volume, and  $u_\tau^a$  is the mean friction velocity. For monodisperse particles in the present straight square duct, the deposition constant can be written as

$$k_d^+ = \frac{N_d}{4tdN_p u_\tau^a}. \quad (4.7)$$

The computation of deposition rate should be made over a period (i.e. time of deposition,  $t_d^+$ ) during which the concentration remains nearly constant. We have chosen the time of statistics as  $t_s^+ = 600$  which is 600 times the particle relaxation time for the lowest (finite-) inertia particles and 12 times for the highest inertia particles considered here. A gradual decrease in concentration occurs while observing deposition numerically over a reasonable length of time. One way to counter this would be to artificially introduce a particle in the domain for every particle deposited (as in van Haarlem, Boersma & Nieuwstadt 1998; Narayanan *et al.* 2003). While this would keep the concentration constant, the effect of particle initial conditions would remain large. Therefore, in the present computation, we first compute  $[k_d^+]$  i.e. the values of  $k_d^+$  determined from 100 individual time bins of width 6.75 time wall units using the time-local concentration in those bins. In each of these individual time bins, the particle number concentration does not drop appreciably. The time variation of computed deposition constants,  $[k_d^+]$ , from Case III and Case IV are shown in figure 4.34 and figure 4.35 respectively. On a linear-log plot,  $[k_d^+]$  appear nearly constant with time, after an initial transient period. The estimates of  $[k_d^+]$  from the last 89 time bins (i.e.  $t_s^+ \sim 600$ ) are averaged here to get the ensemble-averaged deposition constant,  $\langle k_d^+ \rangle$ . We have therefore computed ensemble-averaged deposition constants in individual time bins during which deposition remains nearly constant, even though over  $t_s^+ = 600$  it drops appreciably for longer particles response times.

---

$\tau_p^+$	1	5	10	15	20	30	50
$\langle k_d^+ \rangle$ : Case III	1.958e-5	2.780e-3	1.575e-2	3.454e-2	5.487e-2	9.165e-2	1.358e-1
$\langle k_d^+ \rangle$ : Case IV	-	2.609e-3	-	3.068e-2	-	7.818e-2	-

---

Table 4.5. Computed deposition constants from present DNS Case III and Case IV.

---

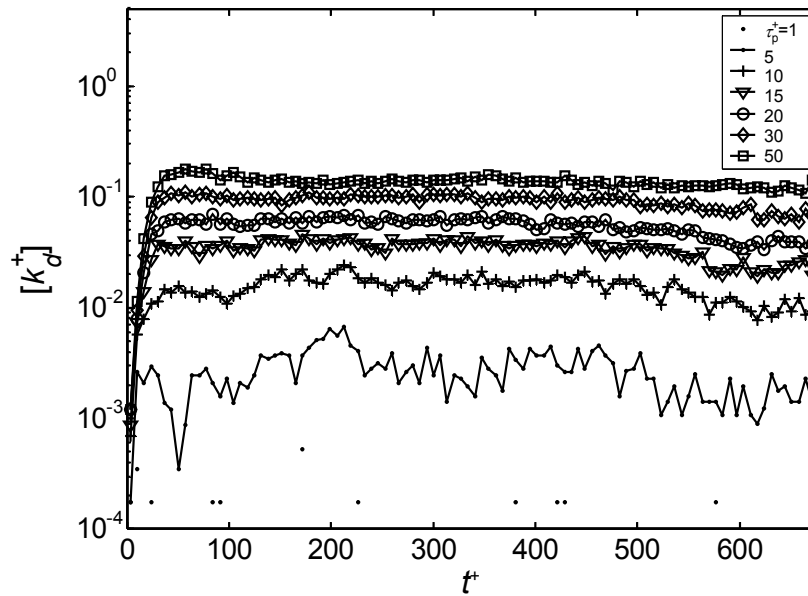


Figure 4.34. Time variation of the deposition constants computed in time bins in Case III.

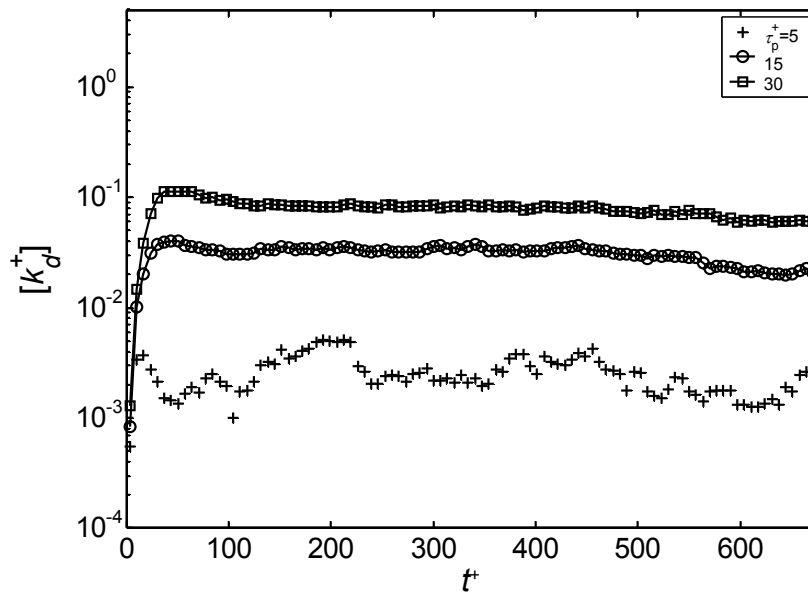


Figure 4.35. Time variation of the deposition constants computed in time bins in Case IV.

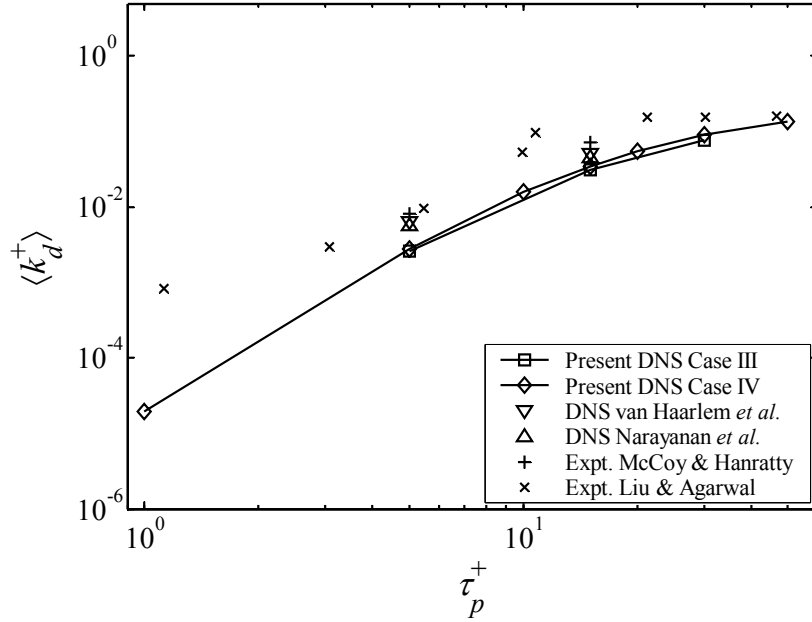


Figure 4.36. Ensemble-averaged deposition constants from Case III and Case IV, as a function of particle response time.

Figure 4.36 and table 4.5 show the numerically computed non-dimensional ensemble-averaged deposition constant  $\langle k_d^+ \rangle$ , as a function of non-dimensional particle response time,  $\tau_p^+$ . Also shown in figure 4.36 are the experimental and DNS data from other studies involving different flow geometries (circular pipe, straight channel) and somewhat different Reynolds numbers ( $\leq 10000$ ). Liu & Agarwal (1974) performed deposition experiments in a circular pipe using olive oil droplets in air and at a Reynolds number of 10000. Based on their measurements they suggested a correlation of the form  $k_d^+ = 6.00e-4(\tau_p^+)^2$  for particle response times in the range  $0 \leq \tau_p^+ \leq 10$ . McCoy & Hanratty (1977) suggested a correlation of the form  $k_d^+ = 3.24e-4(\tau_p^+)^2$ . As evident from figure 4.36, the estimates of  $\langle k_d^+ \rangle$  from the present DNS (Case III and Case IV) are in reasonably good agreement with previous DNS results for channel and pipe flows. We are not aware of any previous measurements of deposition in square ducts. In general, our computations yield smaller deposition constants than those from the DNS in a straight channel (with one free-slip surface) by van Haarlem *et al.* (1998), the DNS in an open

channel by Narayanan *et al.* (2003), as well as the experiments in a circular pipe by Liu & Agarwal (1974) and an annular flow by McCoy & Hanratty (1977). We note, however, that there is a notable difference between the  $k_d^+$  from the experiments of Liu & Agarwal (1974) and that from McCoy & Hanratty (1977) as well. The small difference between  $\langle k_d^+ \rangle$  from the present DNS and from other published DNS may most likely be attributed to the difference in flow geometries.

We have discussed in this section the computation of Lagrangian particle transport statistics in a low Reynolds number turbulent straight square duct. Particle transport statistics for all the parameters listed in tables 4.1-4.4 were not presented in this thesis. An interested reader may obtain them from the author.

## 5. CONCLUSIONS

Particle-laden turbulent flow through a straight square duct at  $Re_\tau = 300$  was studied using direct numerical simulation and Lagrangian particle tracking. A particle tracking direct numerical simulation code was developed by the author to carry out the large-scale turbulent flow and particle transport computations on serial and parallel computers. The DNS code was validated after demonstrating good agreement with the published DNS results for the same flow and Reynolds number. A number of important turbulent transport parameters were computed for particles with varying degrees of inertia. These include diffusivity, inter-particle separation, penetration, and deposition rate. In some cases, particle dispersion was found to behave similarly to what is predicted for isotropic turbulence, including a  $t^2$  and subsequent  $t^3$  dependence of the square of inter-particle separation. In addition, we have observed an intermediate-time power law regime that appears to be sensitive to particle inertia and initial separation. We have observed evidence of a transition from a *diffusion-impaction* to an *inertia-moderated* regime within a specific range of particle response times. Deposition within the turbulent square duct exhibits qualitative similarities with previous deposition studies in other geometries, including plane channels and circular pipes. A deposition constant was calculated and was shown to increase monotonically with particle inertia over the range of particle response times considered here. Passive tracers do not deposit, but were observed to accumulate inside structures within the turbulent boundary layer.

The present computations did not take into account the effect of additional forces other than the dominant Stokes drag force. It will be interesting to see the effect of additional forces, like the Saffman lift force, on the deposition of low response time particles. This force can notably influence the near-wall behavior of low particle-fluid density ratio and low inertia particles and therefore can enhance their particle deposition rate. It is expected that for the low inertia particles the deposition should somewhat increase with the inclusion of this force. It would be interesting to perform particle transport experiments in the square duct and see how they agree or disagree with the



present simulations. We would also recommend performing a direct numerical simulation and Lagrangian particle tracking at higher Reynolds number with a wider range of particle response times than considered in the present simulation. It would also be interesting to see the effect of dispersed particles on turbulence i.e. a simulation where two way fluid-particle coupling is considered for this flow.

We have generated useful new data on Lagrangian particle transport in a straight square duct using large-scale time-accurate numerical simulations. The results reported in this thesis are valuable new information on particle transport characteristics of a low Reynolds number turbulent straight square duct. To the best of our knowledge, these results are the first that use direct numerical simulation coupled with Lagrangian particle tracking for this flow.

## REFERENCES

- BABIANO, A., BASDEVANT, C., LE ROY, P. & SADOURNY, R. 1990 Relative dispersion in two-dimensional turbulence. *J. Fluid Mech.* **214**, 535-557.
- BAGCHI, P. & BALACHANDAR, S. 2003 Effect of turbulence on the drag and lift of a particle. *Phys. Fluids* **15**, 3496-3513.
- BATCHELOR, G. K. 1950 The application of the similarity theory of turbulence to atmospheric diffusion. *Q. J. R. Meteorol. Soc.* **76**, 133-146.
- BATCHELOR, G. K. 1952 Diffusion in a field of homogenous turbulence. II. The relative motion of particles. *Proc. Camb. Phil. Soc.* **48**, 345-361.
- BROOKE, J. W., HANRATTY, T. J. & MCLAUGHLIN, J. B. 1994 Free-flight mixing and deposition of aerosols. *Phys. Fluids* **6**, 3404-3415.
- DESHPANDE, M. D. 1993 Flow regimes in a three-dimensional driven cavity. *National Aerospace Laboratories, Project Document PD CF 9305*.
- DESHPANDE, M. D. & MILTON, S. G. 1998 Kolmogorov scales in a driven cavity flow. *Fluid Dyn. Res.* **22**, 359-381.
- DESHPANDE, M. D. & SHARMA, G. 1999 Flow intensification in the solution of 3-dimensional Euler equations. *National Aerospace Laboratories, Project Document PD CF 9912*.
- ELGHOBASHI, S. & TRUESDELL, G. C. 1992 Direct simulation of particle dispersion in a decaying isotropic turbulence. *J. Fluid Mech.* **242**, 655-700.
- GAVRILAKIS, S. 1992 Numerical simulation of low-Reynolds-number turbulent flow through a straight square duct. *J. Fluid Mech.* **244**, 101-129.
- VAN HAARLEM, B., BOERSMA, B. J. & NIEUWSTADT, F. T. M. 1998 Direct numerical simulation of particle deposition onto a free-slip and no-slip surface. *Phys. Fluids* **10**, 2608-2620.
- HARLOW, F. H. & WELCH, J. E. 1965 Numerical calculation of time-dependent viscous incompressible flow of fluid with free surface. *Phys. Fluids A* **8**, 2182-2189.

- HUSER, A. & BIRINGEN, S. 1993 Direct numerical simulation of turbulent flow in a square duct. *J. Fluid Mech.* **257**, 65-96.
- JULLIEN, M.-C., PARET, J. & TABELING, P. 1999 Richardson pair dispersion in two-dimensional turbulence. *Phys. Rev. Lett.* **82**, 2872-2875.
- KAWAMURA, T., TAKAMI, H. & KUWAHARA, K. 1986 Computation of high Reynolds number flow around a circular cylinder with surface roughness. *Fluid Dyn. Res.* **1**, 145-162.
- KOLMOGOROV, A. N. 1941 The local structure of isotropic turbulence in an incompressible viscous fluid. *Dokl. Akad. Nauk. SSSR* **30**, 301-305.
- LA PORTA, A., VOTH, G. A., CRAWFORD, A. M., ALEXANDAR, J. & BODENSCHATZ, E. 2001 Fluid particle accelerations in fully developed turbulence. *Nature* **409**, 1017-1019.
- LIU, B. Y. H. & AGARWAL, J. K. 1974 Experimental observation of aerosol deposition in turbulent flow. *J. Aerosol Sci.* **5**, 145-155.
- MACINNES, J. M. & BRACCO, F. V. 1992 Stochastic particle dispersion modeling and the tracer-particle limit. *Phys. Fluids A* **4**, 2809-2824.
- MADABHUSHI, R. K. & VANKA, S. P. 1991 Large eddy simulation of turbulence-driven secondary flow in a square duct. *Phys. Fluids A* **3**, 2734-2745.
- MAXEY, M. R. 1987 The motion of small spherical particles in a cellular flow field. *Phys. Fluids* **30**, 1915-1928.
- MCCOY, D. D. & HANRATTY, T. J. 1977 Rate of deposition of droplets in annular two-phase flow. *Int. J. Multiphase Flow* **3**, 319-331.
- MCLAUGHLIN, J. B. 1989 Aerosol particle deposition in numerically simulated channel flow. *Phys. Fluids A* **1**, 1211-1224.
- MOIN, P. & MAHESH, K. 1998 Direct numerical simulation: A tool in turbulent research. *Annu. Rev. Fluid Mech.* **30**, 539-578.
- MONIN, A. S. & YAGLOM, A. M. 1971 *Statistical Fluid Mechanics: Mechanics of Turbulence*, Vol 1. MIT Press.

- NARAYANAN, C., LAKEHAL, D., BOTTO, L. & SOLDATI, A. 2003 Mechanisms of particle deposition in a fully developed turbulent open channel flow. *Phys. Fluids* **15**, 763-775.
- OBUKHOV, A. M. 1941 On the distribution of energy in the spectrum of turbulent flow. *Izv. Akad. Nauk. SSSR Ser. Geogr. Geofiz.* **5**, 453-466.
- OTT, S. & MANN, J. 2000 An experimental investigation of the relative diffusion of particle pairs in three-dimensional turbulent flow. *J. Fluid Mech.* **422**, 207-223.
- OTTINO, J. M. 1990 Mixing, chaotic advection, and turbulence. *Annu. Rev. Fluid Mech.* **22**, 207-254.
- PEYRET, R. 2002 *Spectral Methods for Incompressible Viscous Flow*. Springer Verlag.
- POZRIKIDIS, C. 2001 *Fluid Dynamics: Theory, Computation, and Numerical Simulation*. Kluwer Academic Publishers.
- PRESS, W. H., TEUKOLSKY, S. A., VETTERLING, W. T. & FLANNERY, B. P. 1992 *Numerical Recipes in FORTRAN 77: The Art of Scientific Computing*. Cambridge University Press.
- PROVENZALE, A. 1999 Transport by coherent barotropic vortices. *Annu. Rev. Fluid Mech.* **31**, 55-93.
- QUADRIO, M. & LUCHINI, P. 2003 Integral space-time scales in turbulent wall flows. *Phys. Fluids* **15**, 2219-2227.
- RAI, M. M. & MOIN, P. 1991 Direct simulations of turbulent-flow using finite-difference schemes. *J. Comput. Phys.* **96**, 15-53.
- RICHARDSON, L. F. 1926 Atmospheric diffusion shown on a distance-neighbor graph. *Proc. Roy. Soc. Lond. Ser. A* **110**, 709-737.
- ROBINSON, S. K. 1991 Coherent motions in the turbulent boundary layer. *Annu. Rev. Fluid Mech.* **23**, 601-639.
- ROVELSTAD, A. L., HANDLER, R. A. & BERNARD, P. S. 1994 The effect of interpolation errors on the Lagrangian analysis of simulated turbulent channel flow. *J. Comput. Phys.* **110**, 190-195.

- SAFFMAN, P. G. 1965 The lift on a small sphere in a slow shear flow. *J. Fluid Mech.* **22**, 385-400.
- SAWFORD, B. 2001 Turbulent relative dispersion. *Annu. Rev. Fluid Mech.* **33**, 289-317.
- SQUIRES, K. D. & EATON, J. K. 1991 Measurements of particle dispersion obtained from direct numerical simulations of isotropic turbulence. *J. Fluid Mech.* **226**, 1-35.
- SWARZTRAUBER, P. N. 1984 Fast Poisson solvers. *Studies in Numerical Analysis* (ed. G. H. Golub), Vol. 24, pp 319-370 Mathematical Association of America.
- SWARZTRAUBER, P. N. & SWEET, R. A. 1979 Efficient Fortran subprograms for the solution of separable elliptic partial differential equations. *ACM Trans. Math. Software* **5**, 352-364.
- TAYLOR, G. I. 1921 Diffusion by continuous movements. *Proc. Lond. Math. Soc. Ser. 2*, **20**, 196-211.
- UIJTTEWAAL, W. S. J. & OLIEMANS, R. V. A. 1996 Particle dispersion and deposition in direct numerical and large eddy simulations of vertical pipe flows. *Phys. Fluids* **8**, 2590-2604.
- VAZQUEZ, M. S. & METAIS, O. 2002 Large-eddy simulation of the turbulent flow through a heated square duct. *J. Fluid Mech.* **453**, 201-238.
- VIRANT, M. & DRACOS, T. 1997 3D PTV and its application on Lagrangian motion. *Meas. Sci. Technol.* **8**, 1539-1552.
- WANG, L. P., MAXEY, M. R., BURTON, T. D. & STOCK, D. E. 1992 Chaotic dynamics of particle dispersion in fluids. *Phys. Fluids A* **4**, 1789-1804.
- WILLIAMSON, J. H. 1980 Low-storage Runge-Kutta schemes. *J. Comput. Phys.* **35**, 48-56.
- YEUNG, P. K. 1994 Direct numerical simulation of two-particle relative diffusion in isotropic turbulence. *Phys. Fluids* **6**, 3416-3428
- YEUNG, P. K. 2002 Lagrangian investigations of turbulence. *Annu. Rev. Fluid Mech.* **34**, 115-142.
- YEUNG, P. K. & POPE, S. B. 1989 Lagrangian statistics from direct numerical simulations of isotropic turbulence. *J. Fluid Mech.* **207**, 531-586.

YOUNG, J. & LEEING, A. 1997 A theory of particle deposition in turbulent pipe flow. *J. Fluid Mech.* **340**, 129-159.

## VITA

Gaurav Sharma was born in Mandi, Himachal Pradesh, India. He obtained a Bachelor of Technology (B.Tech.) degree in mechanical engineering from Regional Engineering College (REC) Hamirpur, India (now a National Institute of Technology) in 1998. For a one-year period (1998-1999) following his undergraduate studies, he joined the National Aerospace Laboratories (N.A.L.), Bangalore as a graduate trainee in its Computational and Theoretical Fluid Dynamics (CTFD) Division working under the supervision of Dr. M. D. Deshpande. He attended the University of Houston between fall'00 and summer'01 and worked as a research assistant in its Institute of Fluid Dynamics and Turbulence (IFDT). He transferred to the Texas A&M University in fall '01 and joined the research group of Dr. Denis Phares in spring'02. His research interests are in fluid dynamics, turbulence, Lagrangian particle transport, and scientific computing.

Gaurav Sharma can be reached at [gsharma@indiatimes.com](mailto:gsharma@indiatimes.com). His permanent home address is: House No. 127/2, Purani Mandi, Mandi – 175 001, Himachal Pradesh, India.